PHOTODISSOCIATION STUDIES

USING A XENON EXCIMER LASER

by

EVANGELOS THEOCHAROUS B.Sc. A.R.C.S.

A thesis submitted in partial fulfilment of the requirements for the degree of Doctor of Philosophy of the University of London and the Diploma of Imperial College

January 1981

Blackett Laboratory
Imperial College
London, England

To my parents

ABSTRACT

The photoionization cross section of excited state selenium, $Se(^1S)$, obtained by the photodissociation of OCSe, was measured in the wavelength region 170 to 175 nm using a tuned xenon excimer laser. A minimum value, at 172 nm was found to be 1.2×10^{-20} cm^2. The photodissociation cross section for OCSe, at the same wavelength, was measured to be 0.8×10^{-16} cm^2.

The work required the developement of a reliably tunable xenon excimer laser. The operation of the laser was investigated under different pumping power densities. Parameters affecting the tunability of the laser were identified. Tuning of the laser was achieved using diffraction gratings and prisms as dispersive elements.

Using this laser, the absolute photoionization cross section of ground state caesium atoms was measured. A value of 0.9×10^{-19} cm^2 is reported at 172 nm, in agreement with recent theoretical calculations.

The laser was shown to be ideal for the dissociation studies of the mercuric halides, (HgX_2, X=I, Br, Cl). The dissociation products include the excited state radicals $HgX^*(B)$. The effects of the addition of argon on the spectral and temporal behaviour of $HgX(B \rightarrow X)$ fluorescence were investigated. Values for the collisional quenching rates of $HgX^*(B)$ by argon, for pressures up to one atmosphere are reported. The radiative lifetimes of the $HgX(B \rightarrow X)$ transitions were calculated.

Further applications of the xenon excimer laser in photodissociation spectroscopy are suggested and discussed.

CONTENTS

		Page
ABSTRACT		3
CHAPTER 1	INTRODUCTION TO MOLECULAR PHOTODISSOCIATION	7
CHAPTER 2	THE XENON LASER	
	2.1 Introduction	13
	2.2 The Spectroscopy of the Xenon Excimers	13
	2.3 The Kinetics of the Xenon Excimers	14
	2.4 The High Voltage Generator	22
	2.5 The Coaxial Diode	24
	2.6 Fluorescence Studies of the Xenon Excimers	26
	2.7 The Untuned Xenon Laser	28
	2.7.1 Pressure Optimization of the Laser Output	30
	2.7.2 The Red Shift	32
	2.7.3 Mirror Optimization of the Laser Output	32
	2.7.4 Damage to Optical Components	35
	2.8 The Identification of the Impurities	39
	2.8.1 The Origins of the Visible Bands	42
	2.8.2 Gas Handling and Gas Purification	46
	2.9 The Tuning of the Xenon Excimer Laser	47
	2.9.1 Tuning Using a 1200 lines mm^{-1} Grating	48
	2.9.2 Tuning Using a 3600 lines mm^{-1} Grating	51
	2.9.3 Tuning Using a Spectrasil Prism	54
	2.9.4 The Introduction of an Aperture in the Cavity	62
	2.9.5 Tuning Using a BaF_2 Prism	62
	2.9.6 Tuning Using a Two-Prism Tuning Element	64
	2.9.7 Pressure Tuning	67
	2.9.8 Comparison of the Performance of Different Tuning Elements	68

		Page
CHAPTER 3	MEASUREMENT OF THE PHOTOIONIZATION CROSS SECTION OF Se(^{1}S) IN THE RANGE 170-175 nm	
	3.1 Introduction to Group VIA Lasers	70
	3.2 The Production of Se(^{1}S) by Photodissociation	73
	3.3 The Se(^{1}S) Loss Mechanisms	77
	3.4 Theoretical Background	78
	3.5 The Experimental Apparatus	81
	3.6 Experimental Results	86
	3.7 Discussion	96
CHAPTER 4	ABSOLUTE DETERMINATION OF THE PHOTOIONIZATION CROSS SECTION OF GROUND STATE CAESIUM AT 172 nm	
	4.1 Introduction	99
	4.2 Summary of Previous Work	99
	4.3 Theoretical Background	101
	4.4 The Experimental Apparatus	102
	4.5 Experimental Results	104
	4.6 Discussion	106
CHAPTER 5	PHOTODISSOCIATION STUDIES IN THE MERCURIC HALIDES	
	5.1 Introduction	113
	5.2 Historical Background	114
	5.3 The Spectroscopy of the Mercuric Halides	115
	5.4 Theoretical Background	118
	5.5 The Experimental Apparatus	119
	5.6 Experimental Results	120
	5.6.1 Studies in HgI_2	124
	5.6.2 Studies in $HgBr_2$	132
	5.6.3 Studies in $HgCl_2$	135
	5.6.4 Photodissociation Studies in HgX_2 Solution	

Page

5.7 Discussion 140

CHAPTER 6 CONCLUSIONS - SUGGESTIONS FOR FURTHER WORK 145

APPENDIX A 151

REFERENCES 154

ACKNOWLEDGEMENTS 165

PUBLICATIONS 166

CHAPTER 1

INTRODUCTION TO MOLECULAR PHOTODISSOCIATION

A molecule is a collection of atoms that possesses distinctive and distinguishing properties. A molecule is said to be stable if the molecular group of atoms does not spontaneously rearrange or disintegrate. For a stable diatomic molecule, its potential energy curve possesses a minimum when the separation between the two atomic nuclei has its equilibrium value. At this separation, the attractive force due to the electronic binding is equal to the repulsive force due to the positively charged nuclei. For smaller interatomic distances the coulombic force dominates and the potential energy of the system rises sharply due to the work needed to overcome the repulsive force. As the separation between the atoms increases, the electronic binding force becomes superior so the potential energy rises again.

A diatomic molecule is expected to have a large number of electronic states, each identified with its own potential energy curve. Some of these curves have potential minima and represent stable states. Others do not possess a minimum and correspond to unstable states. The atoms of a diatomic molecule populating an unstable state will exert a repulsive force on each other for all interatomic distances. With increasing internuclear separation both stable and unstable energy curves will approach asymptotically to a series of dissociation limits, each corresponding to an excitation state of the constituent atoms.

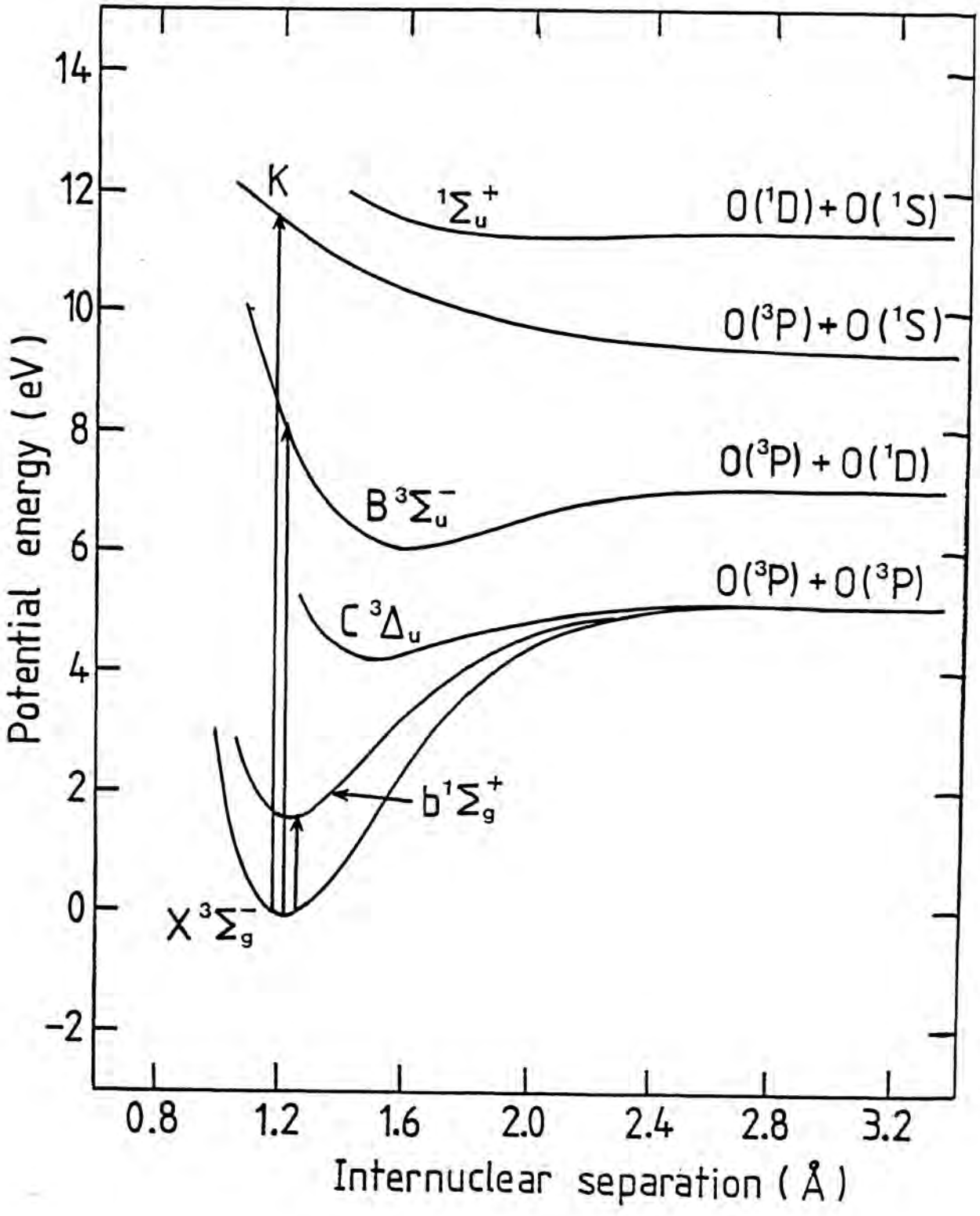
The absorption and emission spectra of diatomic molecules

are much more compex than atomic spectra. The concept of potential energy curves has been invaluable in the understanding of molecular spectra. According to classical theory, a stable molecule is vibrating about the potential minimum so that the internuclear separation varies between two extreme values. The molecule will thus spend a lot of time at the two limits of vibration where its kinetic energy is zero. These are also the points from which the molecule is most likely to undergo an electronic transition.

The time taken for a molecule to undergo a transition is estimated[1] to be less than 10^{-15} seconds. This is considerably shorter than the period of one vibrational oscillation (10^{-13} seconds). Therefore the velocities and separation of the two nuclei are expected to remain unaltered during an electronic transition. This is known as the Frank- Condon principle[2] and can be used to interpret the observed intensity distribution of a molecular spectrum.

Schrodinger's wave equation states that the vibrational energy of a molecule is quantized. Electronic transitions between two bound states will therefore show band structure. In the case of absorption or emission of a continuous spectrum however, at least one of the energy states between which the transition is taking place must be unquantized. Only kinetic energy can account for the continuous nature of an energy state. Absorption of a continuous spectrum will therefore indicate the dissociation of the molecule.

Figure 1 shows the electronic states of the oxygen molecule. The figure illustrates the three main types of molecular electronic transitions. At room temperature absorption will take place mainly from the lowest vibrational



Energy levels of the oxygen molecule

FIGURE 1

level of the ground state. The Frank-Condon principle determines that the strongest absorption will occur to regions of higher electronic states that lie vertically above the ground state minimum. The transition:

$$O_2(X^3\Sigma_g^-) + h\nu(700\ nm) \longrightarrow O_2(b^1\Sigma_g^+) \qquad (1\text{-}1)$$

takes place between two bound states and gives rise to an absorption spectrum with band structure[3]. The transition:

$$O_2(X^3\Sigma_g^-) + h\nu(\lambda<133\ nm) \longrightarrow O_2(K) \qquad (1\text{-}2)$$

terminates to an unbound state which dissociates within a period of oscillation to $O(^1S_0)$ and $O(^3P)$ [4]. The absorption is continuous and any excess photon energy appears as kinetic energy of the dissociation fragments. The transition:

$$O_2(X^3\Sigma_g^-) + h\nu(\ =170nm) \longrightarrow O_2(B^3\Sigma_u^-) \qquad (1\text{-}3)$$

is between two bound states (see fig. 1). However, maximum absorption terminates at a point on the $O_2(B^3\Sigma_u^-)$ potential curve which is higher than the dissociation limit. This absorption gives rise to the Schumann-Runge continuum[2] which sets a lower wavelength limit to spectroscopic work in air. The dissociation products are $O(^1D)$ and $O(^3P)$.

The lowest dissociation energy of the oxygen molecule is[5] E_b=5.1eV, the binding energy of the molecular ground state. Further dissociation limits occur for energies $E=E_b + E_a$ where E_a corresponds to the energy of different atomic states of oxygen. Photodissociation can therefore be used to populate an atomic state of oxygen of energy E_i provided photolysis radiation of photon energy $E_p = E_b + E_i$ is utilised. If the photon energy can be varied in the range E_1 to E_2 then atomic oxygen states lying in the region

$E_2 - E_b$ and $E_1 - E_b$ can be populated. It is therefore important for the photodissociation source to possess as wide a tuning range as possible. It is also important to use a photolysis source operating in the far UV or VUV part of the spectrum since most stable molecules possess dissociation energies in 4 to 7 eV range[5].

The spectral width of dissociative continua corresponding to specific dissociation channels can be very wide ($>10^3$ cm^{-1}). However, overlap of different absorption continua necessitates the use of a pump source of sufficiently narrow spectral output so that only one type of dissociation products is produced with a significant quantum yield. This condition is particularly important when photodissociation is used to populate the upper state of a lasing transition. The pump source must have a narrow enough spectral output so that the photodissociative production of the lower laser state is insignificant.

Photodissociation can be used to generate atoms or molecules in an excited state in order to study their radiative lifetimes and different quenching reactions (see chapter 5 for references). However the theory of these processes can be substantially simplified provided the population of the upper state occurs in a time which is short compared with the radiative lifetime of the excited state. It is highly desirable therefore, to use short pulse excitation for photodissociation studies.

In any experiment, a high value of signal to noise ratio is desirable. A large signal can be achieved using a high power excitation pulse.

In the next chapter the characteristics of a Xenon

excimer laser are described. This laser was shown to be capable of producing output pulse energies in excess of 30 mJ, with a pulse duration of 10 ns. The laser could be tuned from 169 to 175 nm. The output photon energy of 7.2 eV is higher than the binding energies of most stable molecules[5]. Chapters 3, 4 and 5 describe the use of this laser in the photodissociation studies of some simple molecules.

CHAPTER 2

THE XENON LASER

2.1 Introduction

The emission of the rare gas VUV continua, together with the hydrogen continuum have been used as standard VUV light sources for many years[6]. Their origin was studied extensively[7,8,9] and the repulsive nature of the ground state was well understood when Houtermans[10] proposed that bound-free transitions could be used to obtain laser action. These transitions terminate on a highly repulsive ground state which dissociates within a period of a molecular vibration ($\sim 10^{-13}$s). The lower laser level will therefore be emptied very rapidly and bottlenecking of the lower state should not occur.

The emission bandwidth of these continua is very broad (>10 nm). Since the gain coefficient is inversely proportional to the bandwidth, a large population inversion and thus high pumping power densities are required to achieve lasing threshold. Basov[11] used an electron beam to excite liquid xenon and observed laser action at 176 nm. Soon afterwards lasing was obtained in high pressure xenon gas at 172 nm[12], krypton at 146 nm[13] and argon at 126nm[14].

2.2 The spectroscopy of the xenon excimers

The resistance of ground state xenon atoms to forming compounds is explained by a full outermost shell which has a configuration ...$5s^2 5p^6 (^1S_0)$. However, the first excited

state of xenon, $...5s^2 5p^5 6s^1 ({}^3P_{1,2,3}, {}^1P_1)$ resembles a caesium atom and is expected to enter into molecular bonds very readily. It is able to combine with a ground state xenon atom to form an excited dimer, known as excimer. The bond consists of a molecular ion core, Xe_2^+, with the valence electron orbiting around this core. Rydberg states can therefore be used to understand the spectroscopy of xenon excimers[15].

Figure 2 shows the most important energy levels of the xenon system, based on the estimates of Mullikan[16]. Time resolved absorption studies in high pressure xenon confirm the shape of the lower excimer levels[17]. Apart from the highly repulsive ground state the most important features are the two lower excimer states ${}^3\Sigma_u^+$ and ${}^1\Sigma_u^+$ which have binding energies of ~0.5 eV. Emission from these states, which correlate to atomic states ${}^3P_2$ and ${}^3P_1$ respectively, give rise to the 172 nm xenon continuum.

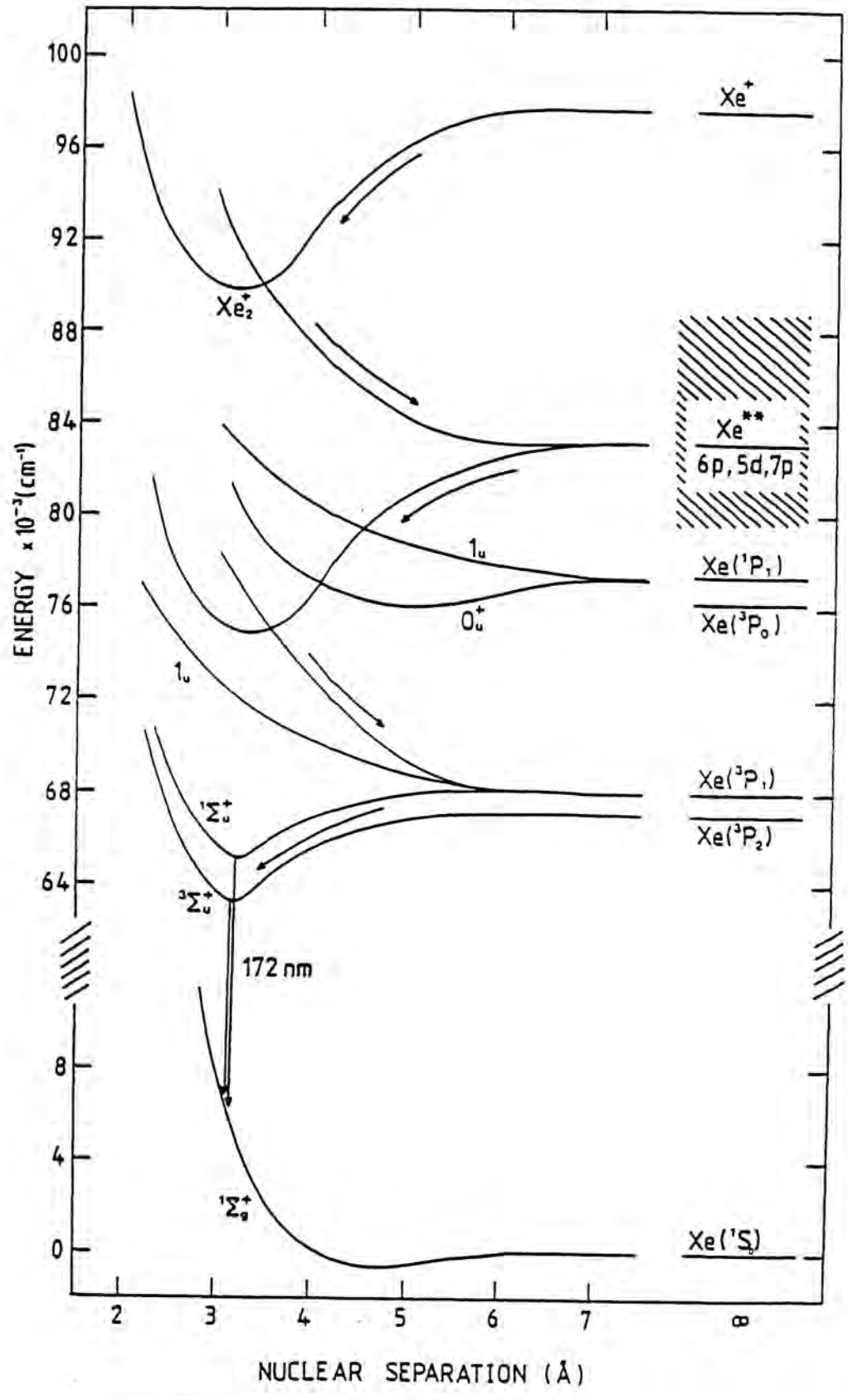
2.3 The kinetics of the xenon excimers

When a beam of high energy electrons ($\gtrsim$0.5 MeV) enters a cell containing high pressure xenon gas the main energy loss mechanism will be the ionization process:

$$e_p^- + Xe \longrightarrow Xe^+ + e_p^- + e_s^- \qquad (2.1)$$

Although large electron densities are generated by this process, most of the excitation is done by primary electrons. The temperature of the secondary electrons will decrease rapidly due to inelastic collitions in the generated plasma. These low energy electrons ($kT_e \approx 2$ eV) play an important role in mixing the populations of states lying kT_e apart.

Due to the surrounding high pressure gas, xenon ions



Energy levels of the Xenon molecule

FIGURE 2

will be rapidly converted to molecular ions via the three body process:

$$Xe^+ + Xe + Xe \longrightarrow Xe_2^+ + Xe \qquad (2.2)$$

Table 2.1 summarizes the relevant reactions for the formation of the upper laser states and gives the corresponding rate constants and source of reference.

In figure 2 an unbound state was drawn crossing the molecular ion potential minimum and dissociating to a highly excited atomic state. In practice there will be a large number of such states, dissociating in the shaded region[16]. Each can provide a pathway for predissociation with the aid of a slow electron:

$$Xe_2^+ + e \longrightarrow Xe^{**} + Xe \qquad (2.3)$$

This process is known as dissociative recombination and can be very fast (< 1 nm) in the presence of a large density of thermalised electrons.

Werner et al[18] postulated the existence of a molecular ionic trimer, Xe_3^+ . This can increase the rate of conversion of atomic ions Xe^+ to highly excited xenon atoms (see eq. 2.4 and eq. 2.5 in table 2.1) so a lower elecrton density is predicted at higher pressures.

The highly excited xenon atoms are unlikely to have time to decay radiatively. Radiation trapping in the plasma will reduce the effects of such a process even further. In the high pressure gas, fast recombination (eq. 2.6) followed by dissociation (eq. 2.7) will be a much faster process. Finally, fast recombination will populate the upper laser states (eq. 2.9 and 2.10).

The triplet state $^3\Sigma_u^+$ lies approximately 0.1 eV below

TABLE 2.1

Eq.	REACTION	RATE	Ref.
2.1	$Xe + e_p \longrightarrow Xe^+ + e_p + e_s$		
2.1(a)	$Xe + e_p \longrightarrow Xe^{**} + e_p$		
2.2	$Xe^+ + Xe + Xe \longrightarrow Xe_2^+ + Xe$	3.6×10^{-31} cm^6 sec^{-1}	29
2.3	$Xe_2^+ + e^- \longrightarrow Xe^{**} + Xe$	1.4×10^{-6} cm^3 sec^{-1} 3.0×10^{-7} cm^3 sec^{-1}	30 24
2.4	$Xe_2^+ + Xe + Xe \longrightarrow Xe_3^+ + Xe$	9.0×10^{-32} cm^6 sec^{-1}	18
2.5	$Xe_3^+ + e \longrightarrow Xe^{**} + Xe + Xe$	9.5×10^{-5} cm^3 sec^{-1} 3.0×10^{-6} cm^3 sec^{-1}	18 24
2.6	$Xe^{**} + Xe + Xe \longrightarrow Xe_2^{**} + Xe$	3.0×10^{-32} cm^6 sec^{-1}	18
2.7	$Xe_2^{**} \longrightarrow Xe^*(^3P_1, {}^3P_2) + Xe$		
2.o	$Xe^*(^3P_1) + e^- \rightleftharpoons Xe^*(^3P_2) + e^-$		
2.9	$Xe^*(^3P_1) + Xe + Xe \longrightarrow Xe_2^*(^1\Sigma_u^+) + Xe$	1.7×10^{-32} cm^6 sec^{-1}	31
2.10	$Xe^*(^3P_2) + Xe + Xe \longrightarrow Xe_2^*(^3\Sigma_u^+) + Xe$	7.0×10^{-32} cm^6 sec^{-1}	32
2.11	$Xe_2^*(^1\Sigma_u^+) + Xe \longrightarrow Xe_2^*(^3\Sigma_u^+) + Xe$	1.2×10^{-13} cm^3 sec^{-1}	18

TABLE 2.1 (continued)

Eq.	REACTION	RATE	Ref.
2.12	$Xe_2^*(^1\Sigma_u^+) + e \rightleftharpoons Xe_2^*(^3\Sigma_u^+) + e$	2.3×10^{-7} cm^3 sec^{-1}	18
2.13	$Xe_2^*(^1\Sigma_u^+) \longrightarrow Xe_2(^1\Sigma_g^+) + h\nu(172\ nm)$	$t = 4.6 \times 10^{-9}$ sec $t = 6.9 \times 10^{-9}$ sec	17 33
2.14	$Xe_2^*(^3\Sigma_u^+) \longrightarrow Xe_2(^1\Sigma_g^+) + h\nu(172\ nm)$	$t = 99 \times 10^{-9}$ sec $t = 112 \times 10^{-9}$ sec	17 33
2.15	$Xe_2^*(^1\Sigma_u^+) + h\nu(172\ nm) \longrightarrow Xe_2(^1\Sigma_g^+) + h\nu + h\nu$	$\sigma = 1.5 \times 10^{-17}$ cm^2	18
2.16	$Xe_2^*(^3\Sigma_u^+) + h\nu(172\ nm) \longrightarrow Xe_2(^1\Sigma_g^+) + h\nu + h\nu$	$\sigma = 1.0 \times 10^{-18}$ cm^2	18
2.17	$Xe_2^*(^1\Sigma_u^+, {}^3\Sigma_u^+) + h\nu(172\ nm) \longrightarrow Xe_2^+ + e^-$	$\sigma = 2.0 \times 10^{-18}$ cm^2	19
2.18	$Xe_2^*(^1\Sigma_u^+, {}^3\Sigma_u^+) + Xe_2^*(^1\Sigma_u^+, {}^3\Sigma_u^+) \longrightarrow Xe_2^+ + Xe + Xe$	3.5×10^{-10} cm^3 sec^{-1} 8.0×10^{-11} cm^3 sec^{-1} 6.4×10^{-10} cm^3 sec^{-1}	34 20 24

the singlet $^1\Sigma_u^+$. At room temperature, $kT_r \approx 0.025$ eV and therefore atomic collitions will populate the triplet state preferentially. However Lorentz[19] noted that at high pressures the 172 nm fluoresence decay rate approaches asymptotically a value given by:

$$t^{-1} = \frac{3}{4}t_3^{-1} + \frac{1}{4}t_1^{-1} \qquad (2.19)$$

where t_3 =100 ns, the lifetime of the triplet[17] and t_1=5 ns the singlet lifetime[17]. This relation implies that the ratio of the populations of triplet to singlet is 3 : 1 which is the ratio of their statistical weights. At high pressures the two states must therefore be in thermal equilibrium.

Only thermalised electrons are energetic enough to achieve mixing of the two states. This would require the electron density to increase at high pressures. But at high pressures the electron density is observed to decrease in contradiction with Lorentz's predictions[20].

The model that appears to provide most of the answers was proposed by Werner et al[18]. The fluorescence and laser behaviour is explained in terms of the relative populations of the singlet and triplet states at different pressures coupled with losses arising from the photoionization of the excimers by 172 nm photons (eq 2.17, table 2.1).

The estimated values of the stimulated emission and photoionization cross sections of the two states indicate that only the singlet state can provide net gain, with the triplet providing net loss. At a constant pressure the instantaneous electron number density will determine the relative populations of the two states. At high pressures the electron number density is low[20]. The population of the triplet will therefore be favoured and the output power of

the laser is expected to decrease, in agreement with experimental observation.

The model also provides a formula[18] for the gain as a function of the populations of the two states. As the ratio of the populations of triplet to singlet increases the peak wavelength is predicted to move to longer wavelengths, in agreement with the observed red shift in xenon[21]. No such phenomenon is predicted for krypton or argon[18].

Ground state absorption has also been suggested as the cause of the red shift. An increase in pressure will produce transient ground state dimers which are able to absorb in the blue side of the 172 nm continuum. This will produce an apparent red shift to the peak wavelength. Ground state absorption can also expain why there is no monotonic increase in the laser power with increasing pressure. Higher number densities of ground state xenon atoms would imply greater probability of populating the lower laser level thus reducing the population inversion.

However the red shift has only been observed in xenon[21]. No report exists of any shift in krypton and a small blue shift has been observed in argon[21]. Werner[18] has also shown that the same model fails to account correctly for the variation of the laser output with pressure.

One phenomenon that no model can account for is the premature termination of lasing. It was observed by Gerardo and Johnson[22] that the laser intensity reaches a maximum and begins to decrease even though the gain in the system is still higher than the initial losses in the cavity. This phenomenon is even more evident when long excitation pulses ($\sim 10^{-6}$ s) are used. The shape of the fluorescence signal

follows the excitation current pulse thoughout the pumping duration where as lasing only lasts 100 ns and in some cases terminates while the fluorescence signal is still increasing[23,24]. Early theories as to the cause of premature termination included time dependent reflectivities of the cavity mirrors[25]. Fournier included it in his kinetic model[26] but it has since been shown[24] that the nature of the mirrors and their reflectivity is not the cause. Furthermore it has been reported[24] that pulse termination occurs in high pressure xenon operating in a superfluorescence mode where no mirrors are used.

Hoff et al[13] suggested absorption of ground state dimers formed by collisions at high temperatures as the cause of premature termination. Gas heating is accepted by Werner[27] but according to Werner what terminates lasing is the effect of high temperature on the stimulated emission cross section $\sigma_s(\lambda)$. At normal temperatures, lasing will occur over a range of wavelengths for which $\sigma_s(\lambda)$ is high enough so that the gain is greater than the loss at the same wavelength. At high temperatures the peak value of $\sigma_s(\lambda)$ decreases. Above a certain temperature, gain will be smaller than loss for all wavelengths and lasing will terminate. Recent estimates[24] show that this explanation alone fails to account for the observed behaviour.

The temporal profile of absorption losses was measured at 193 nm[23,28] but its behaviour cannot be accounted by the variation of any known parameter. An attempt to measure the absorption at 172 nm showed that there is a linear dependence between absorption and the atomic number density of xenon up to pressures of 30 atmospheres[21]. If the absorption was due

to transient ground state dimers then the absorption should be proportional to the square of the atomic number density. The linear dependence suggests the presence of an impurity. Oxygen and carbon monoxide impurities have been detected in the course of this work (see section 2.8) and it may be that impurities play an important role in the kinetics of the xenon excimer laser.

2.4 The high voltage generator

A brief description of the operation of the high voltage generator is given below. Details can be found elsewhere[35,36]. It was designed to deliver 750 kV peak voltage in a 60 ns pulse at a repetition rate of up to 10 H. Figure 3 shows its schematic diagram. It operated as follows: The primary capacitor was pulse-charged to 30 kV. The air pressure in the input spark-gap was adjusted so that the gap broke down when the input capacitor was fully charged. This caused the primary capacitor to discharge though the primary turns of the autotransformer. The secondary winding charged the peaking capacitor up to 750 kV. The pressure inside the output spark-gap was adjusted so that it broke down when the voltage of the peaking capacitor reached its maximum value. This voltage then appeared across the diode. A low pass filter was used in order to eliminate any prepulse effects and to short circuit the low frequency components of the voltage pulse.

The major disadvantages of this design were:

1) The lack of a pulse forming network. This meant that a nonuniform excitation pulse was provided so no temporal fluorescence studies could be performed. Furthermore, power was delivered to the xenon gas for periods longer than 60 ns,

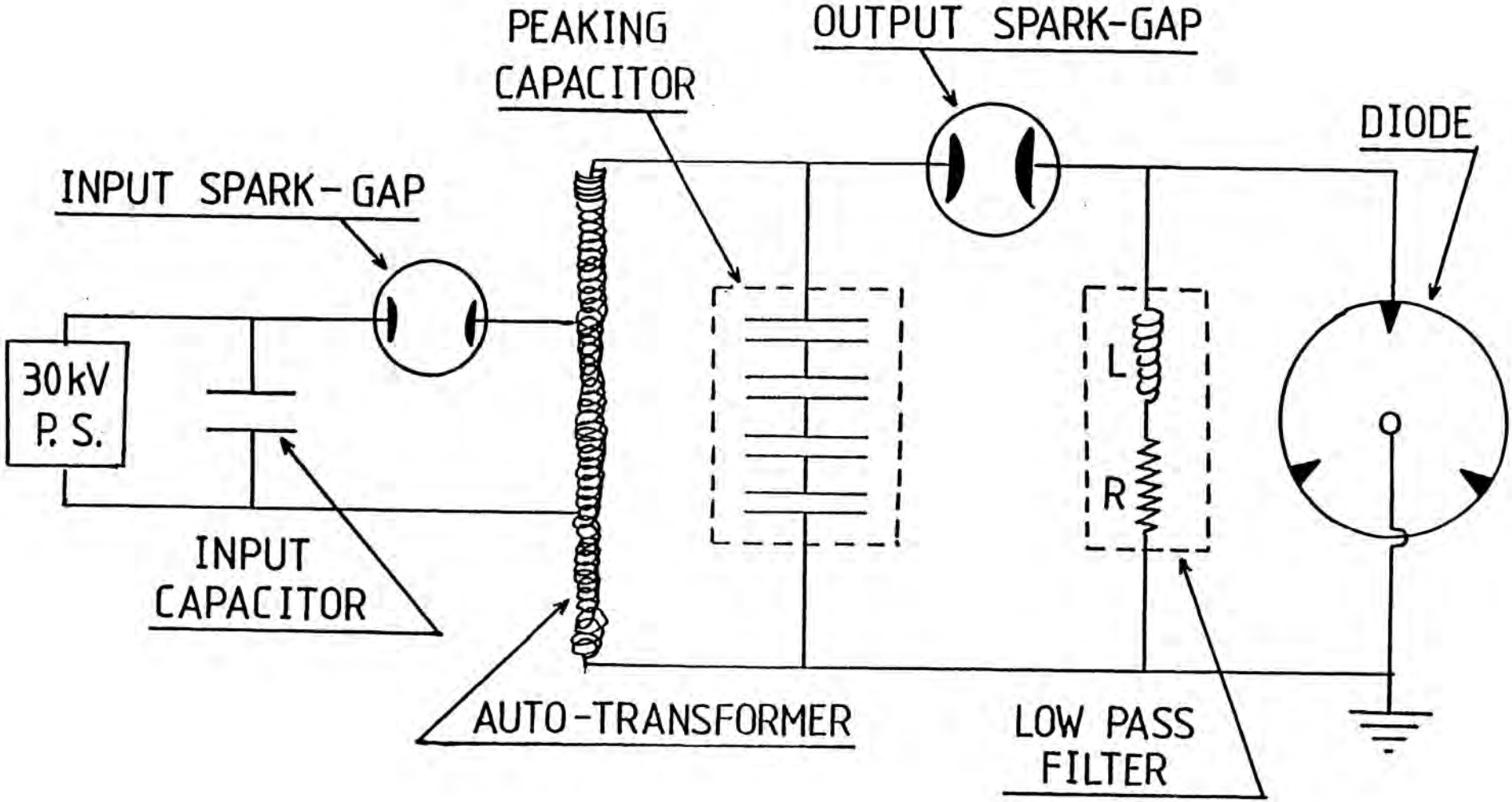


FIGURE 3 Schematic diagram of the high voltage generator.

long after the laser had terminated. This energy could only contribute to the heating of the gas which was a highly undesirable effect.

2) The reproducability of the energy deposited in the gas suffered because of the use of self-breakdown spark-gaps. For example, if the input spark-gap broke down when the voltage across the primary capacitor was δV below the normal breakdown voltage, this voltage defect was amplified by the gain of the auto-transformer . In some cases the voltage across the peaking capacitor would not rise high enough to break the output spark-gap so the freon insulation broke down and the energy stored in the capacitor damped itself to the outer earthed case.

Better operation was obtained when the pressure of the input spark-gap was increased sufficiently so that the gap would not break down even when the input capacitor was fully charged. The pressure was suddenly reduced by opening the exhaust valve. This ensured that the gap was firing only when the input capacitor was fully charged so the energy damped through the primary of the auto-transformer was constant from shot to shot.

3) Freon gas at atmospheric pressure was used to insulate and prevent an electrical breakdown within the generator. However, the insulating characteristics of low pressure freon are poor[37] compared with oil and this was the cause of breakdowns that could have been prevented had oil been used as the insulator.

2.5 The coaxial diode

Short pulse (<100 ns) excitation of xenon lasers requires the use of high pressures (~ 10 bar). High pressures

are necessary so that three body collisions can saturate, since the third body can always be guaranteed to be in the vicinity of a two body collision. Furthermore at high pressures rapid vibrational relaxation of the upper laser levels can occur, thus reducing the fluorescence bandwidth and consequently increasing the gain. But it is very difficult to operate stable discharges at high pressures[38] so electron beams are used exclusively.

The role of the electron beam is to transfer the energy from the high voltage generator to the high pressure gas. Electron beams require pressures less than 10^{-4} Torr to be generated. The high pressure lasing medium is separated from this vacuum by means of a thin ($\sim$ 50 μm) metal foil which the electrons can penetrate with small energy loss. This is the transverse mode of pumping.

Electrons in a high pressure gas soon loose their energy due to inelastic collisions[39] and acquire a mean deviation θ in their trajectories[40]. This implies that the energy deposition is not uniform throughout the gas[41].

The coaxial pumping geometry developed at Imperial College[42,43] uses a thin (25 to 50 μm) wall tube as its anode, thus providing cylindrical symmetry. Uniform energy deposition can be achieved with a $\pm$10% variation in the transmitted energy over the entire pumped length of the anode tube[42].

However, the coaxial system was shown to possess another advantage. If, for example, the anode tube diameter is reduced by a factor of two and the pressure of xenon inside is increased so that the electron beam energy is again completely deposited in the gas, then the supplied power density is now four times higher because the energy is deposited in $\frac{1}{4}$ of the

original volume.

Although this may appear obvious, it was never demonstrated until an increase in the supplied power density became necessary in the course of tuning this laser. Figure 4 shows a simple adaptor designed to allow the use of anode tubes of different diameters. Two such adaptors are necessary, one at each end of the tube. Using this arrangement the anode tube diameter could be changed within a few hours. Adaptors able to take anode tubes of 4mm, 6mm and 8mm diameter were constructed and these were found adequate for all subsequent work.

Energy deposition calculations indicate that the 8mm tube would provide the maximum laser energy output. Practice showed however that using the 6mm tube the laser output was higher and the laser operated more reliably. Tuning of the laser to the edges of the tuning range worked best with a 4mm diameter tube. Using an 8mm tube the laser was shown to be underpumped and highly susceptible to the presence of impurities in the gas.

Appendix A describes a new method of manufacturing thin wall anode tubes needed for this experiment.

2.6 Fluorescence studies of the xenon excimers

Spectral and temporal studies of the xenon fluorescence have been reported elsewhere[44]. Coaxial diodes are unsuitable for fluorescence studies because observation is restricted along the axis of the anode tube. Unless very low power densities are deposited in the gas, fluorescence amplification is expected to take place, thus distorting both the spectral and temporal profiles.

Temporal information were obtained using a solar blind

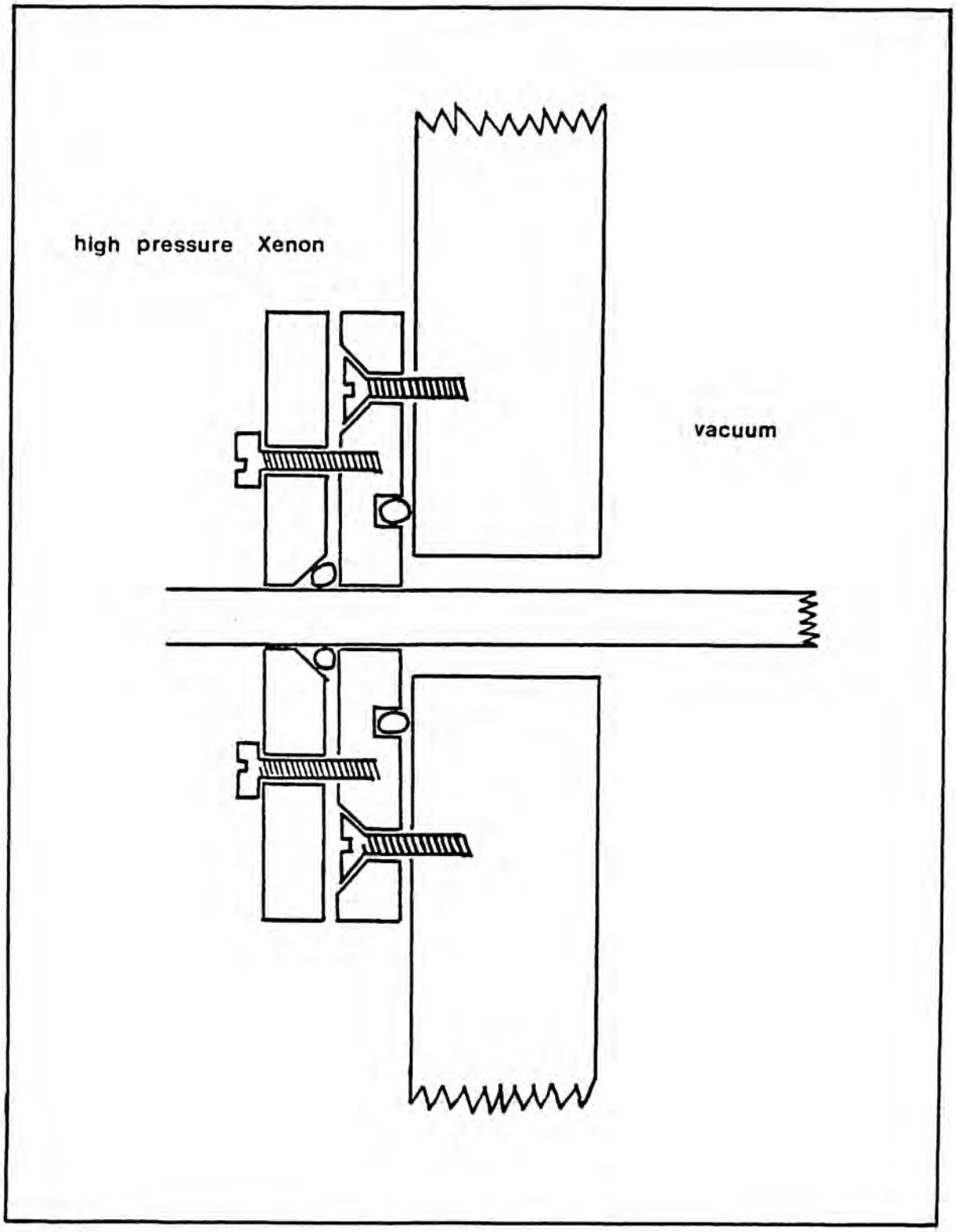


FIGURE 4

photodiode (ITT, type F4115) and displayed on a Tektronix type 519 oscilloscope. Stainless steel wire mesh was used to attenuate the light reaching the photodiode in order to prevent its saturation.

In order to show the effects of amplified spontaneous emission, the temporal profile of the fluorescence was recorded using an 8mm and a 6mm diameter anode tubes. Plate 1(a) shows the temporal profile of the fluorescence when an 8mm tube is used. The pulse rises sharply to a peak and decays slowly. Using a 6mm tube, however, there are two peaks in the fluorescence profile shown in plate 1(b). In order to investigate their origin a full reflector (R_{172nm}=97%) was placed at the far end of the anode tube. The size of the first peak remained the same whereas the second increased by approximately 30%, see plate 1(c). This indicated that the second peak was due to the gain in the excited gas. The nature of the second peak was investigated further in conjunction with the tuning of the laser (section 2.9).

When a 4mm diameter tube was used the gain was high enough so that up to 2 mJ was recorded due to the superfluorescence of the medium at 172 nm.

2.7 The untuned xenon laser

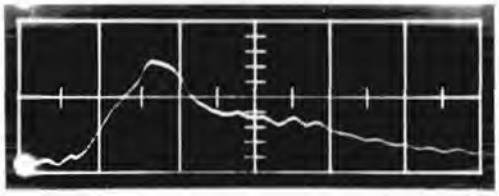
When optical feedback was provided at 172 nm, laser action was observed. Feedback was provided by plane multi-layer dielectric mirrors with MgF_2 substrates, obtainable commercially from Acton Research Corporation, in the U.S.A.. Low reflectivities were obtained from home made, 2 mm thick, single or double plate spectrasil etalons. A 20% reflectivity at 172 nm was estimated for a single etalon and a 76% transmission was measured at the same wavelength.

Plate 1(a) Temporal profile of the fluorescence emitted when an 8 mm diameter anode tube was used, pressurized with 10 bar of xenon, 10 ns/div.

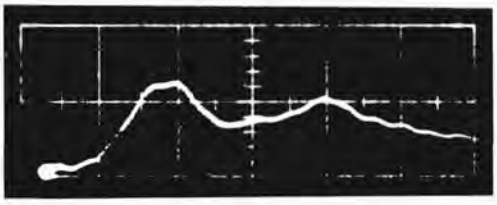
Plate 1(b) Temporal profile of the fluorescence emitted when a 6 mm diameter anode tube was used, pressurized with 12 bar of xenon, 10 ns/div.

Plate 1(c) Temporal profile of the fluorescence emitted when a 6 mm diameter anode tube was used, pressurized with 12 bar of xenon, with a 97% reflector placed at the far end of the tube, 10 ns/div.

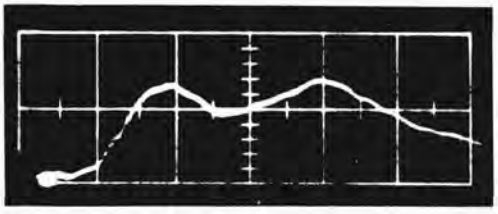
Plate 1(d) Temporal profile of the laser intensity obtained when a 6mm tube was pressurized with 12 bar of xenon The cavity consisted of a 97% reflector and a spectrasil etalon output coupler, 10 ns/div.



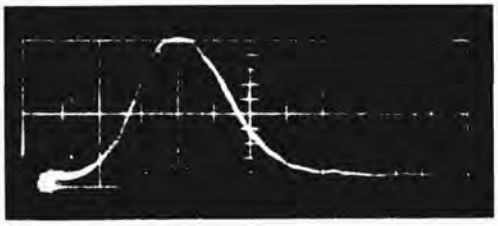
(a)



(b)



(c)



(d)

PLATE 1

The reflectors were mounted internally and alignment was achieved using pushrods driven through high pressure O-ring seals[36,44].

A typical laser intensity profile is shown in plate 1(d). A 6 mm anode tube was used with a cavity consisting of a full reflector and a single etalon output coupler. A Laser Instrumentation type L.R. calorimeter was used to measure the time integrated laser pulse energy. The pulse shown in plate 1(d) corresponds to an output energy of 32 mJ.

Spectral information were obtained using a home made one-meter spectrograph incorporating a 600 lines mm^{-1} concave grating blazed for maximum reflection at 90 nm. Spectra were recorded on Kodak type SC7 film and analysed on a Joyce Loebl microdensitometer. Second order spectra around 344 nm were generally recorded because of the x2 increase in the dispersion of the instrument. Furthermore, a low pressure mercury lamp could conveniently provide wavelength calibration lines on both sides of the laser spectrum.

Figure 5 shows the spectral characteristics of a pulse similar to the one shown in plate 1(d). The 167 nm calibration line corresponds to the first order 334nm mercury emission line. Two absorption bands are apparent and these were shown (see section 2.8) to be due to carbon monoxide impurity in the xenon gas.

2.7.1 Pressure optimization of the laser output

It was found experimentally that the two most important parameters that determine the laser energy output were the gas pressure and the mirror reflectivities. Although xenon pressure features strongly in all the kinetic models, its effect on the

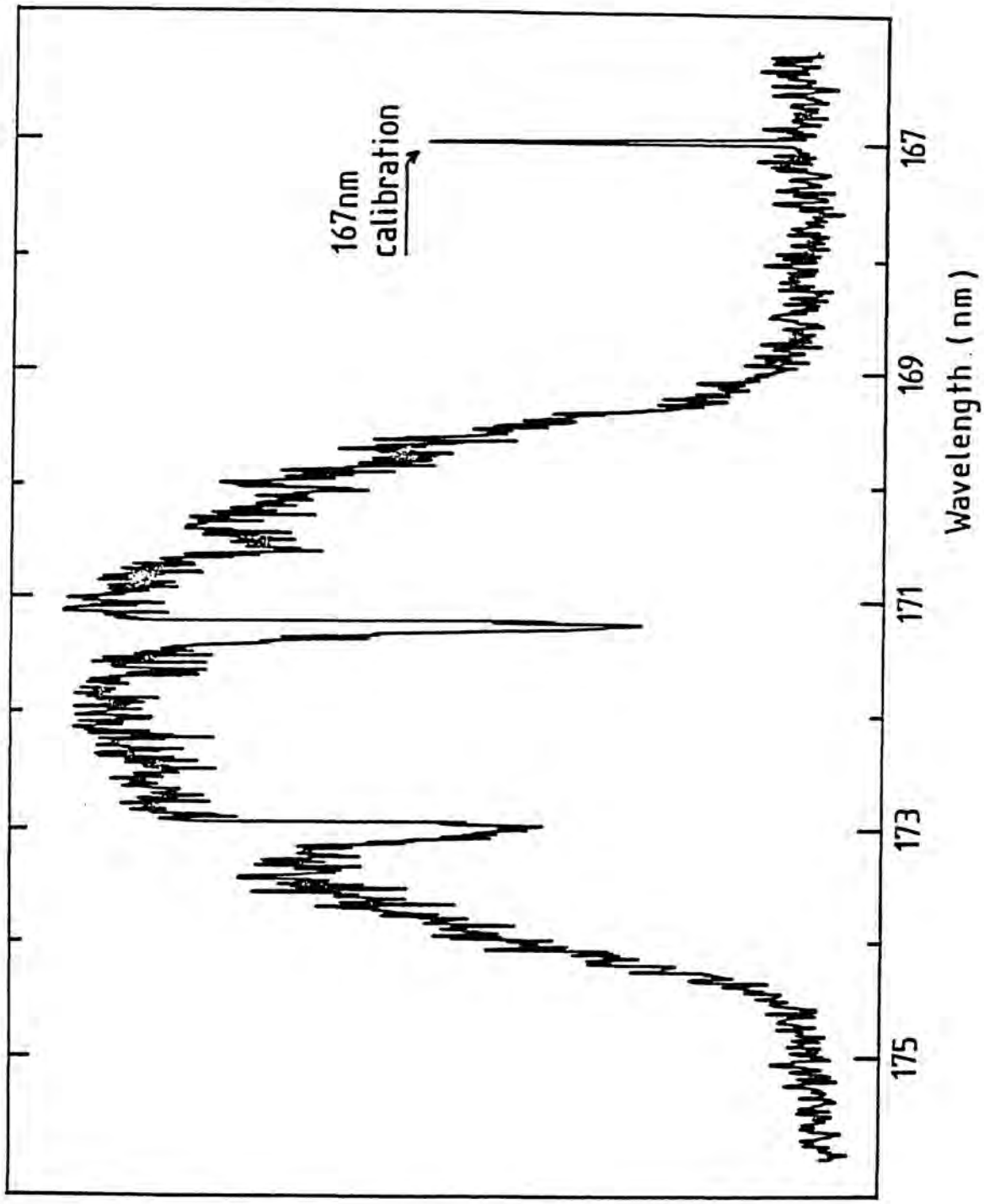


FIGURE 5

deposition of the electron beam energy in the gas appeared to dominate. It was found for example that when a 4 mm anode tube was used the laser energy output was increasing monotonically up to a pressure of 15 bar, the maximum pressure used. When an 8 mm tube was used an optimum pressure of 8.5 bar was observed[36]. Figure 6 shows the variation of the untuned laser output with pressure when a 6 mm tube was used, in combination with a full reflector and a single etalon output coupler. Maximum energy output was found to occur at 13 bar.

2.7.2 The red shift

The variation of the xenon gas pressure was found to have an effect on the spectral profile of the xenon laser. Figure 7 shows the variation of the peak wavelength of the laser spectrum with pressure. The peak wavelength is seen to shift towards the long wavelengths as the pressure is increased. This red shift was found to be in agreement with the observations of Hughes[45] and Werner[27]. A similar shift was reported[21,44] for the peak wavelength of the xenon fluorescence. This indicates that the peak net gain shifts to longer wavelengths as the pressure is increased. This phenomenon was used in the present work to aid the tuning of the laser towards the long wavelength edge.

2.7.3 Mirror optimization of the laser output

When the xenon gas was excited by the electron beam, some of the energy was stored in the gas in the form of excimers. Because of the short lifetime of the upper laser state (see section 2.3) the storage capacity of the xenon excimers was expected to be low. Excimers were lost via Penning ionization or by radiative decay. It was therefore vital to allow the

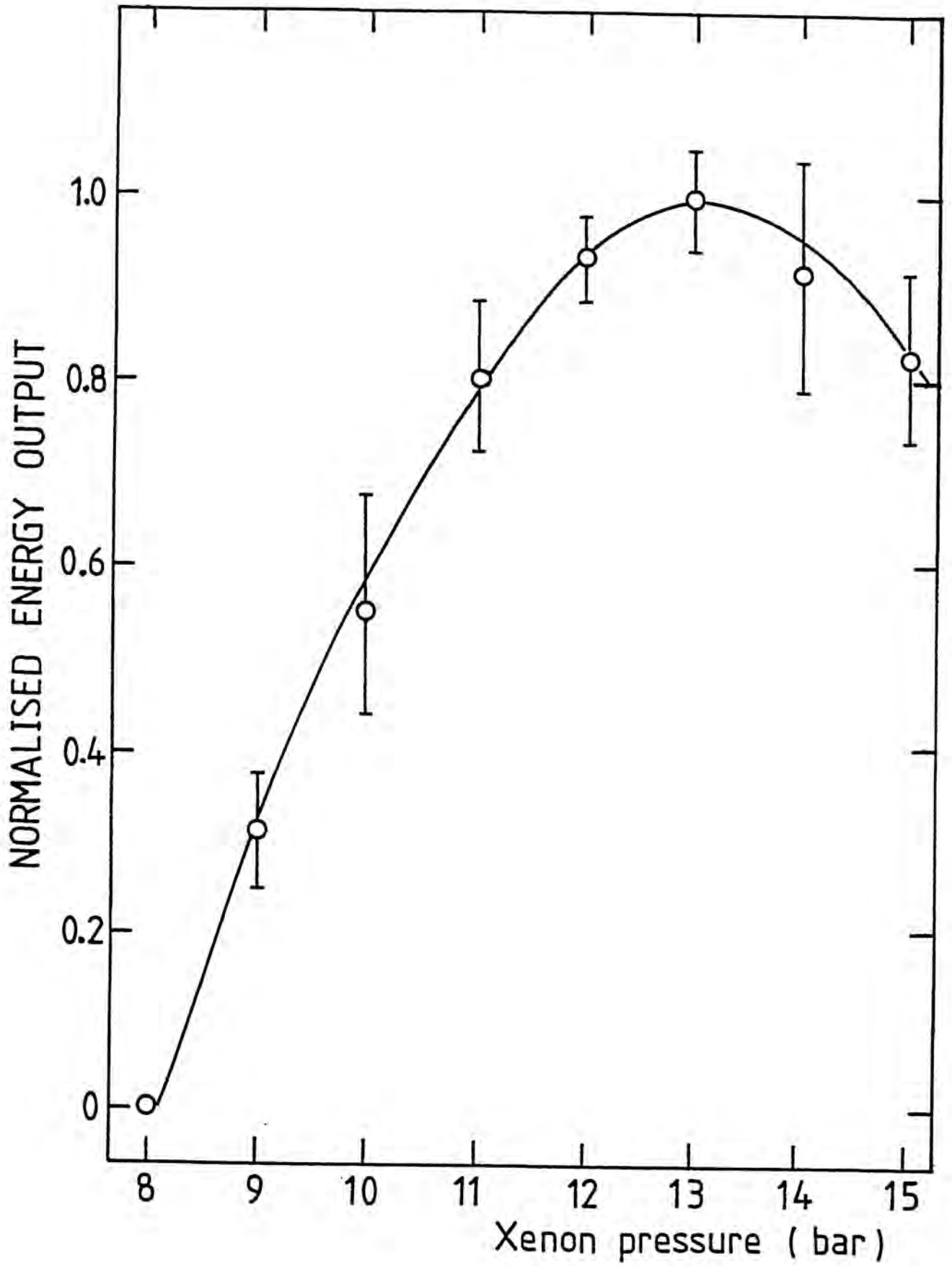

NORMALISED ENERGY OUTPUT
1.0
0.8
0.6
0.4
0.2
0
8
9
10
11
12
13
14
15
Xenon pressure (bar)

FIGURE 6

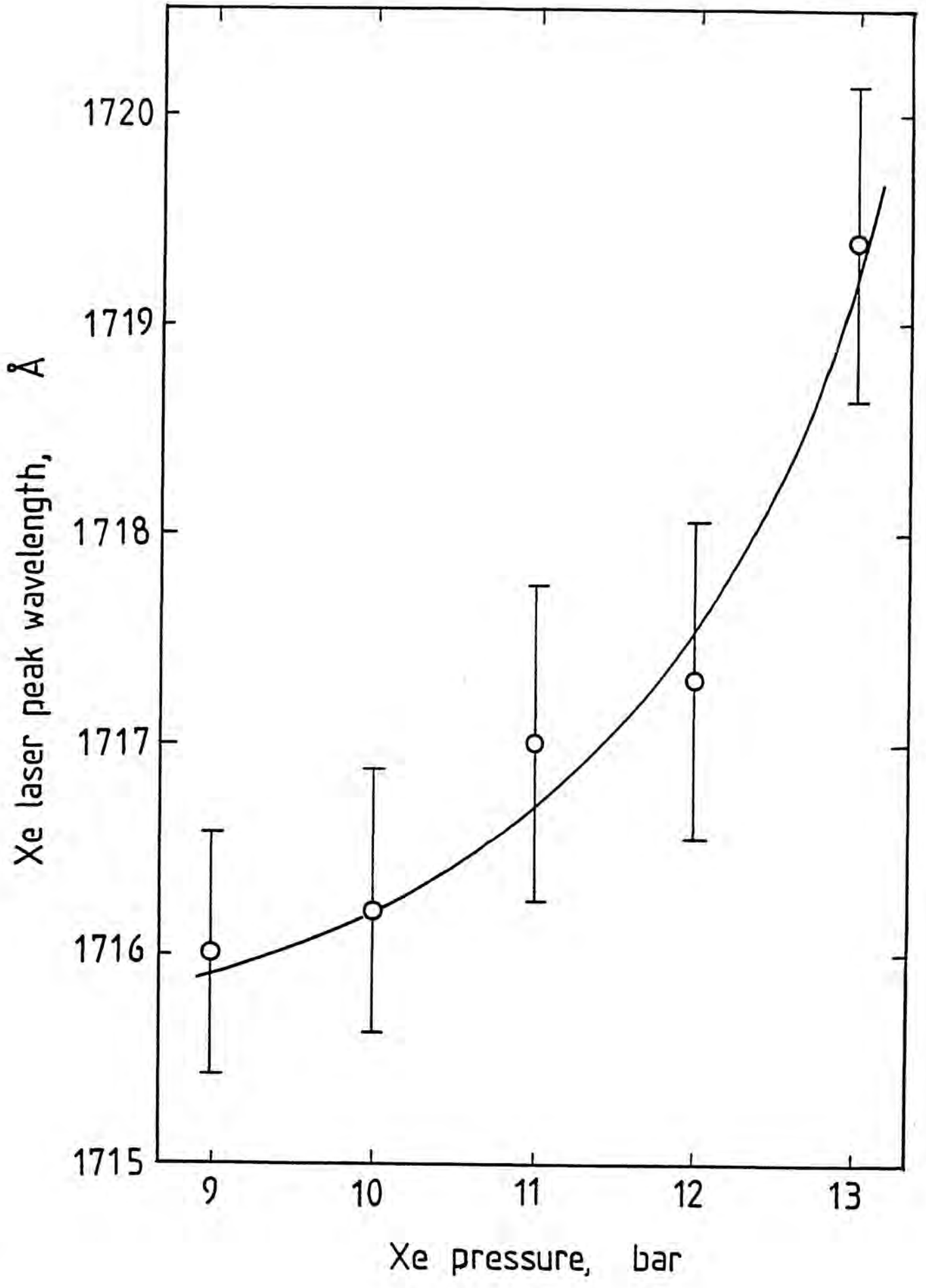

1720
1719
1718
1717
1716
1715
Xe laser peak wavelength, Å
9
10
11
12
13
Xe pressure, bar

FIGURE 7

laser flux to build up quickly so that it could successfully compete with other loss mechanisms for the energy stored in the excimers. On the other hand the output mirror had to be transparent enough so that a large fraction of the cavity flux escaped to form the laser beam.

For every pumping configuration there was an output mirror reflectivity for which optimum energy output occured. Figure 8 shows the variation of the energy output of the laser, with the product of the mirror reflectivities, R_1R_2 , for a 6 mm and an 8 mm anode tube at 12 bar and 8.5 bar respectively.

When a 6 mm tube was used, optimum energy output occurred for values of R_1R_2 considerably smaller than when an 8 mm tube was used. This was explained by the fact that with the 6 mm tube the gain was expected to be higher, thus allowing the saturation flux to be reached with a cavity of lower Q.

The fact that the optimum energy output for the 8 mm tube was only 12 mJ indicated that in the 8 mm tube the gain was low enough so that the saturation flux was never reached even for cavities with high values of Q. No such plot could be made when the 4 mm anode tube was used. In this case the gain was high enough to allow the intra-cavity flux to build up beyond the damage threshold of the cavity optics even when an etalon was used as an output coupler. Pulse energies of 16 mJ were measured which correspond to an output energy density of 130 mJ cm^{-2}. This was the maximum energy density obtained from this system.

2.7.4 Damage of the optical components

One of the most important limitations in the operation of high power lasers is the damage that can occur to optical components. Non linear optical effects and breakdown in solids

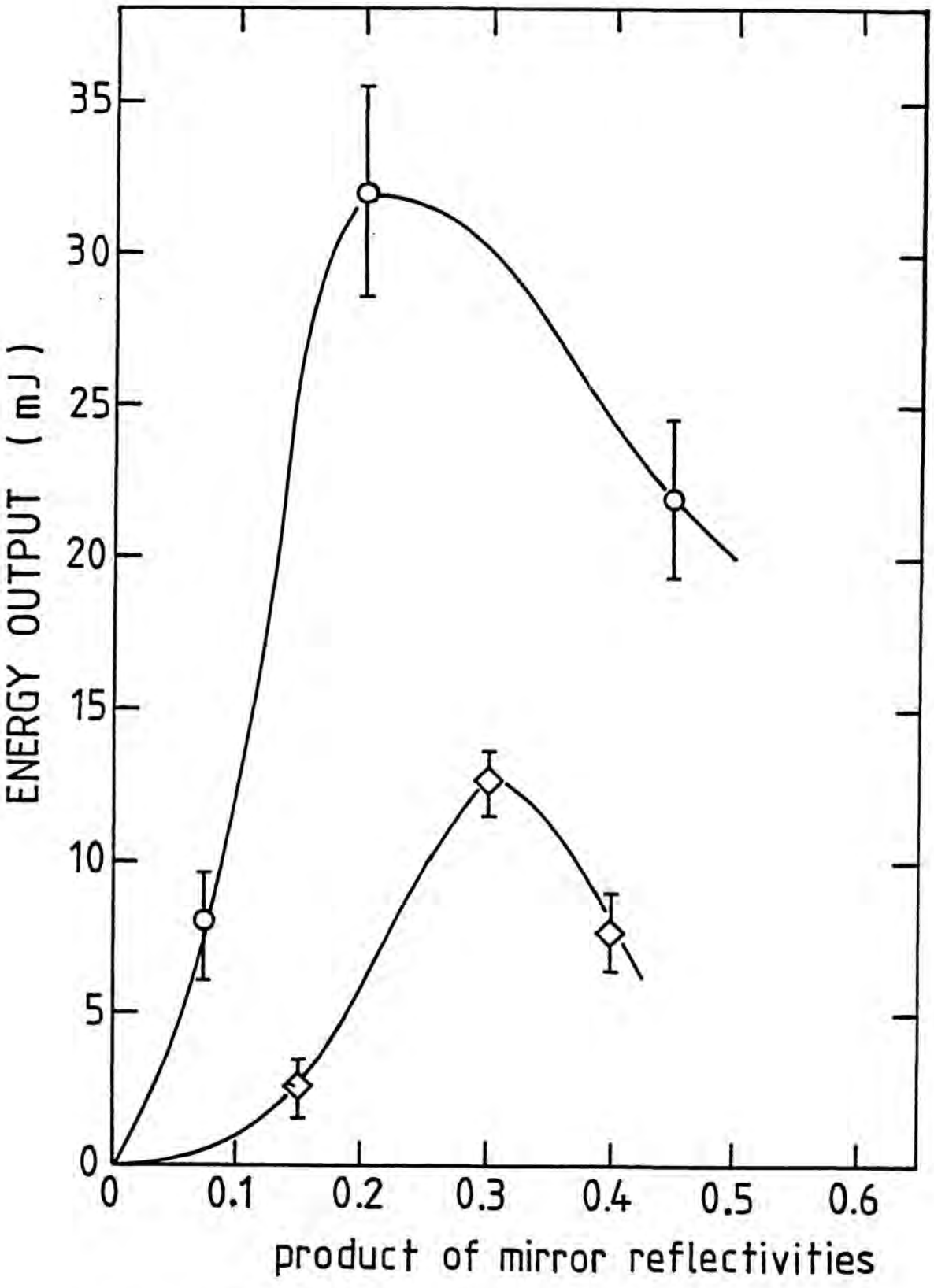

ENERGY OUTPUT (mJ)
35
30
25
20
15
10
5
0
0
0.1
0.2
0.3
0.4
0.5
0.6
product of mirror reflectivities
—o—o—o— 6mm anode tube diameter
—◇—◇—◇— 8mm " " "

FIGURE 8

are found to be the causes. However, at 172 nm optical absorption by all solids is significant with subsequent thermal stresses. Furthermore, two photon absorption becomes an important effect at short wavelengths[46]. These effects are expected to cause damage throughout the thickness of the optical components.

It was found experimentally that the most serious damage occurred on surfaces exposed to high power fluxes of VUV light. This caused the reduction to their optical reflection and transmission coefficients. The cause of the damage was identified with the presence of hydrocarbon molecules in the cavity. Passage of VUV photons through, say, a barium fluoride window could produce some photoelectrons from the surface of the crystal thus generating a net positive charge on the surface. Oil molecules floating in the cavity are much more likely to deposit where there was a net charge to aid attachment. This effect has also been observed elsewhere[47]. During long periods of idleness the cavity was pressurized with xenon in order to reduce the mean free path of the oil molecules thus preventing them from depositing on the surface of the optical components.

Oil molecules form a thin film that absorbs strongly in the VUV. Passage of 172 nm radiation heats the oil film and fuses it to the surfaces. The heat generated can produce cracks on the surface of the crystal. Examination of a damaged surface using a stylus technique showed that deposition had taken place on the damaged parts of the surface. Some deep recessions (cracks) were also detected.

Multi-layer dielectric mirrors were used to provide reflectivities higher than 40%. The higher the reflectivity of the mirror, the larger the number of dielectric layers needed. Some absorption was expected to take place in the dielectric



Dielectric mirror (R_{172} = 97%) damaged by the intracavity flux of the Xenon laser.

PLATE 2

with a subsequent increase in its temperature. This in turn could cause damage to the mirror coating.

With 48% reflectors, damage was slight and the reflectivity of the mirror decreased to a value such that the intra-cavity flux that could be sustained could cause no further damage to the mirror. This was not found to be the case with the 98% reflectors. Plate 2 shows a magnified section of the surface of a mirror which has been exposed to high intra-cavity flux. The heat generated in the mirror coating had caused it to flake off until the bare MgF_2 substrate was exposed. This was a common phenomenon when a 4 mm anode tube was used.

2.8 The identification of the impurities

It was mentioned with reference to figure 5 that the two absorption bands seen in the output spectrum of the untuned laser were due to carbon monoxide impurity. The emission spectrum of a particularly contaminated xenon gas is shown in figure 9(a). Four absorption bands are visible and were found to correspond in wavelength, intensity and shape with the four emission bands of a CO discharge, shown in figure 9(b).

Table 2.2 identifies the transitions giving rise to the absorption bands. They are all shown to originate from the ground state of the CO molecule.

The most widely believed reason for the origin of the CO impurity is the evolution of carbon from the stainless steel anode tube. This combines with oxygen to form carbon monoxide.

However, monitoring the amount of CO present in the cavity over the period of three years suggested that it originated from the breakdown of large hydrocarbon molecules and in particular from diffusion pump oil molecules backtracking and

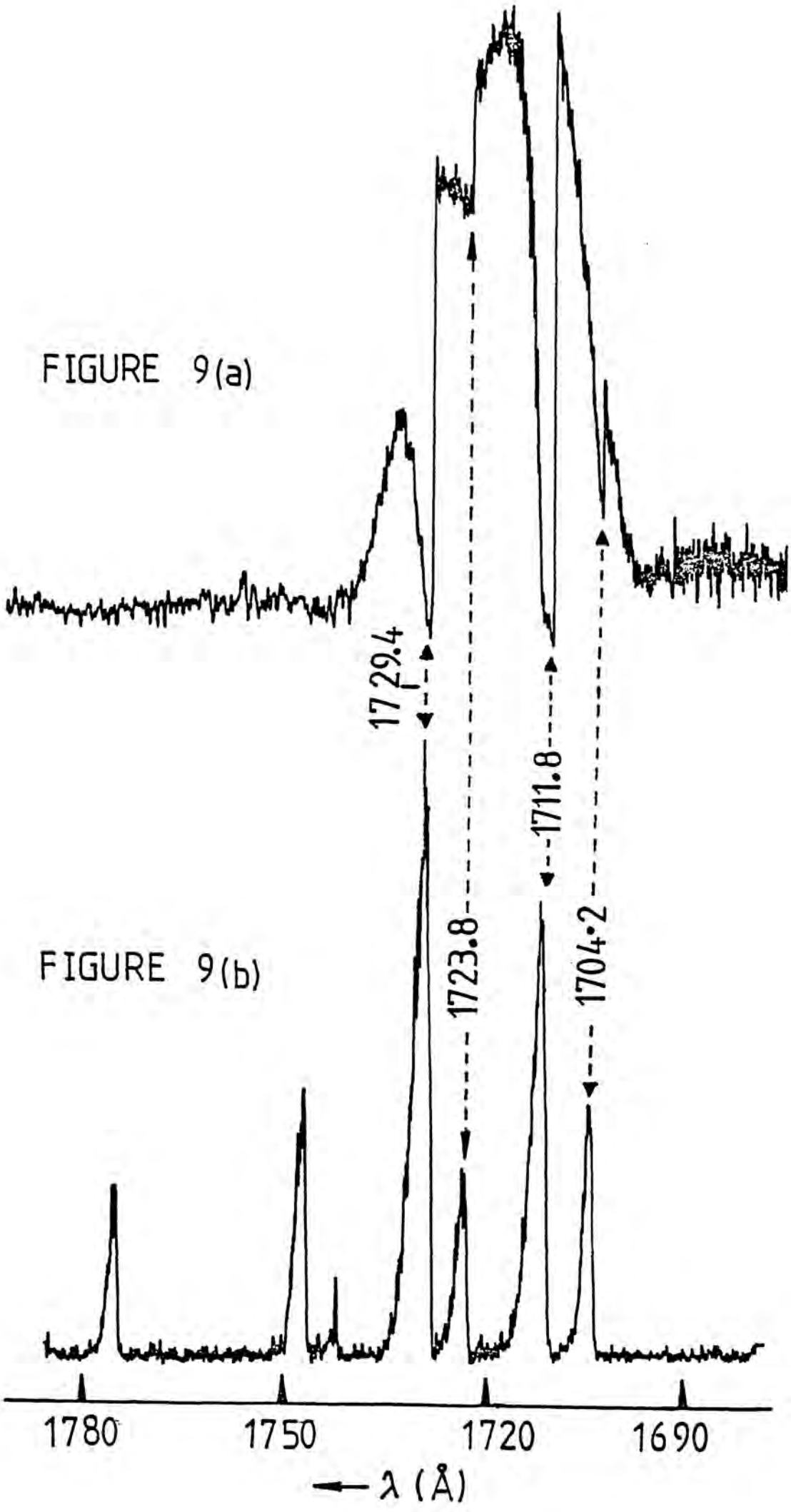


FIGURE 9(a)

FIGURE 9(b)

TABLE 2.2

Wavelength (Å)	Wavenumber (cm^{-1})	Transition	v'	v''
1704.5	58675	$A(^1\Pi) \rightleftharpoons X(^1\Sigma^+)$	6	7
1705.2	58644	$A(^1\Pi) \rightleftharpoons X(^1\Sigma^+)$	3	5
1712.2	58404	$A(^1\Pi) \rightleftharpoons X(^1\Sigma^+)$	0	3
1723.8	58011	$A(^1\Pi) \rightleftharpoons X(^1\Sigma^+)$	4	6
1729.3	57827	$A(^1\Pi) \rightleftharpoons X(^1\Sigma^+)$	1	4
1731.4	57757	$a^1(^3\Sigma^+) \longleftarrow X(^1\Sigma^+)$	2	0

finding their way to the cavity. Hydrocarbons have been detected in the cavity (see section 2.7.4).

2.8.1 The origins of the visible bands

During the fluorescence studies of the photodissociation products of the mercuric halides (see chapter 5), a visible band system around 540 nm was detected which could not be attributed to any of the emissions from the halides. This band system was subsequently found to originate from the xenon laser itself. The rest of the spectrum was examined and a second band was seen at 310 nm. These bands have already been observed by Koehler[21], Hull[44] and Viecelli[48]. The latter[48] developed a theoretical model that suggests that the 310 nm band originates from the radiative recombination reaction:

$$Xe^{+} + e \longrightarrow Xe^{*} + h\nu(310nm) \qquad (2.20)$$

In order to resolve the mystery of their origin, a systematic study of these bands was undertaken. Figure 10 shows the spectrum of the 540 nm band. Two bands were identified and found to originate from the XeO excimer. The main band system is due to the transition:

$$XeO(2^{1}\Sigma^{+}) \longrightarrow XeO(1^{1}\Sigma^{+}) + h\nu(540nm) \qquad (2.21)$$

Figure 11 shows the energy level diagram of XeO as calculated by Dunning and Hay[49]. The weaker 570 nm band was identified with the transition[50]:

$$XeO(2^{1}\Sigma^{+}) \longrightarrow XeO(^{1}\Pi) + h\nu(570nm) \qquad (2.22)$$

From the XeO energy level diagram shown in figure 11 another band is predicted due to the transition:

$$XeO(2^{1}\Sigma^{+}) \longrightarrow XeO(^{3}\Sigma^{-}) + h\nu \qquad (2.23)$$

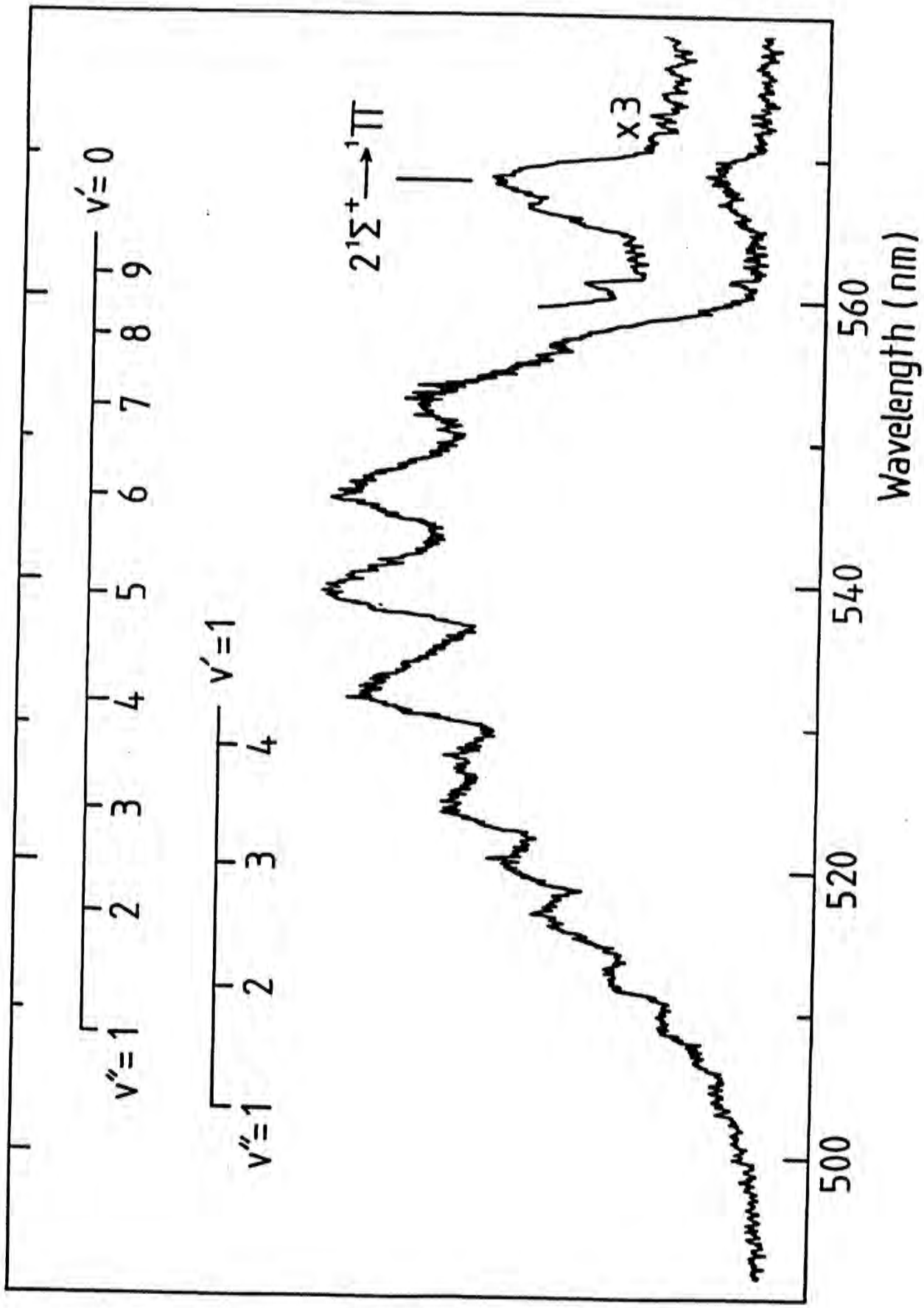
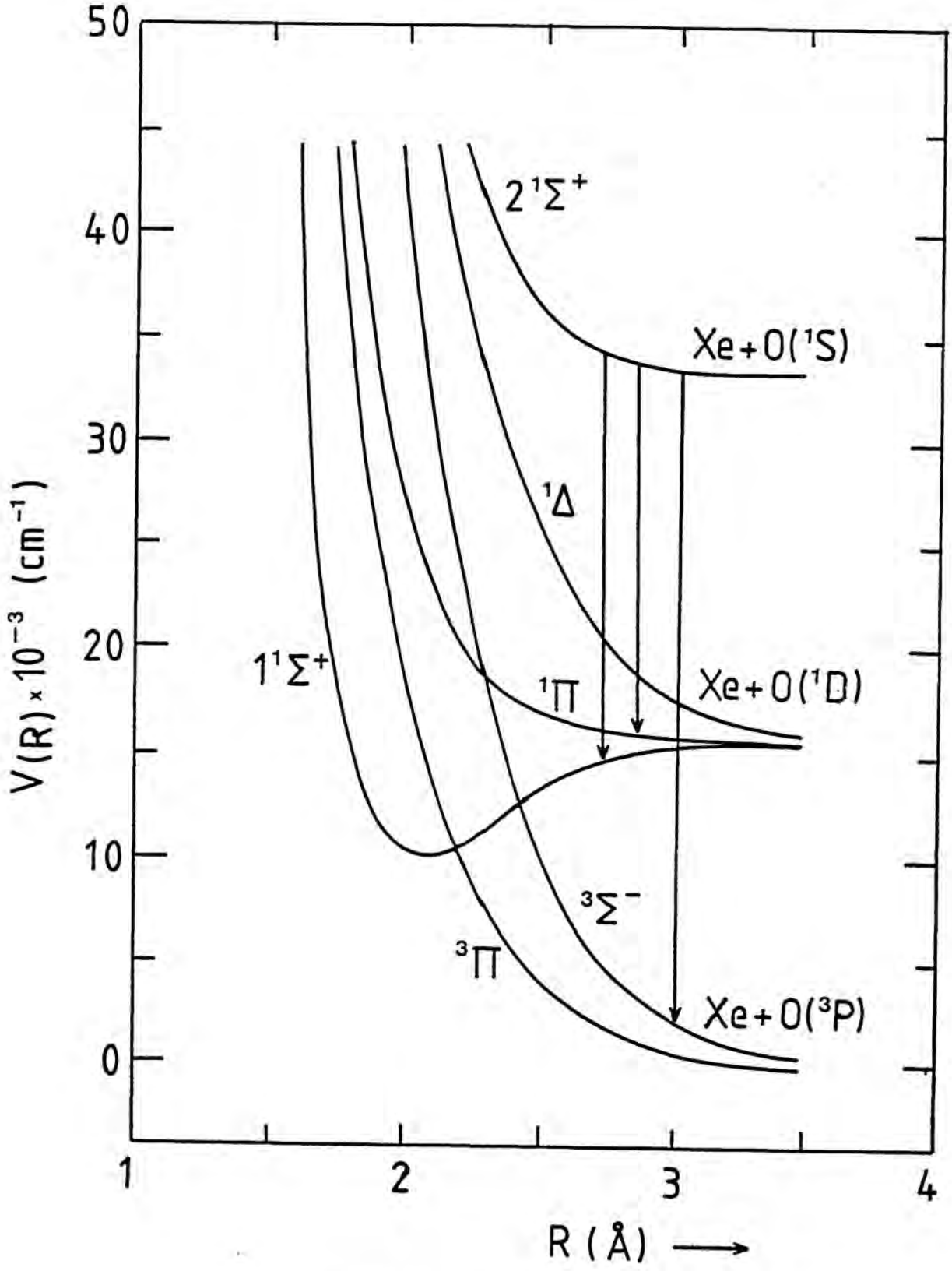

XeO visible bands
v'=0
v''=1 2 3 4 5 6 7 8 9
v'=1
v''=1 2 3 4
$2^1\Sigma^+ \rightarrow {}^1\Pi$
x3
500 520 540 560
Wavelength (nm)

FIGURE 10



ENERGY LEVELS OF XeO

FIGURE 11

Energy considerations showed that this transition would emit in the 300 nm region. Indeed, such a band was observed at 310 nm. Furthermore it had a narrow bandwidth and no structure was resolved. These are the characteristics of an emission band corresponding to the transition described by eq. 2.23 .

Viecelli's suggestion[48] must be wrong because the process of association described by eq. 2.20 should give rise to a broad emission continuum, just like the process of dissociation i.e. photoionization gives rise to absorption bands of many tens of nanometers bandwidth.

The XeO 540 nm band has recently been studied extensively because its upper state is basically an $O(^1S_0)$ state perturbed by a ground state Xe atom[51,52]. As it will be shown in the next chapter the $^1S_0$ states of group VI_A elements appear promising for high storage laser amplifiers, with possible uses in laser fusion.

The emission of XeO bands from the laser medium suggested the presence of atomic oxygen donor impurity. Analysis of a typical xenon laser gas sample by the Analytical Services Laboratory of Imperial College showed that it contained up to 90 parts per million molecular oxygen impurity[36]. Oxygen molecules absorb strongly in the region 169 to 175 nm (see chapter 1). Absorption produces its photodissociation:

$$O_2(X^3\Sigma_g^-) + h\nu(172\ nm) \longrightarrow O(^1D) + O(^3P) \qquad (2.24)$$

Quenching of the xenon upper laser state by an oxygen molecule produces the same products:

$$O_2(X^3\Sigma_g^-) + Xe_2^+(^3\Sigma_u,\ ^1\Sigma_u) \longrightarrow O(^1D) + O(^3P) + 2Xe \qquad (2.25)$$

Both processes are destructive for the oxygen molecule and therefore bleaching of all the oxygen molecules was expected

to take place.

Collision of an oxygen atom with a xenon excimer was expected[53] to lead to the population of $XeO(2^1\Sigma^+)$. Another possible pathway for the production of the $2^1\Sigma^+$ state may be via the production of the ionic pair Xe^+O^-. Comparison with the Xe^+F^- excimer shows that the ionic state Xe^+O^- must be in the vicinity of the $XeO(2^1\Sigma^+)$ valence state. Possible curve crossing of the two states may cause the predissociation of the ionic to the valence state.

It is interesting to note that in high pressure argon excitation, emission bands at 190 nm and 218 nm have been observed[21]. These bands have not been identified with any known transitions but at least the 190 nm band is thought to be due to an impurity[21]. It is interesting that the Ar^+F^- emission occurs at 193 nm. The ionic pair states of Ar^+F^- and Ar^+O^- are expected to be similar because of the similarity of the constituent ions. It is therefore suggested that Ar^+O^- is the source of the 190 nm band. No predissociation of the Ar^+O^- state can occur because the ionic state if lying approximately 2 eV higher than the $ArO(2^1\Sigma^+)$ valence state.

2.8.2 Gas handling and gas purification

The output of the xenon laser was found to decrease with time when the same gas was used for more than 50 shots. High output could be restored by purifying the gas. A number of purification methods were used.

One of the most effective and versatile techniques consisted of storing the xenon in a 0.1 litre cylinder at high pressure. The temperature was slowly reduced by gradually immersing it in liquid nitrogen. The vapour pressure of xenon

at 77 K, the boiling point of nitrogen, is 0.01 Torr. The cylinder was then opened to the much larger volume of the cavity (~2 lt) and its temperature was allowed to rise slowly. When the pressure in the cavity reached 10 Torr, the cylinder was closed and heated back to room temperature. The cavity was evacuated and the same procedure could be repeated.

This purification method is only effective for contaminants whose boiling point is much lower than the boiling point of xenon. It was found to remove the oxygen impurity and was partly successful with the carbon monoxide impurity.

The other important contaminant, water, was prevented from reaching the laser cavity by distilling the xenon gas from a reservoir whose temperature was kept below 200 K. The vapour pressure of ice at 200 K is 4×10^{-4} Torr, which gives a water impurity content below 0.05 parts per million.

2.9 The tuning of the xenon excimer laser

One of the advantages of using xenon at high pressure is that the vibrational relaxation of the excimers is fast[54]. This implies that the energy stored in the excimers can be extracted in a narrow spectral bandwidth, provided the extraction time is long compared with the relaxation time of the upper state. Long extraction times are required to allow the repopulation of the states depleted by stimulating emission.

Laser tuning can be achieved by introducing a dispersive element in the cavity, so that feedback is only provided over a narrow frequency bandwidth. Tuning of the xenon excimer laser has been reported using a prism as the dispersive element[55,44,36]. Diffraction gratings have been considered

unsuitable[44,36] because of their low reflectivity at 172 nm and the low damage threshold of their reflective coatings.

Tuning of the argon excimer laser has recently been reported[56,57] using a diffraction grating, so a similar technique was applied here for the tuning of the xenon excimer laser.

The insertion of a tuning element in the laser cavity was observed to increase the laser threshold pumping power density. The tuning element thus introduced significant losses in the cavity. The aim of the present work was to compare the performance of different dispersive elements in tuning the xenon excimer laser. An investigation of the parameters affecting the tunability was also carried out.

2.9.1 Tuning using a 1200 lines mm^{-1} diffraction grating

Initially a 1200 lines mm^{-1} grating was used, blazed for maximum reflection at 121 nm. The grating was mounted on a system of gimbals[57], so that the axis of rotation was parallel to the grating grooves. Rotation was achieved using an external micrometer driving a pushrod through a high pressure O-ring seal. A 6 mm diameter anode tube was used, with the cavity pressurized with 12 bar of xenon.

When an etalon was used as the output coupler and the cavity tuned to 172 nm, there was a x3 increase in the fluorescence signal. This was an indication that the feedback provided by the etalon and the grating was not enough to sustain oscillation. Powerful lasing was observed when the etalon was replaced by a 48% reflector at 172 nm.

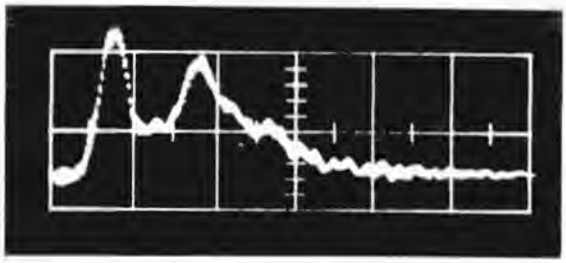
Plate 3 illustrates the tuning characteristics of the xenon excimer laser. The laser output is shown at four different

Plate 3(a) Temporal profile of the output emitted when the cavity was tuned to 160 nm, 20 ns/div.

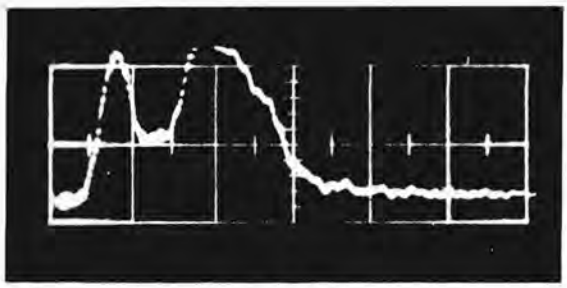
Plate 3(b) Temporal profile of the output emitted when the cavity was tuned to 169 nm, 20 ns/div.

Plate 3(c) Temporal profile of the output emitted when the cavity was tuned to 170 nm, 20 ns/div.

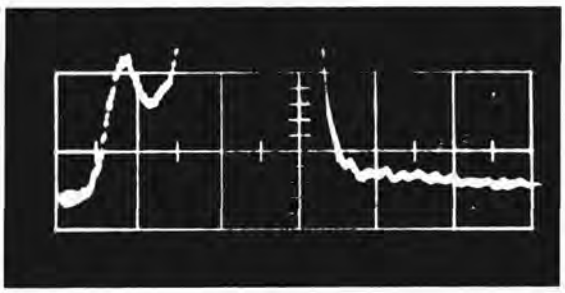
Plate 3(d) Temporal profile of the output emitted when the cavity was tuned to 172 nm, 20 ns/div.



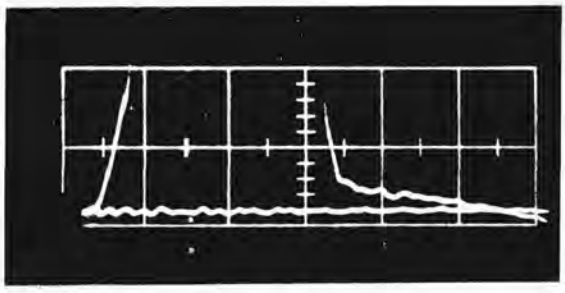
(a)



(b)



(c)



(d)

PLATE 3

wavelengths, where the excited gas can provide different values of net gain. Plate 3(a) shows the temporal profile of the output when the cavity was tuned to 160 nm. No net gain was expected at 160 nm and the output is identical to the fluorescence profile obtained when the grating was removed from the cavity altogether.

Tuning the cavity to 169 nm produced a x2 increase in the size of the second peak, whereas the first peak remained unaffected (see plate 3(b)). This implied that there was a net gain at 169 nm, but the feedback provided by the cavity was too low for the intra-cavity flux to build up. In this case most of the energy stored in the excimers was lost to Penning ionization or to spontaneous emission. Efficient tuning of the xenon laser could only be achieved when the intra-cavity flux was allowed to build up quickly to its saturation value, so it could compete successfully against other loss mechanisms for the energy stored in the excimers. Lasing at 169 nm could be improved by increasing the gain and / or increasing the quality factor, Q, of the cavity.

Tuning the cavity to 170 nm, where the gain was expected to be higher, produced a more powerful output, shown in plate 3(c). The size of the first peak still remained unaffected, but out of its fluorescence builds up the intra-cavity flux. The size of the second peak was many tens of times the magnitude of the fluorescence. However, lasing could still be improved since there was a time lag between the appearence of the fluorescence and the onset of laser oscillation.

Increasing the gain still further could decrease the build up time of the intra-cavity flux. Plate 3(d) shows the output obtained when the cavity was tuned to 172 nm, the middle of the

tuning range, where the gain was expected to be maximum. The intra-cavity flux was then seen to build up immediately and this was the most efficient form of tuning.

Using the 1200 lines mm^{-1} grating, output energies up to 12 mJ were obtained at 172 nm. However examination of the spectral profile of the output showed the F.W.H.M. to be up to 1.4 nm. Figure 12 plots the F.W.H.M. of the output, represented by error bars, at different wavelengths. Circles indicate the position of the peak wavelength.

2.9.2 Tuning using a 3600 lines mm^{-1} diffraction grating

A reduction of the output bandwidth was achieved by employing a more dispersive grating. The new grating had 3600 lines mm^{-1} and was blazed for maximum reflection at 160 nm. Very poor tuning was observed when the grating was used in a cavity in combination with a 48% reflector. Increasing the reflectivity of the output coupler to 68%, improved lasing enormously. Output energies up to 1 mJ were obtained around 172 nm. Figure 13 shows the spectral profile of the output at 170.8 nm. The F.W.H.M. of the tuned output remained constant at $\sim$0.25 nm over the entire tuning range of the laser.

The spectral brightness of the output obtained when the 3600 lines mm^{-1} grating was used, was a factor of three lower than the value obtained with the 1200 lines mm^{-1} grating. However, the spectral narrowing achieved with the 1200 lines mm^{-1} grating was only a factor of two narrower than the bandwidth of the untuned laser. Using the more dispersive grating, however, the bandwidths obtained were an order of magnitude narrower than those of the untuned laser. An even narrower output should

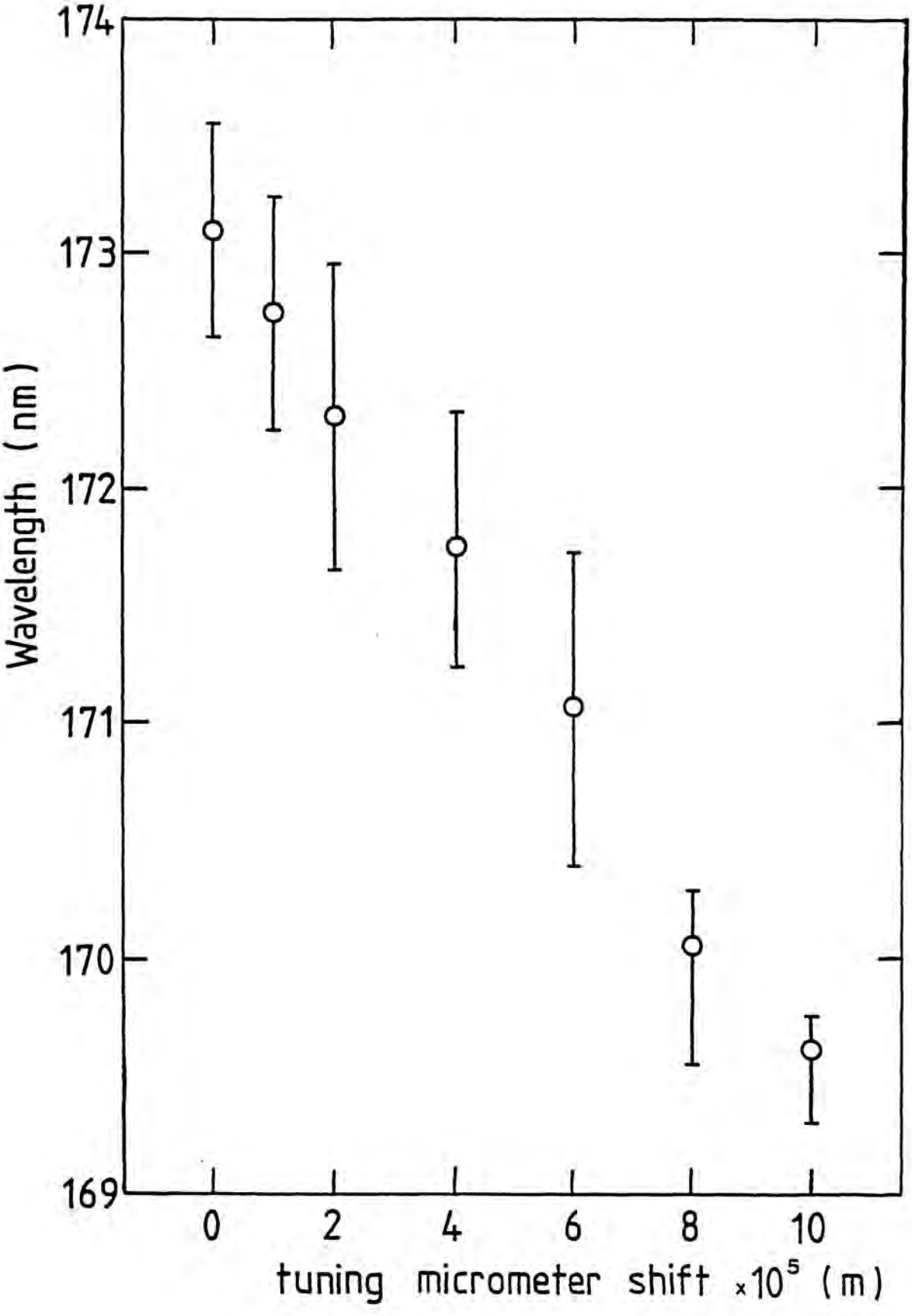

174
173
172
171
170
169
Wavelength (nm)
0
2
4
6
8
10
tuning micrometer shift x10^5 (m)

FIGURE 12

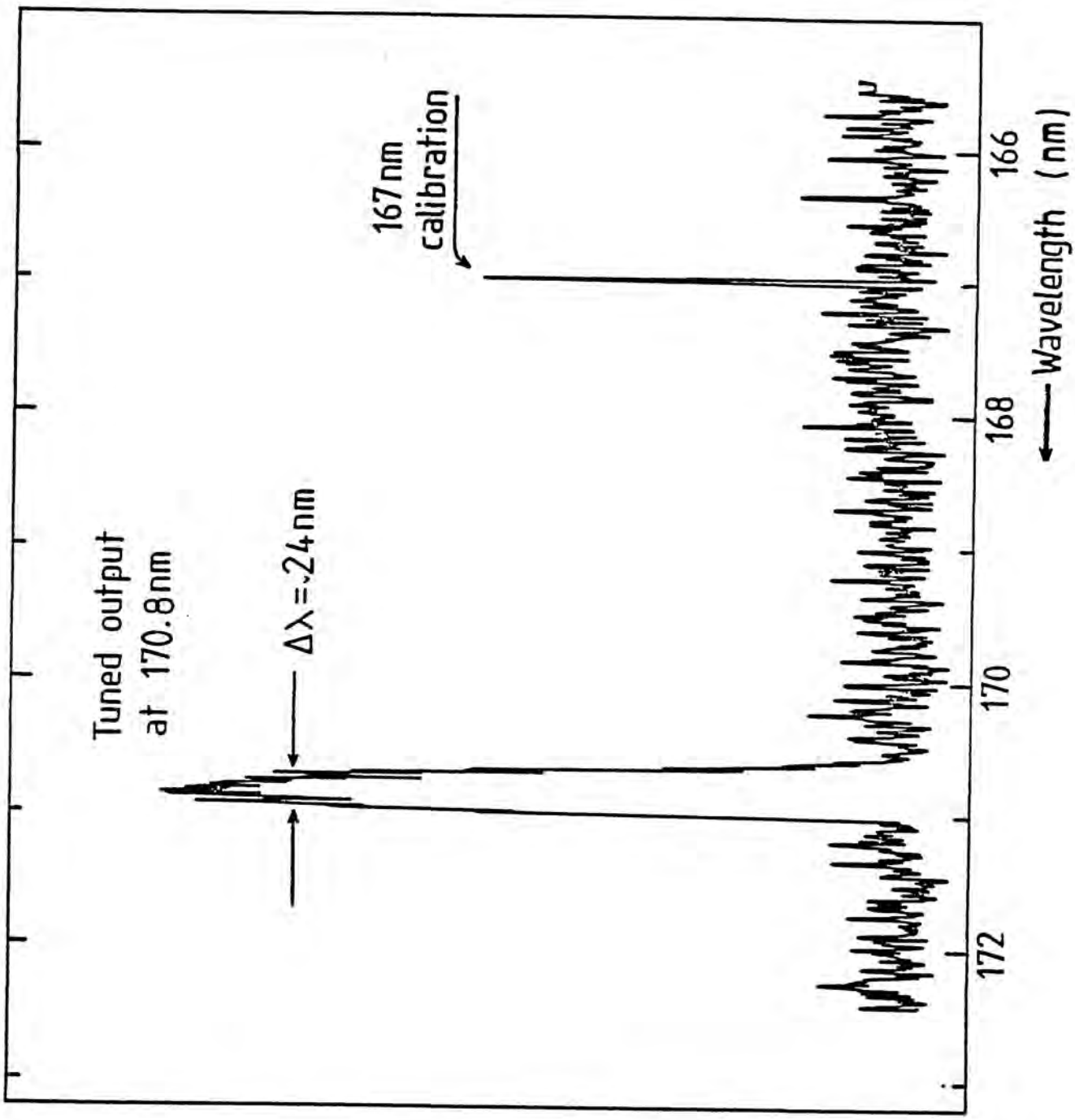

Tuned output
at 170.8nm
Δλ=.24nm
167nm
calibration
166
168
170
172
Wavelength (nm)

FIGURE 13

be obtained if a more dispersive grating is used. Plans are also under way to tune the laser using the "grazing incidence" technique[58,59].

No damage to optics was observed when the 3600 lines mm^{-1} grating was used, whereas serious damage to the reflective coating of the 1200 lines mm^{-1} grating was observed which limited its lifetime to approximately 40 shots.

2.9.3 Tuning using a spectrasil prism

Operation in the visible part of the spectrum has shown that prisms have a much higher damage threshold than diffraction gratings[60]. When operating in the VUV, a prism can provide another advantage over a grating. Its dispersion increases as the resonant wavelength moves near the absorption cut off of the prism material. The prism used here was made of spectrasil B because of its high dispersion[61] at 172 nm, while it still retains a high transmission coefficient at the same wavelength.

Details of the design and alignment of the prism tuning element can be found elsewhere[44,36]. The aim of the present work was to identify the parameters contributing to the tuning of the xenon excimer laser when a prism was used as the dispersive element.

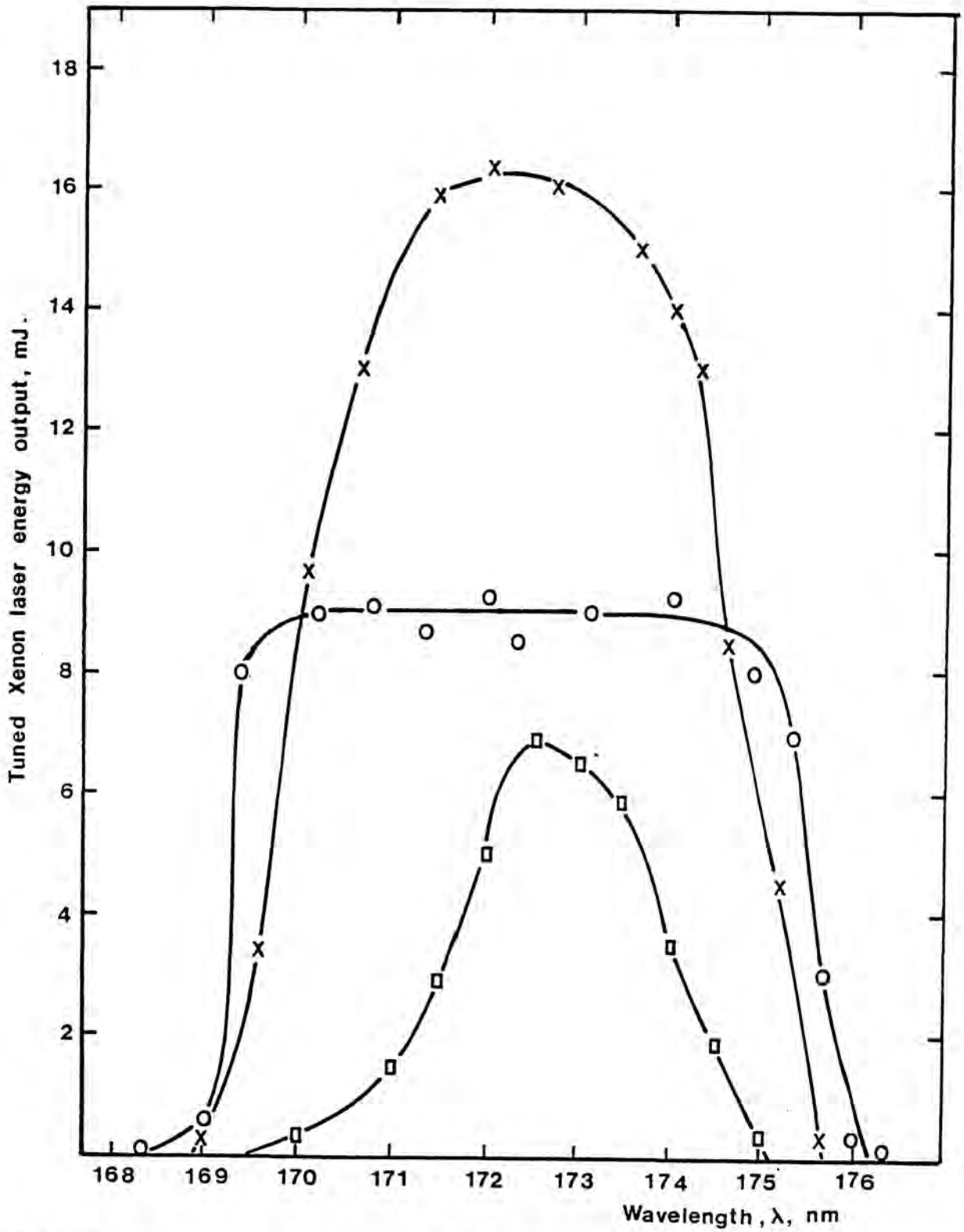
Efficient tuning can be achieved when the intra-cavity flux at the resonant wavelength λ_q is allowed to build up rapidly and convert the energy stored in the excimers, to laser radiation. The quality factor $Q(\lambda_q)$ of the cavity at λ_q, together with the gain $G(\lambda_q)$ that can be provided by the medium at the same wavelength, were identified and examined in detail.

The nature of the lasing transition suggests that the gain

is wavelength dependent. For a certain cavity configuration, tuning will be most efficient around 172 nm where the gain is maximum. The same cavity may not be able to sustain oscillation when tuned to 169 or 175 nm, the two extreme wings of the tuning range. This was found to be the case when the 8 mm diameter anode tube was used in combination with a 68% reflector. Figure 14(a) shows the tuned energy output for such a configuration. An output energy of 7 mJ was recorded in the middle of the tuning range, while very weak oscillation occurred at 170 and 175 nm. Using an etalon as the output coupler, no tuning could be observed, indicating low gain over the entire tuning range.

Gain was increased by reducing the anode tube diameter. Using a 6 mm anode tube, efficient tuning was obtained over a wider wavelength range, even when an etalon was used as the output coupler. Figure 14(b) shows the tuned energy output at different wavelengths for such a configuration. Examination of the spectral profile of the tuned output indicated that the F.W.H.M. did not remain constant over the entire tuning range Figure 15 shows the spectral profile of the output at 170.7 and 172.1 nm. The F.W.H.M. had a value of 0.5 nm at the centre of the tuning range and decreased to 0.38 nm at 170.7 nm.

The increase of the bandwidth of the tuned output as the laser was tuned towards the middle of the tuning range was to be expected. The dispersion of the tuning element implied that the quality factor of the cavity was wavelength dependent. Lasing could occur over a wavelength bandwidth $\delta\lambda_0$ around λ_0 for which the Q of the cavity could sustain oscillation, for the gain provided by the medium around λ_0. If the laser was tuned to a new wavelength λ_1, the Q of the cavity retained its shape but the wavelength where the Q of the cavity was



(a): —o—o—: With 4mm anode tube and 48% output coupler

(b): —x—x—: With 6mm anode tube and etalon

(c): —□—□—: With 8mm anode tube and 68% output coupler

FIGURE 14

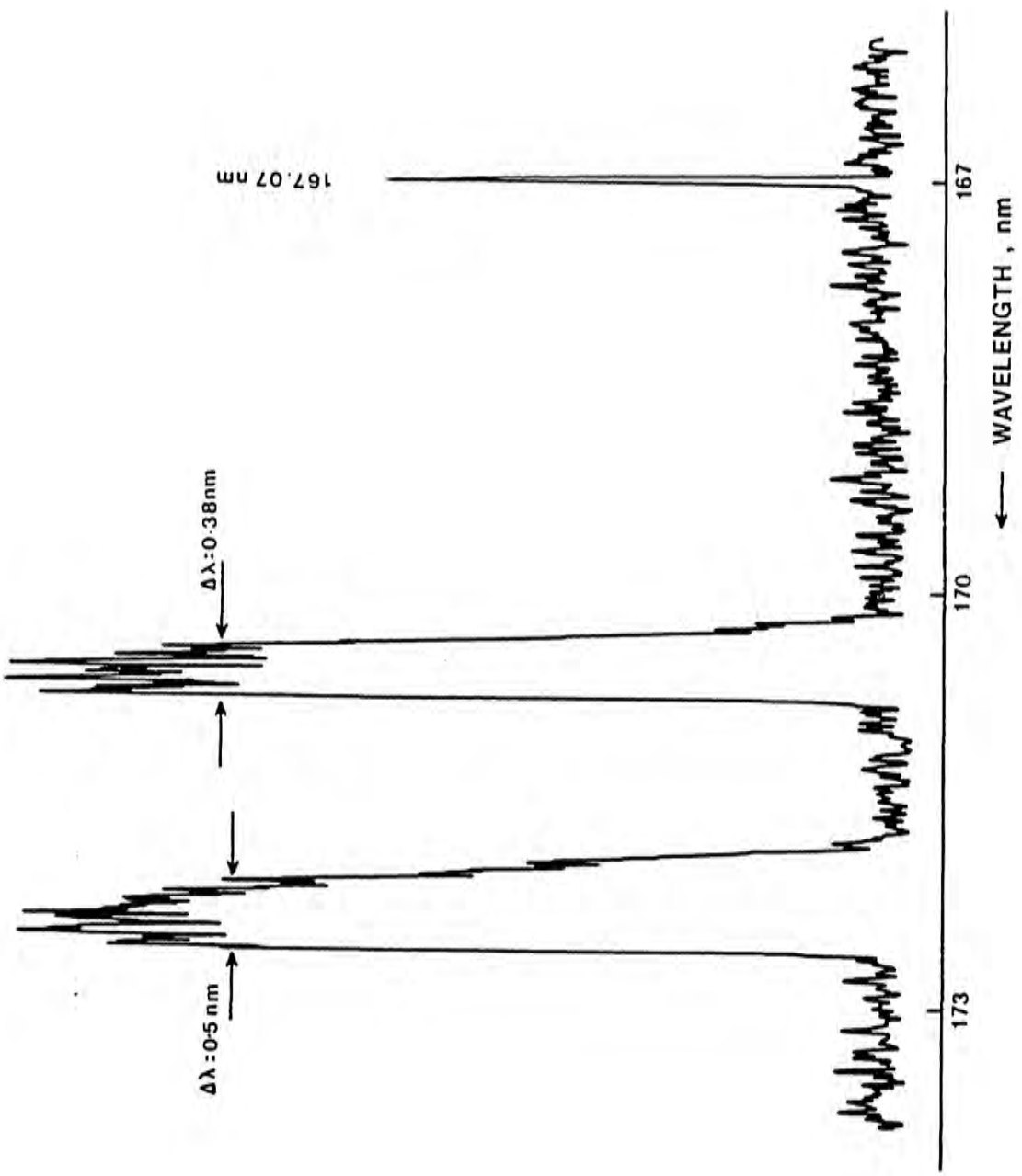


FIGURE 15

maximum was shifted to λ_1. If the gain around λ_1 was higher, then the cavity ought to be able to sustain oscillation over a wider bandwidth, $\delta\lambda_1$, because with higher gain lasing threshold could be achieved with a cavity of lower Q.

Further evidence that the gain determined the laser bandwidth was provided by tuning the laser to 171.2 nm, so that it coincided with the carbon monoxide absorption band (see section 2.8). Figure 16(b) shows the spectral profile of the output at 171.2 nm. Comparison with the output at 171.9 nm (shown in figure 16(a)) indicated that the CO absorption had reduced the net gain at 171.2 nm so that only weak lasing occurred at that wavelength. Lasing is a severe loss mechanism. Prevention of lasing allowed the gain to be higher on either side of the CO absorption band. Oscillation was thus observed on either side of 171.2 nm, even though at these wavelengths the Q of the cavity was expected to be lower than at 171.2 nm. If the CO impurity was absent, the output at 171.2 nm would have resembled the output at 171.9 nm, shown in figure 16(a).

When a 4 mm diameter anode tube was used, a new regime of operation of the tuned laser was found. The cavity consisted of the prism tuning element and a 48% output coupler. The combination of high gain and relatively high Q caused the intracavity flux to build up very quickly over the entire tuning range. Figure 14(c) shows the tuned energy output at different wavelengths for this configuration. Plate 4 shows the tuned output spectra at five different wavelengths. The spectral profile of the output retained a F.W.H.M. value of 0.25 nm over the entire tuning range (see figure 17).

FIGURE 16(a)

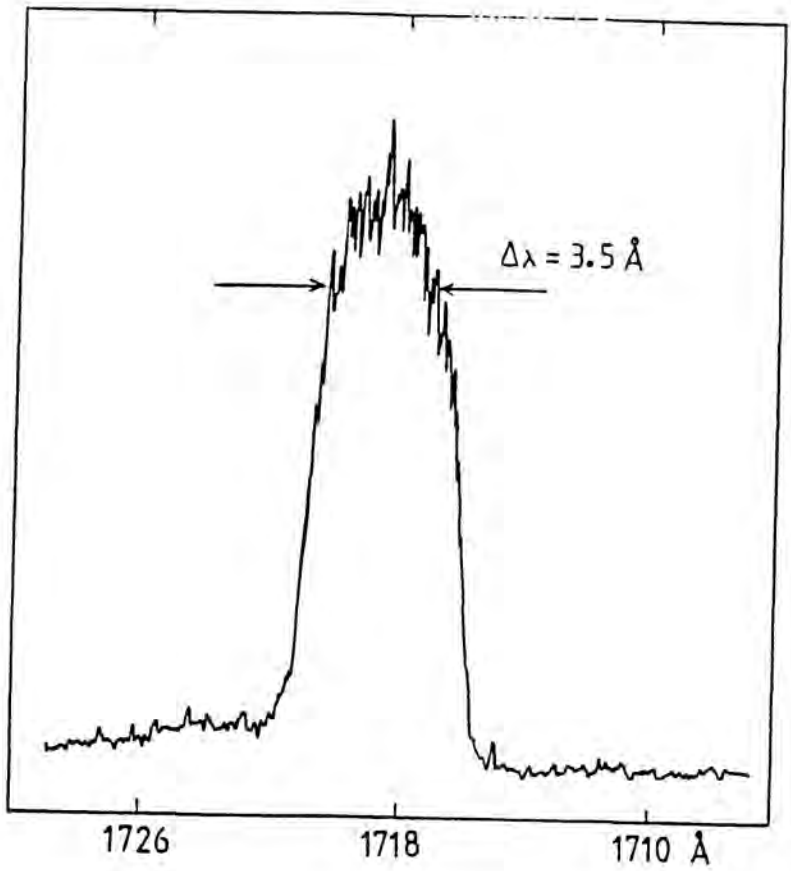
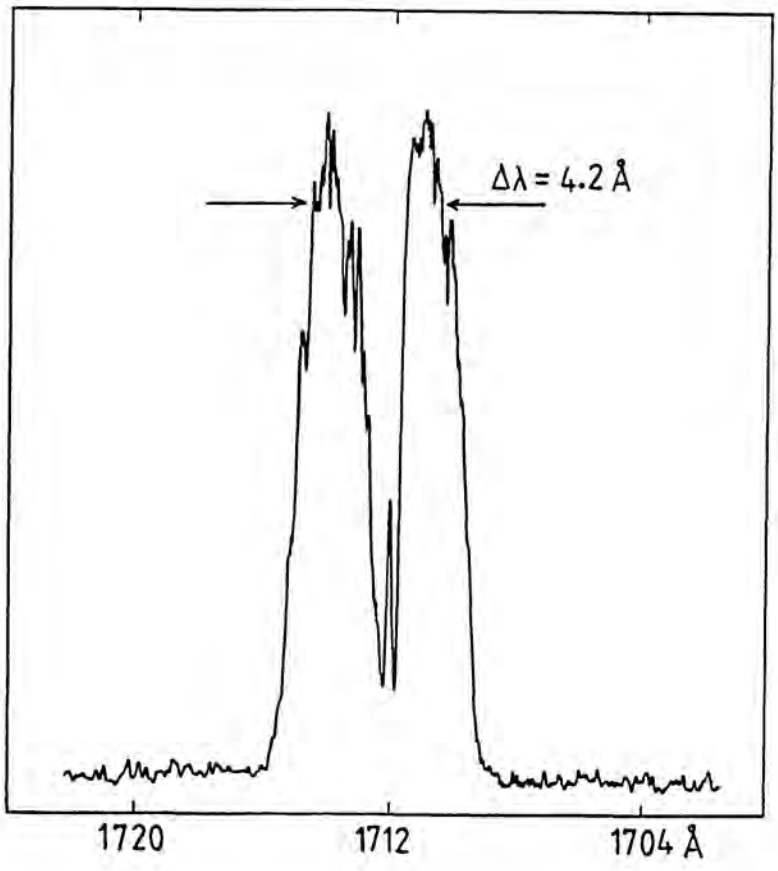
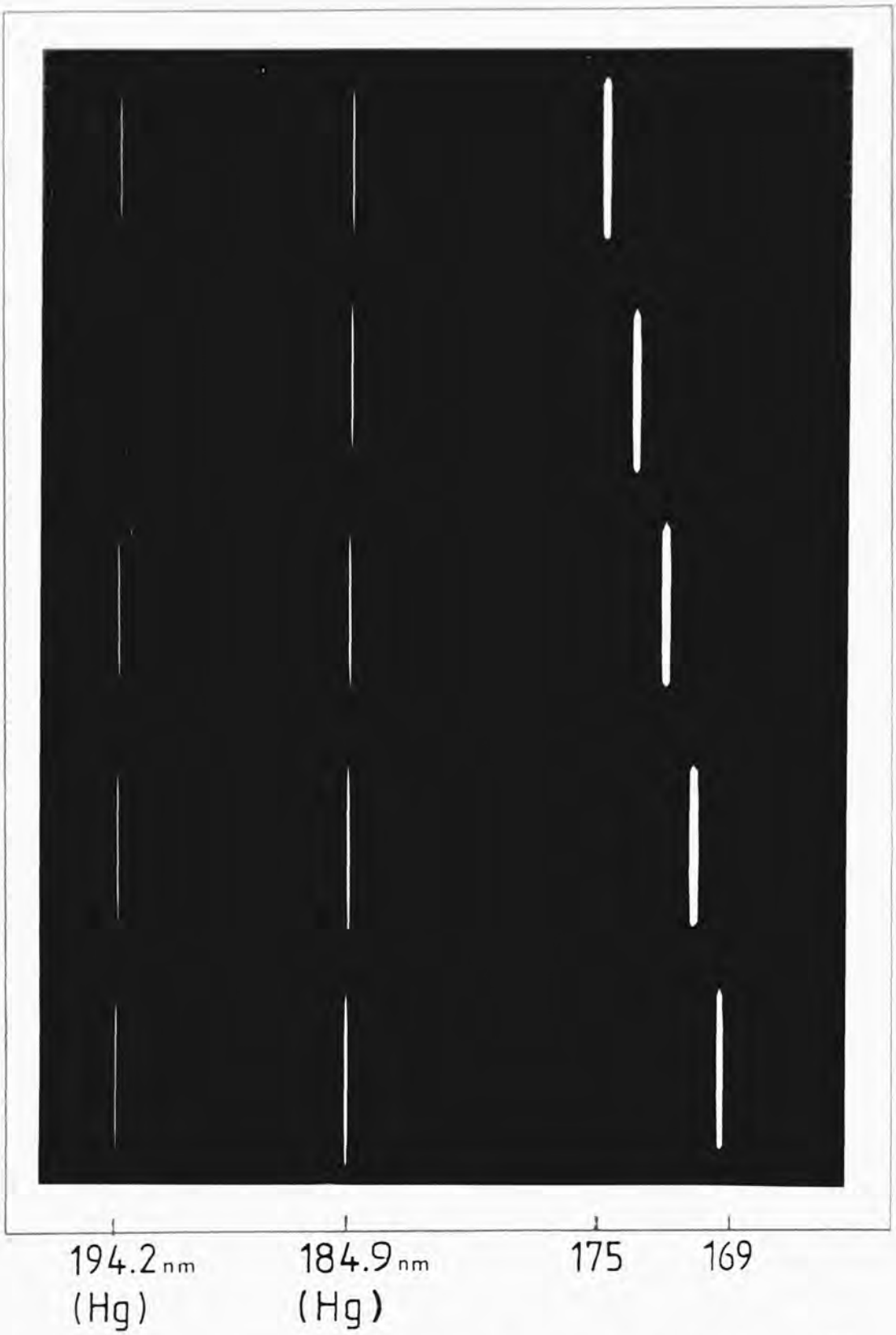


FIGURE 16(b)





Tuned Xenon laser output spectra, 169 – 175nm.

PLATE 4

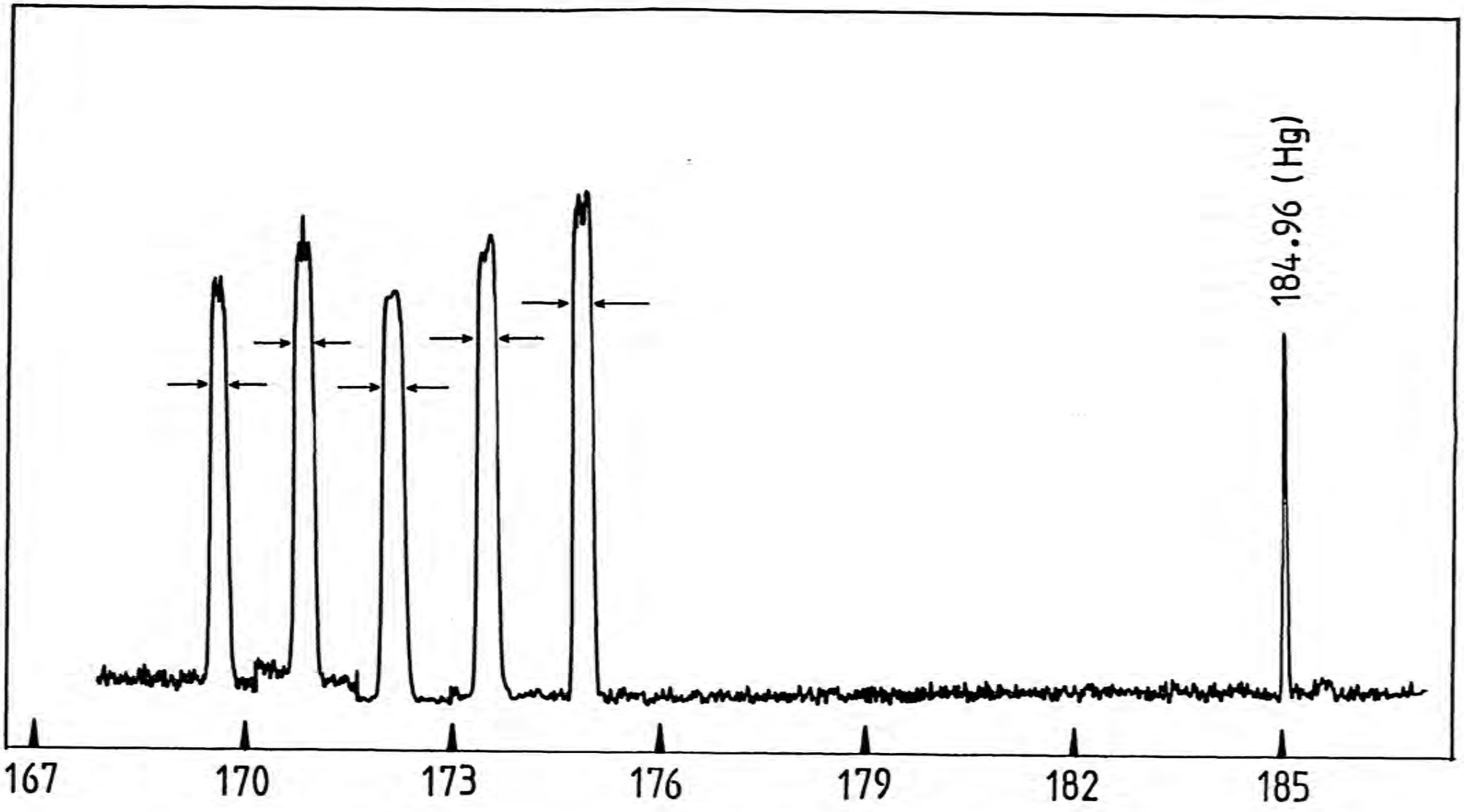


FIGURE 17

2.9.4 The introduction of an aperture in the cavity

In an attempt to reduce the bandwidth of the tuned xenon laser, the effects of the introduction of a circular aperture in the cavity, were examined. Using a 6 mm diameter anode tube, a circular aperture of 3 mm diameter was introduced in the cavity, between the anode tube and the prism tuning element.

The reflectivity of the output coupler had to be increased to 48% in order to obtain a tuned output energy of 1 mJ. This corresponded to a spectral bandwidth of 0.1 nm. Thus the introduction of the aperture caused the spectral brightness to decrease by a factor of three. When the aperture was removed and the electron beam energy deposited in the gas was reduced so that the tuned energy output was only 1 mJ, the spectral bandwidth also decreased to 0.1 nm. This indicated that the effect of the 3 mm diameter aperture on the tuned laser bandwidth was negligible.

2.9.5 Tuning using a BaF_2 prism

Extrapolation from published data[62,63,64] suggests that the dispersion of BaF_2 at 170 nm is approximately three times the dispersion of spectrasil at the same wavelength. The refractive index of BaF_2 was measured at 172 nm (section 3.6) and was found to be approximately equal to the refractive index of spectrasil[61]. Finally the transmission of the two materials is comparable around 172 nm[62].

Due to the higher dispersion of BaF_2 around 170 nm, it was decided to investigate the spectral bandwidth of the tuned laser output when a BaF_2 prism was incorporated in the tuning element.

BaF_2 is only available[65] in cylindrical boules of 0.5 inch diameter. A 60 degree prism was constructed by cutting such a boule, so that the two refractive surfaces of the prism were ellipses of 0.5 inch minor axis and 0.577 inch major axis.

When the BaF_2 prism was introduced in the cavity lasing was obtained, and two observations were noted:

a) The angle by which the BaF_2 prism-tuning element had to be turned from the position where the He-Ne laser wavelength (632.8 nm) was resonating to the position where the 171.8 nm wavelength was resonating, was 14.9% smaller than the corresponding angle when the spectrasil prism was used. This indicated that the difference in the values of the refractive index of BaF_2 at 171.8 and 632.8 nm, is smaller than the corresponding difference in the values of the refractive index of spectrasil.

b) With the BaF_2 prism in the cavity, the resonant wavelength change when the tuning micrometer was shifted by one division around 171.8 nm, was 0.13 nm. With the spectrasil prism in the cavity, the same shift in the micrometer reading caused the resonant wavelength to change by 0.11 nm. This implied that the dispersion of BaF_2 around 171.8 nm was smaller than the dispersion of spectrasil at the same wavelength. This conclusion contradicts predictions of the formula derived by Malitson[63] to fit the experimentally measured values of the refractive index of BaF_2 down to 253.7 nm.

Examination of the spectral bandwidth of the tuned output indicated values comparable to the bandwidths obtained with the spectrasil prism. When a 6 mm diameter anode tube was used in combination with the BaF_2 prism-tuning element and a 48% output coupler, output energies up to 8 mJ were obtained around 172 nm.

Absorption losses in the tuning prism were thought to be one of the factors determining the short wavelength edge of the tuning range. However, using the BaF_2 prism, reliable tuning was obtained down to 169.5 nm. This would imply that it was the gain in the excited xenon gas that determined the tuning range of the laser rather than absorption losses in the intra-cavity elements.

2.9.6 Tuning using a two-prism tuning element

At visible wavelengths, where the dispersion of optical materials is low, combinations of several prisms are used[60,66] in order to obtain narrow output bandwidths. In this section the performance of a two-prism tuning element in tuning the xenon excimer laser is described. The problems involved in designing a multi-prism tuning element are examined.

Figure 18(a) shows the geometry of the single-prism tuning element. The Brewsters angle of spectrasil is approximately 60 degrees[61]. A second prism can thus be added on the turn-table so that one of its surfaces is parallel to one of the surfaces of the first prism, as shown in figure 18(b). The high reflectivity mirror had to be rotated by 60 degrees, the deviation caused by the second prism.

Using a two-prism tuning element, lasing was achieved using a 68% output coupler, with output energies up to 4.5 mJ. This corresponded to a spectral bandwidth of 0.13 nm. Lasing was also observed when the output coupler was replaced by a 48% reflector. The spectral profile of the tuned output using such a cavity configuration is shown in figure 19. The F.W.H.M. was only 0.07 nm, but it corresponded to an output energy of $\sim$0.8 mJ.

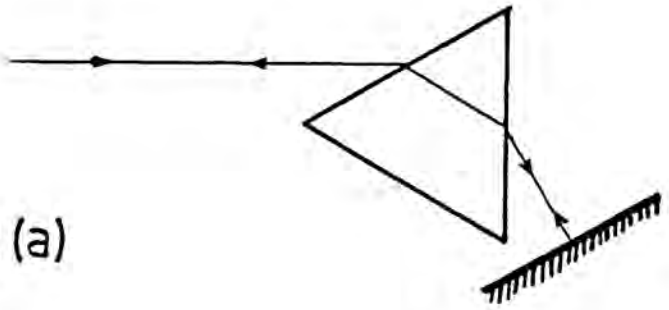
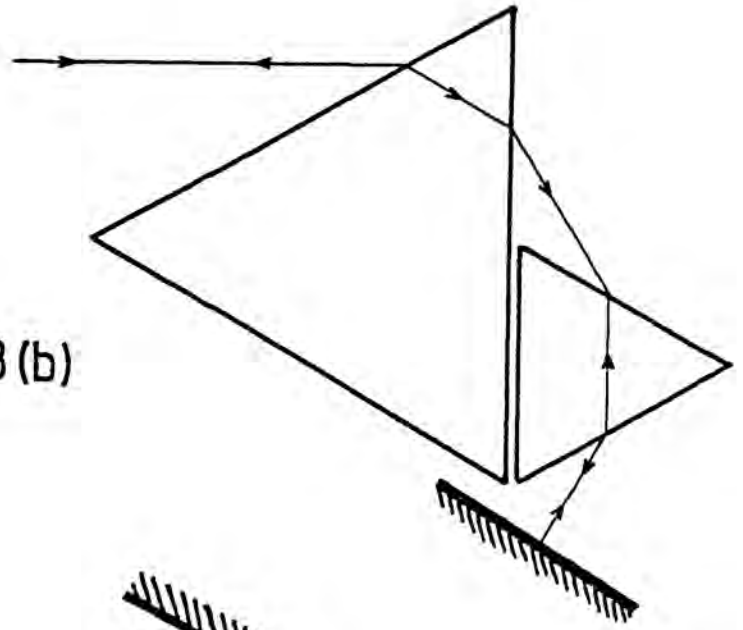
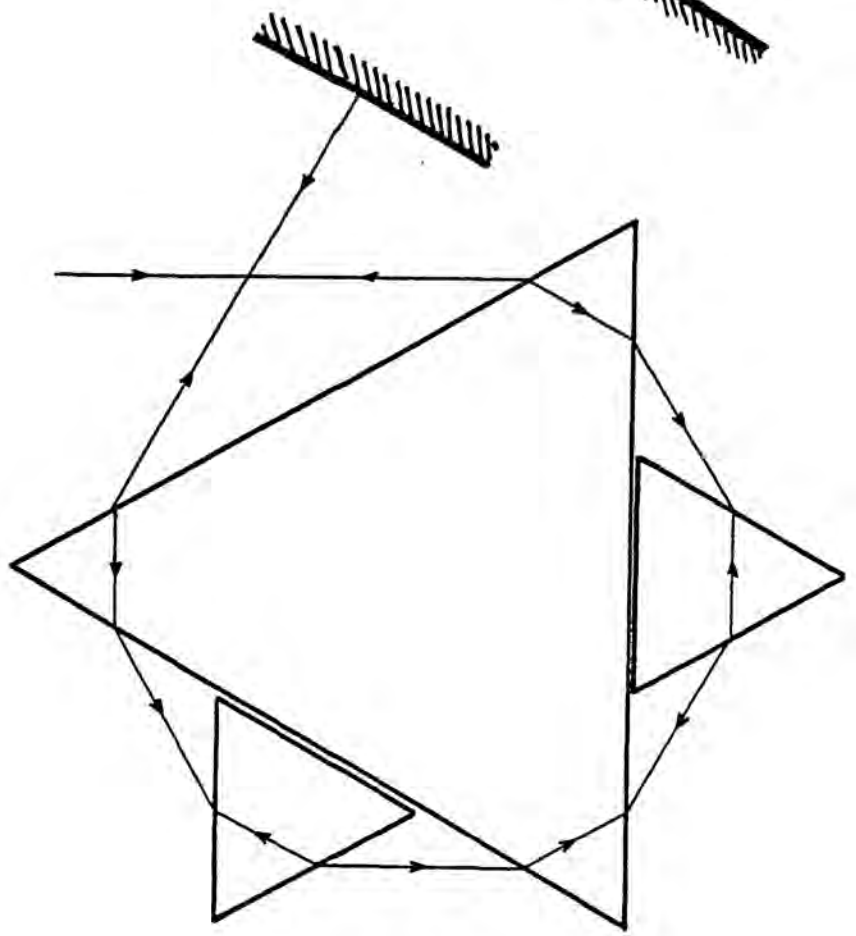


FIGURE 18 (a)



18 (b)



18 (c)

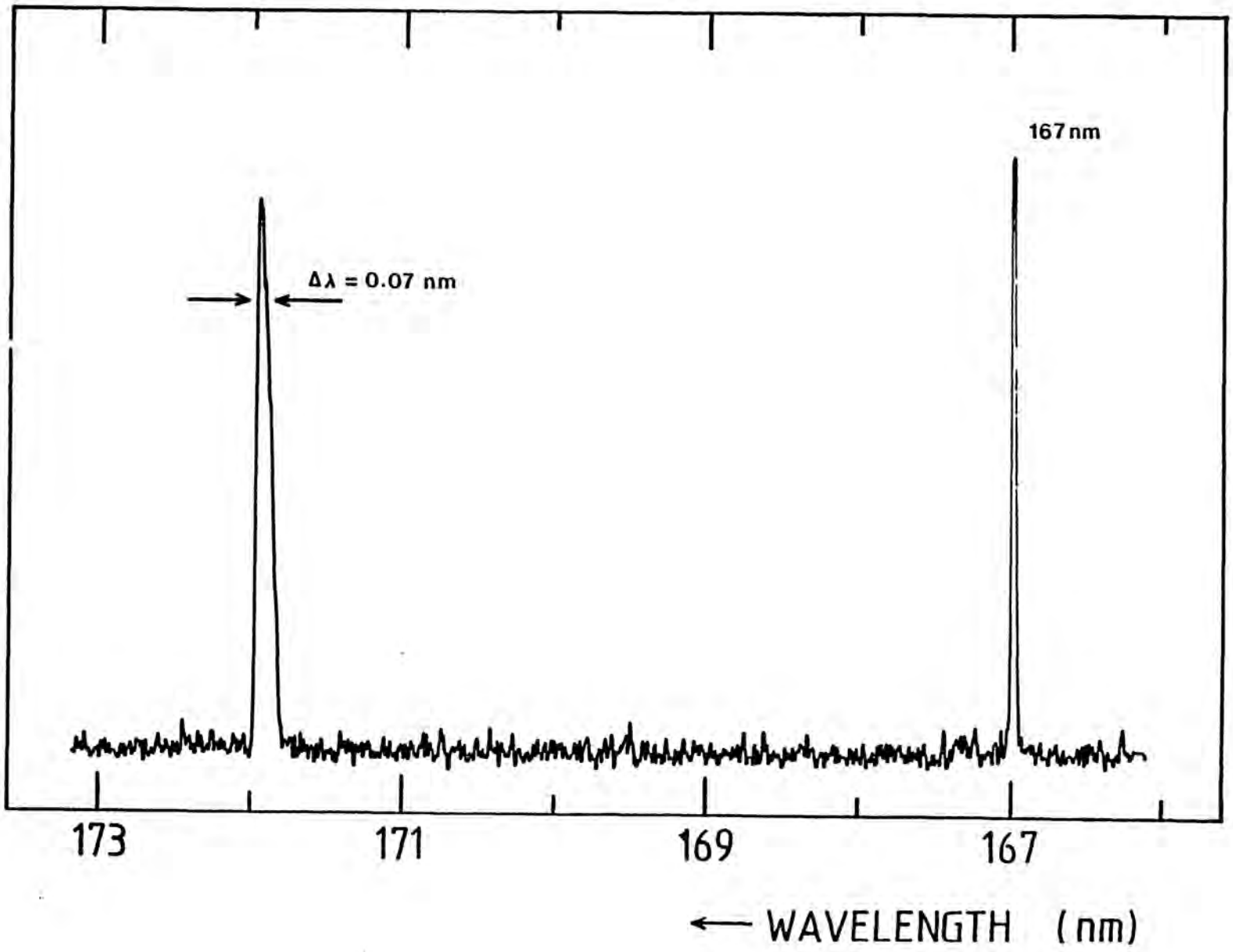


FIGURE 19

The change in the resonant wavelength of the cavity when the micrometer reading was altered by one division around 171.8 nm was only 0.0575 nm. This was only half the corresponding value (~0.11 nm/div., see section 2.9.5) for the single-prism tuning element. The addition of the second prism thus caused a x2 increase in the dispersion of the tuning element.

Due to the large difference in the values of the refractive index of spectrasil at 172 and 632.8 nm, the wavelength of the He-Ne alignment laser, the number of prisms employed was limited to two. However, efficient tuning was observed even with a 48% reflectivity output coupler, suggesting that the losses due to the two-prism tuning element at the resonant wavelength were low. Provided an alignment laser emitting in the far UV was used, a larger number of prisms could be used in the tuning element.

Figure 18(c) shows a three-prism arrangement, corresponding to a five-prism tuning element. An important advantage of a five-prism tuning element, apart from the x5 increase in the dispersion, is that the intra-cavity beam is deviated by 300 degrees. The high reflectivity mirror can thus be placed in the opposite half of the turn-table which is normally vacant.

2.9.7 Pressure tuning

Xenon gas has a pressure dependent refractive index[67,68]. The resonant wavelength of the laser cavity can therefore be varied by altering the pressure of the xenon laser gas.

Ordinarily the xenon laser is tuned by rotating a turn-table on which the prism and the high reflectivity mirror are attached[44,36]. Rotation is achieved using a micrometer to

drive a push-rod. During the tuning studies of the xenon laser some backlash was observed, which introduced an uncertainty in the value of the resonant wavelength of typically ± 0.05 nm. Pressure tuning was investigated as a possible alternative method of tuning.

The orientation of the tuning element was kept fixed with respect to the laser axis, while the xenon pressure in the cavity was varied. A plot of the variation of the peak wavelength output with pressure indicated an increase of the output wavelength of 0.68 nm per atmosphere reduction of pressure around 12 bar of xenon.

Pressure tuning was shown to be a reliable way of tuning the xenon laser. No backlash was observed. There was a serious draw-back, however. Energy deposition of the electron beam in the gas is only uniform over a limited range of xenon pressures. Lasing outside this pressure range can be obtained, but the beam quality of the output is poor. Pressure tuning is therefore only effective over a limited range of wavelengths ($\leqslant 2$ nm) for a particular setting of the micrometer.

Pressure tuning was found to involve frequent freezing of the xenon gas into the storage cylinder, in order to reduce the pressure in the cavity, and allowing it to boil, in order to increase the pressure. These processes were slow. Furthermore, extra care had to be taken to prevent the contamination of the gas by impurities that are normally stored in the cylinder (see section 2.8).

2.9.8 Comparison of the performance of different tuning elements

It was shown in this section that prisms and diffraction gratings are capable of tuning the xenon excimer laser, reliably.

However, their performance indicated that a prism can provide a higher reflectivity at the resonance wavelength than a grating of identical resonance curve (quality factor versus wavelength). This was expected, since diffraction gratings are known to channel the incident energy into more than one diffraction order. Even gratings that are designed to have a preferential distribution of the diffracted energy suffer, because some radiation is absorbed by the reflective coating and some is scattered into areas other than the desired order. Holographic gratings appear very promising[69] since their scattered energy is known to be two orders of magnitude lower than ruled gratings.

Bandwidths of 0.25 nm were observed using a spectrasil or a BaF_2 prism. Similar bandwidths have also been observed using a diffraction grating, but with a very disappointing energy output (~1 mJ). For comparable tuned energy outputs, bandwidths of less than 0.1 nm were obtained using a two-prism tuning element. The use of a more dispersive grating could reduce the output bandwidth even further, but higher gain values are required to overcome the extra losses introduced by the new grating.

Optical damage to prisms was found to be a surface effect, which could be remedied by repolishing. Optical damage to a diffraction grating involved the removal of the reflective coating and could be remedied by depositing a new reflective coating.

Prisms were found more convenient to maintain in working order.

CHAPTER 3

MEASUREMENT OF THE PHOTOIONIZATION CROSS SECTION OF Se(^{1}S) IN THE RANGE 170-175 NM

3.1 Introduction to group VIA lasers

Lasers have the capability to concentrate energy in space and time. They are thus able to transfer large energies to small volumes in a sub-nanosecond time-scale. This unique property allows lasers to be used in order to attain the conditions of very high density and temperature at which thermonuclear fussion can occur[70]. The technology that will allow the construction of a single laser oscillator which is able to generate high energy short pulses is not available however, so high power laser systems consist of a low power oscillator followed by a chain of amplifiers.

Consider a single amplifier. Energy is supplied externally so that a population inversion is formed in the amplifier medium. However, spontaneous emission and quenching processes of the upper state limit the length of time for which population inversion can be maintained. A laser amplifier is only efficient when the time required to establish the inversion in the amplifier medium is considerably shorter than the effective lifetime of the upper state. The electrical energy used to pump the amplifier can, at best, be supplied to the gain medium in 10^{-6} seconds. An efficient amplifier thus requires a lasing transition with an effective upper state lifetime which is longer than 1 ns.

In a high energy storage amplifier, the amplification of

the spontaneous emission and the production of parasitic oscillations due to the presence of stray reflections can reduce the effective radiative lifetime of the upper state. These losses can be reduced by employing a laser transition with low stimulated emission cross section and long spontaneous emission lifetime. However, efficient energy extraction from an amplifier is only achieved when the radiation flux to be amplified exceeds the saturation flux, E_s, of the laser transition, given by $E_s = h\nu/\sigma$ where $h\nu$ is the photon energy and σ is the stimulated emission cross section. Damage to optical components limits the laser flux to a few Joules cm^{-2}. This condition sets a lower limit to the stimulated emission cross section for efficient amplification.

A compromise value of $\sigma \sim 10^{-20}$ cm^2 appears low enough so that superfluorescence and parasitic oscillations are substantially reduced, but at the same time large enough so that saturation and efficient extraction can be achieved without damaging the optics.

Transitions characterized by values of $\sigma = 10^{-20}$ cm^2 can be found in group VIA elements (O,S,Se and Te) where the Pauli exclusion principle prevents the rearrangement of the electrons in the partially filled p-shell. Electric dipole transitions are therefore excluded. Figure 20 shows the electronic levels of the selenium atom. States $^1S_0$ and $^1D_2$ are radiatively metastable. The $Se(^1S_0)$ state is found to be highly resistant to collisional deactivation whereas $Se(^1D_2)$ can be rapidly quenched to $Se(^3P)$. Provided a way of populating $Se(^1S_0)$ can be found, population inversion can be maintained between the $^1S_0$ and $^1D_2$ states. Furthermore the $Se(^3P_1)$ state lies 2000 cm^{-1} above $Se(^3P_2)$, the ground state of selenium. Thermal population

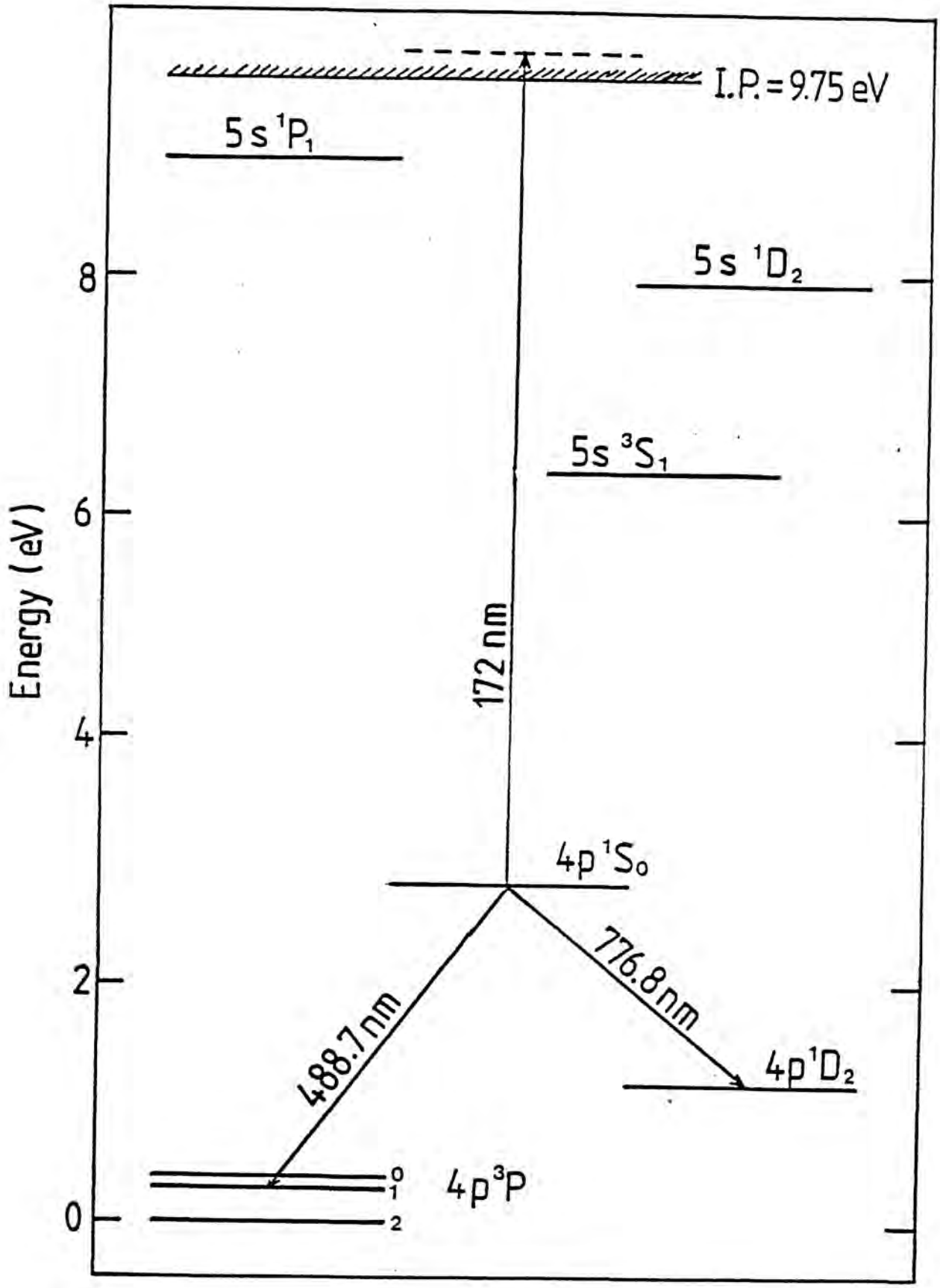


FIGURE 20

Energy level diagram of atomic Selenium

of $^3P_1$ is unlikely whereas collisional deactivation of the same state can maintain a population inversion between the states $Se(^1S_0)$ and $Se(^3P_1)$.

The developement of large scale group VIA amplifiers requires a demonstrated method of efficiently generating high $Se(^1S_0)$ atom densities ($\sim 10^{16}$ cm^{-3}).

3.2 The production of $Se(^1S_0)$ by photodissociation

Electron beam excitation can be used to produce $Se(^1S_0)$ but efficient coupling of the electron beam into the medium requires high pressures. However the collisions that are likely to take place at high pressures are known[71] to change the characteristics of the auroral ($^1S_0 \rightarrow {}^1D_2$) and transauroral ($^1S_0 \rightarrow {}^3P_1$) transitions. Furthermore electrons are known to quench the $^1S_0$ state, making electrical excitation inadequate.

When a molecule absorbs a photon, a molecular transition will occur. By choosing the right molecule and a suitably energetic photon, the photodissociation of the molecule can be accomplished and the desired photodissociation products can be produced with high quantum yields.

The carbonyl selenide (OCSe) is interesting because it is basically a carbon monoxide molecule with a selenium atom weakly bound to it. Photodissociation of OCSe by a photon of relatively low energy ($\leq$11 eV) is expected to produce a Se atom and a CO molecule. This is due to the large dissociation energy of CO (11 eV)[5] which is one of the most stable molecules in nature, compared with the possible binding energy of CSe or OSe molecules.

The absorption spectrum of OCSe has been measured[72] in the 110-200 nm region. This is reproduced in figure 21.

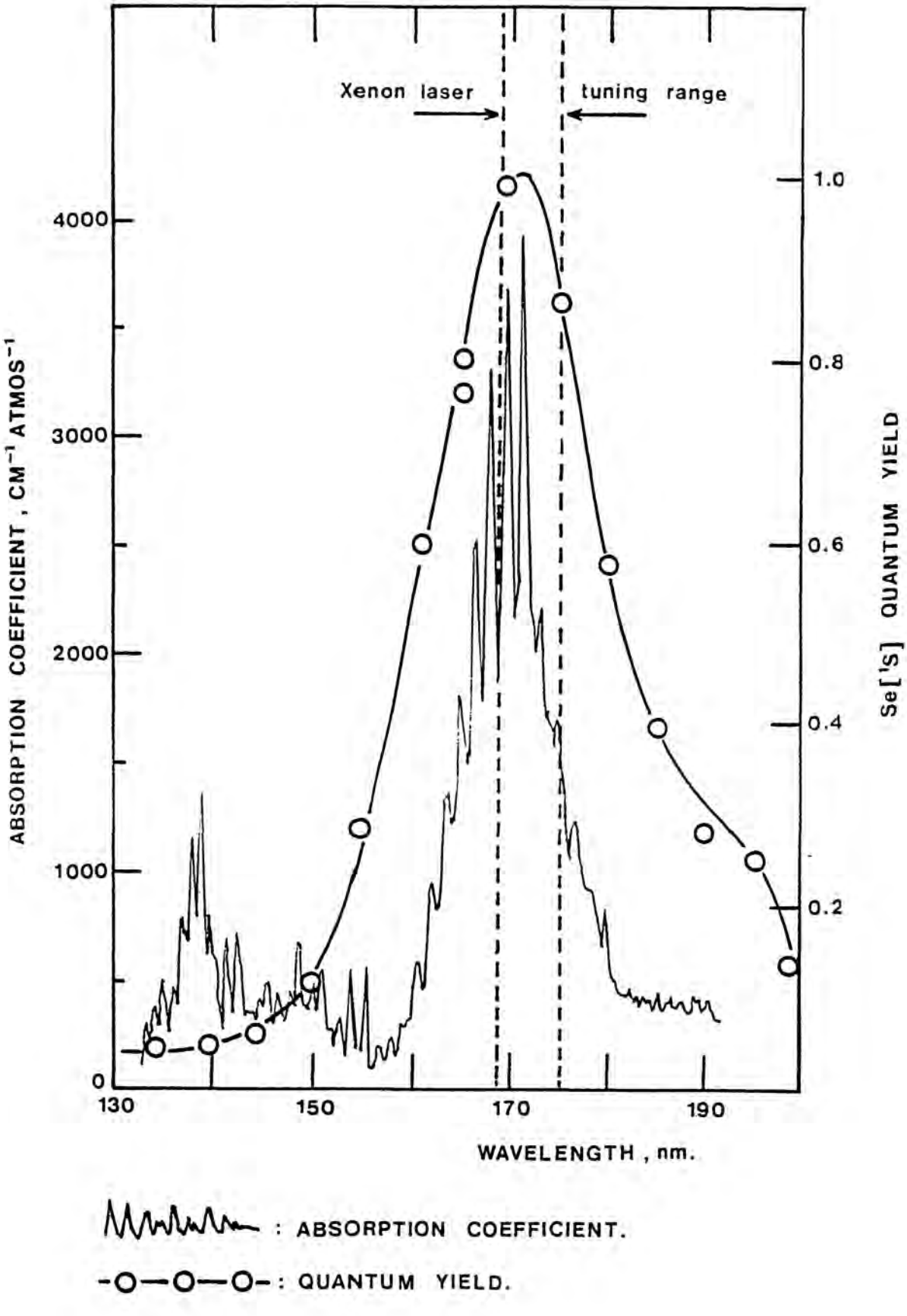

Xenon laser
tuning range
ABSORPTION COEFFICIENT , CM^{-1} ATMOS^{-1}
Se[^{1}S] QUANTUM YIELD
WAVELENGTH , nm.
0
1000
2000
3000
4000
130
150
170
190
0.2
0.4
0.6
0.8
1.0
: ABSORPTION COEFFICIENT.
: QUANTUM YIELD.

FIGURE 21

A strong absorption feature is seen around 170 nm. This is found to coincide with a region of near unit quantum yield for the production of $Se(^1S_0)$ in the photodissociation of OCSe, as measured by Black[72]. Black's estimates of the quantum yield as a function of wavelength are also reproduced in figure 21. These are found to be in agreement with indepedent measurements by Shaw[73]. For comparison, the xenon laser tuning range is also indicated in figure 21 and it is clear that it coincides with the region of maximum absorption by OCSe and the near unit quantum yield of $Se(^1S_0)$. Xenon excimer emission, therefore appears to be the ideal pumping source for the $^1S_0$ state production from the photodissociation of OCSe.

The absorption spectrum of OCSe in the region 160-180 nm shows considerable diffuse structure (see figure 21). This appears to contradict the hypothesis that photodissociation gives rise to a continuous absorption spectrum. It was shown by Pack[74], however that such diffuse vibrational structure superimposed on a continuum as exhibited by OCSe around 170 nm can also give rise to a transition that terminates to a dissociative upper state. This in turn can explain the high quantum yield of $Se(^1S_0)$ due to the photodissociation of OCSe around 170 nm.

The low energy electronic states of OCSe are drawn in figure 22 , based on the experimental work of Finn[75]. The three lower dissociation limits give rise to the three lowest states of the selenium atom and ground state CO molecule. Absorption of a 172 nm photon ($E = 58000\ cm^{-1}$) by a ground state OCSe molecule will populate the $OCSe(^1\Sigma^+)$ which is highly dissociative giving rise to the $Se(^1S_0)$ state. This in turn can decay to $^1D_2$ or $^3P_1$ giving rise to the selenium

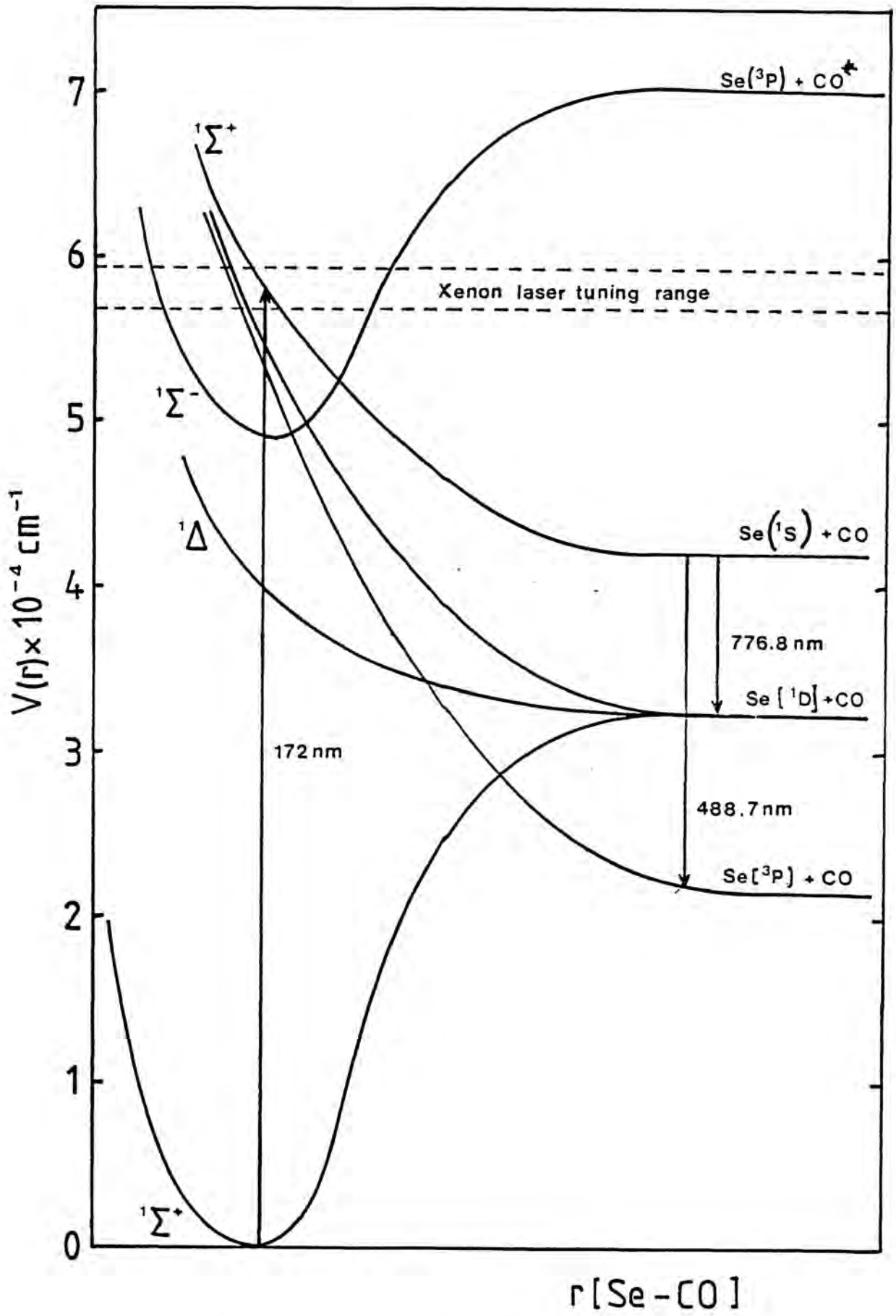

Se(³P) + CO*
¹Σ⁺
Xenon laser tuning range
¹Σ⁻
¹Δ
Se(¹S) + CO
776.8 nm
Se [¹D] + CO
172 nm
488.7 nm
Se[³P] + CO
¹Σ⁺
V(r) x 10⁻⁴ cm⁻¹
r[Se-CO]
0
1
2
3
4
5
6
7

FIGURE 22

auroral (776.8 nm) and transauroral (488.7 nm) emissions respectively. Weak oscillation on both these transitions has been reported by Powell[76] using xenon superfluorescence to photodissociate OCSe. Laser action has also been reported[77] on the sulphur $^1S_0 \rightarrow {}^1D_2$ transition. The sulphur $^1S_0$ state can also be produced with near unit quantum yield by the photolysis of OCS molecule using krypton excimer radiation at 146 nm[78].

3.3 The Se(^{1}S) loss mechanisms

The energy stored in the upper state Se(^{1}S) can be reduced by a number of mechanisms:

a) The quenching by the parent triatomic molecule:

$$Se(^1S) + OCSe \longrightarrow Se_2^* + CO \qquad (3.1)$$

b) Induced emission due to a collision with a buffer gas particle M:

$$Se(^1S) + M \longrightarrow Se(^3P,\ ^1D) + M + h\nu \qquad (3.2)$$

c) Photoionization of the excited state by the photolysis radiation:

$$Se(^1S) + h\nu(172\ nm) \longrightarrow Se^+ + e^- \qquad (3.3)$$

The effects of the quenching reaction 3.1 can be reduced by photolysis of all OCSe molecules present in the dissociation chamber. This requires a photolysis radiation flux E_p which is high enough in order to bleach the absorption of OCSe, i.e. $E_p > h\nu/\sigma_d$ where σ_d is the photodissociation cross section of OCSe at 172 nm. The saturation flux is estimated at 12 mJ cm^{-2}. Such a flux can easily be obtained from the xenon excimer laser which can provide an energy flux exceeding 100 mJ cm^{-2}.

Experimental evidence[79] indicates that the collisional

deactivation of a $Se(^1S)$ state by a ground state rare gas atom (eq. 3.2) occurs entirely via a radiative transition. The molecular state formed by the $Se(^1S)$ and a ground state rare gas atom is repulsive (compare with $XeO(2^1\Sigma^+)$ state shown in figure 11) and it does not cross any other molecular curves at thermally accessible points. The $Se(^1S)$ state can therefore be considered resistant to collisional deactivation. Note that the molecular state formed by $O(^1D)$ and a xenon atom is bound and it crosses repelling molecular states that dissociate to ground state atomic oxygen. Efficient collisional deactivation of $O(^1D)$ and $Se(^1D)$ is therefore to be expected.

The photon energy required for the photodissociation of OCSe is high enough to photoionize the $Se(^1S)$ state according to equation 3.3 . Photoelectrons generated by this process have an energy of 0.2 eV. Quenching of $Se(^1S)$ by these slow electrons can be significant[80]. Furthermore photoelectrons can increase their energy by superelastic collisions with $Se(^1S)$. The electron temperature can rise rapidly and additional electrons can be generated due to electron impact ionization of the medium, thus decreasing the overall laser efficiency. Knowledge of the photodissociation cross section, σ_d of OCSe and the photoionization cross section, σ_i of $Se(^1S)$ are required for the accurate kinetic modelling of the system.

The purpose of this experiment was to measure the photoionization cross section of $Se(^1S)$ in the range 170 to 175 nm using the xenon excimer laser described in chapter 2.

3.4 Theoretical background

Consider a laser pulse of intensity $I(x,t)$ entering a cell containig OCSe gas at a density $\rho_0(x)$. The leading edge of

the pulse is expected to photodissociate the OCSe thus producing $Se(^1S)$. The same pulse is expected to photoionize some of the $Se(^1S)$ produced. The density of the photoelectrons generated n_e is given by[81]:

$$\frac{n_e(x,t)}{t} = \sigma_i I(x,t)\rho^*(x,t) - L \qquad (3.4)$$

where σ_i is the photoionization cross section of $Se(^1S)$ and $\rho^*(x,t)$ is the $Se(^1S)$ number density. This may be written in terms of the initial OCSe density $\rho_0(x)$ by :

$$\rho^*(x,t) = \phi(\rho_0(x) - \rho(x,t)) \qquad (3.5)$$

where ϕ is the quantum yield for the $Se(^1S)$ production from the photolysis of OCSe and $\rho(x,t)$ is the time varying OCSe density. The term L represents the electron loss rate mainly due to electron-ion recombination. However the recombination rate is sufficiently slow compared with the rate of production of photoelectrons[81] so that the loss term L can be ignored.

The solution to eq. 3.4 is given by[81]:

$$n_e(x) = \frac{\sigma_i \phi \rho_0}{\sigma_d}\left\{\ln\left[\frac{V}{\exp(\sigma_d \rho_0 x)}\right] + \frac{(1-\exp(\sigma_d E))}{V}\right\} \qquad (3.6)$$

where $V = \exp(\sigma_d E) + \exp(\sigma_d \rho_0 x) + 1 \qquad (3.7)$

and E is the laser photon density.

It was mentioned in section 3.3 that superelastic collisions of photoelectrons with $Se(^1S)$ can heat the electrons. In order to prevent this avalanching process a molecular buffer gas such as nitrogen can be used to collisionally cool the electrons. More important, by keeping the number densities of photoelectrons and of $Se(^1S)$ sufficiently low the effects of these collisions can be negligible. In this experiment OCSe densities of $\rho_0 \sim 10^{15}$ cm^{-3} were used. Photon densities of E 1 to 5×10^{16}

cm^{-2} were provided by the laser. For a photodissociation cross section $\sigma_d \approx 10^{-16}$ cm^2 and x = 1 cm then $\sigma_d \rho_0 x \approx 10^{-10}$ and therefore $\exp(\sigma_d \rho_0 x) = 1$. Equation 3.7 then becomes:

$$V = \exp(\sigma_d E) \tag{3.8}$$

Substituting $n_e = N_e A^{-1} L^{-1}$ in eq. 3.6 where N_e is the total number of electrons generated in the collection length L and A is the area of the input laser beam:

$$N_e = \frac{\sigma_i \Phi \rho_0 AL}{\sigma_d} (\ln V + V^{-1} - 1) \tag{3.9}$$

Note that for high photon densities i.e. $E \geqslant 5 \times 10^{16}$ cm^{-2} then $V^{-1} \ll 1$ and can be neglected. Equation 3.9 becomes:

$$N_e = \frac{\sigma_i \Phi \rho_0 AL}{\sigma_d} (\ln V - 1) \tag{3.10}$$

Equation 3.10 implies that for a constant photon flux, a plot of the number of electrons collected N_e for different initial number densities ρ_0 will be a straight line whose slope will be given by:

$$\text{slope} = \frac{\sigma_i \Phi AL}{\sigma_d} (\ln V - 1) \tag{3.11}$$

Furthermore for a constant number density ρ_0 of OCSe, the plot of the number of electrons generated N_e for different photon densities E should be a curve that tends asymptotically, for large values of E, to a straight line of slope $\sigma_i \Phi \rho_0 AL$. Note that the intercept of this line on the N_e axis will be:

$$\text{intercept} = - \frac{\sigma_i \Phi \rho_0 AL}{\sigma_d} \tag{3.12}$$

where as its intercept on the E-axis will be given by σ_d^{-1}.

3.5 The experimental apparatus

The apparatus used in this measurement consisted of a simple charge detector able to collect and count the electrons or ions produced by the photoionization of $Se(^1S)$. The detector was housed in the photoionization chamber which was constructed entirely out of Vacuum Generators stainless steel ultra-high vacuum fittings. A schematic diagram of the gas handling arrangement is shown in figure 23. Stainless steel was used where possible since other metals are chemically attacked by the OCSe[82]. Joints were welded where possible to reduce the possibility of any leaks being present. Where welding was inappropriate, stainless steel compression fittings were used. All taps used were of packless bellows design. The photoionization chamber windows were sealed using viton O-rings. A 6 inch oil diffusion pump, backed by a rotary pump, with additional pumping for condensibles provided by a liquid nitrogen cooled cold trap, could evacuate the system to pressures less than 10^{-6} mbar.

A schematic diagram of the photoionization detector is shown in figure 24 . It consisted of three collinear cylindrical electrodes of 12 mm internal diameter. Dimensions were kept small to reduce path lengths and the possibility of electron-ion recombination. The central electrode collected charge over a well defined length L. The outer electrodes were separated from the collector electrode by 0.25 mm thick mylar spacers. The purpose of the two outer electrodes was to provide a uniform electric field inside the central electrode and to serve as earthed quard rings so that the length of the central electrode is better defined. A 0.7 mm thick stainless steel wire slightly displaced from the collector axis carried a small

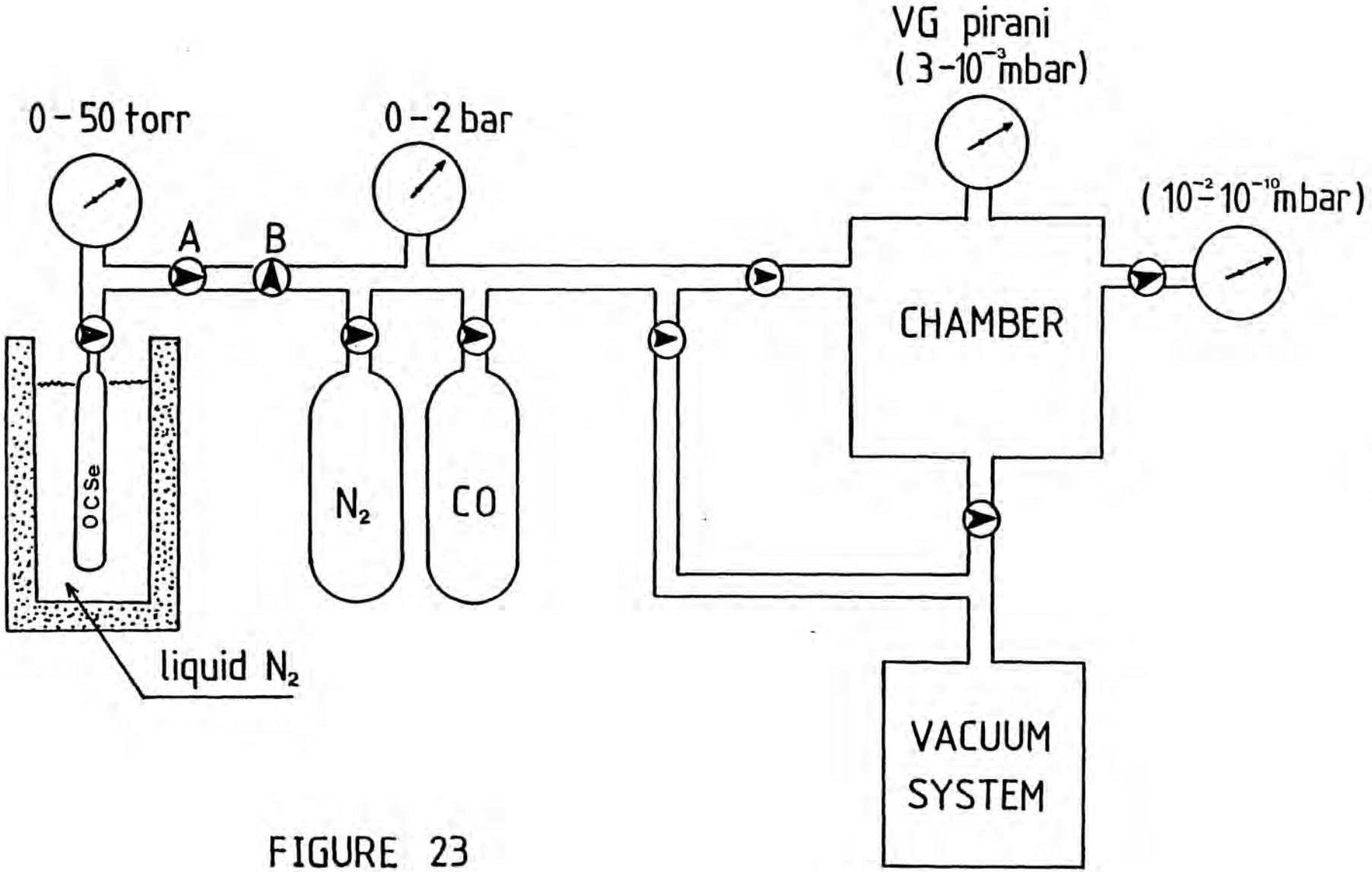

VG pirani
(3-10⁻³mbar)
0-50 torr
0-2 bar
(10⁻²-10⁻¹⁰mbar)
A
B
CHAMBER
OCSe
N₂
CO
liquid N₂
VACUUM
SYSTEM

FIGURE 23

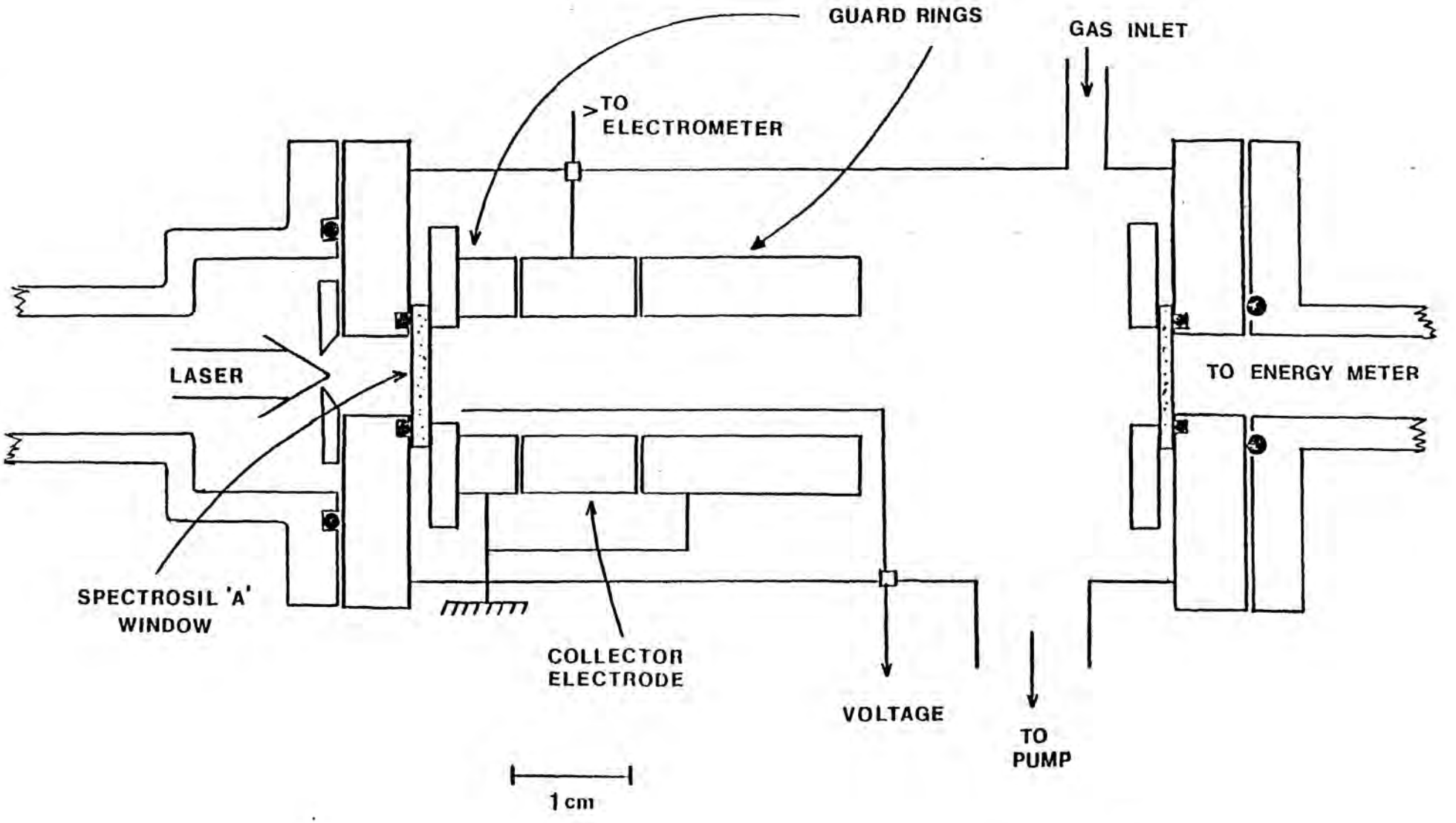

GUARD RINGS
GAS INLET
TO ELECTROMETER
LASER
TO ENERGY METER
SPECTROSIL 'A' WINDOW
COLLECTOR ELECTRODE
VOLTAGE
TO PUMP
1 cm

FIGURE 24

voltage (up to ±400 V) which was sufficient to ensure that the device operated on the plateau of the charge collected versus repelling voltage curve.

The central electrode was connected to an electrometer (Keithley type 601) so that the time integrated charge that was collected by the central electrode was directly measured. The calibration of the electrometer was checked by collecting the charge leakage through a 500 MΩ resistor over a certain period of time, when a 1.5 V battery was connected across the resistor. Using different collection periods, the different electrometer ranges were checked. The values read by the electrometer were found to be within 2% of the time integrated charge that leaked through the 500 MΩ resistor. The temporal profile of the collection of charge was displayed on a fast oscilloscope (Tektronix type 7904).

VUV radiation from the xenon laser described in chapter 2 was lead through an evacuated passage line (pressure $<10^{-1}$ mb) into the photoionization chamber. Absolute measurement of the photoionization cross section of Se(^{1}S) required accurate knowledge of the spatial profile of the laser beam. Using the 6 mm diameter anode tube, the beam diameter was measured (see chapter 4) to be 6 mm(±0.5) at a distance of 1.2 m from the laser. A 3 mm diameter aperature, placed in front of the entrance window, ensured nearly uniform illumination over a 0.07 cm^2 area of the photoionization chamber. Laser radiation was admitted to the chamber via a thin (2 mm) spectrasil window. A similar window placed at the far end of the chamber allowed the 172 nm radiation to escape. This reduced the background signal caused by the generation of photoelectrons from the scattered light within the chamber to a typical value

of a few per cent of the actual signal that was observed when OCSe was present in the chamber. Furthermore, the use of a second window allowed the laser radiation escaping from the chamber to be measured directly using an energy meter (Laser Instrumentation type 142 LR) mounted on the laser axis at the back of the chamber, provided the transmission of the spectrasil window was taken into account.

The temporal profile of the laser was monitored using a CsTe solar blind photodiode (ITT, type F4115). When the laser was used in the untuned mode, the photodiode was placed so as to monitor the radiation passing through the 97% mirror. The 172 nm signal transmitted through the 97% mirror required severe attenuation to prevent the saturation of the photodiode. When the laser was operated in a tuned mode, a 1 mm thick MgF_2 beam splitter was used to direct part (approximately 10%) of the laser output on the photodiode which was placed at right angles to the laser axis. With the photoionization chamber evacuated, calibration between the photodiode and the energy meter signals was frequently performed.

The carbonyl selenide used was manufactured by M.J. Shaw of the Rutherford laboratory by the action of dry CO on heated selenium metal[83]. Trap to trap distillation ensured its purity. The dissociation energy of OCSe is 2.1 eV. Absorption of a visible or UV photon causes the molecule to dissociate, thus making it highly unstable. The OCSe was therefore stored as a solid at liquid nitrogen temperature and under darkness to prevent its decomposition. The major impurity was expected to be CO. Before every introduction of OCSe in the photoionization chamber, the OCSe storage cylinder was opened to the vacuum system and pumping against the frozen OCSe was allowed for

periods of up to 5 minutes. Frequent cleaning of the OCSe in acetone slush ensured the removal of all the CO impurity from the storage cylinder.

A pirani gauge (V.G. type PIR 1A) attached on the chamber was able to measure pressures in the region of 3 to 10^{-3} mbar. However calibration of the pirani was done by the manufacturers using molecular nitrogen and no correction factor was available for the measurement of OCSe pressures. Pressurising the small volume between the taps A and B (see figure 23), to pressures up to 50 Torr (measured on a BOC type 50 Capsulon gauge) firstly with N_2 and then with OCSe and expanding the gases in the much larger volume of the photoionization chamber, a calibration of the pirani gauge to read OCSe pressures was obtained over the region 5×10^{-1} to 10^{-3} mbar.

3.6 Experimental results

Initially the characteristics of the photoionization detector were determined. A fixed pressure of OCSe was introduced in the chamber. Keeping the xenon laser output constant ensured that the same number of photoelectrons were generated on every shot. The charge collected for different values of voltage applied on the repelling electrode is shown in figure 25, for positive and negative voltages. As the value of the repelling potential was increased, the charge collected tended towards a constant level, the saturation charge, corresponding to the collection of all the ions generated. At very high repelling voltages, the charge collected was expected to increase again due to the production of ions from processes that obtain their energy from the high repelling voltage. However, no such increase was observed for the values of the

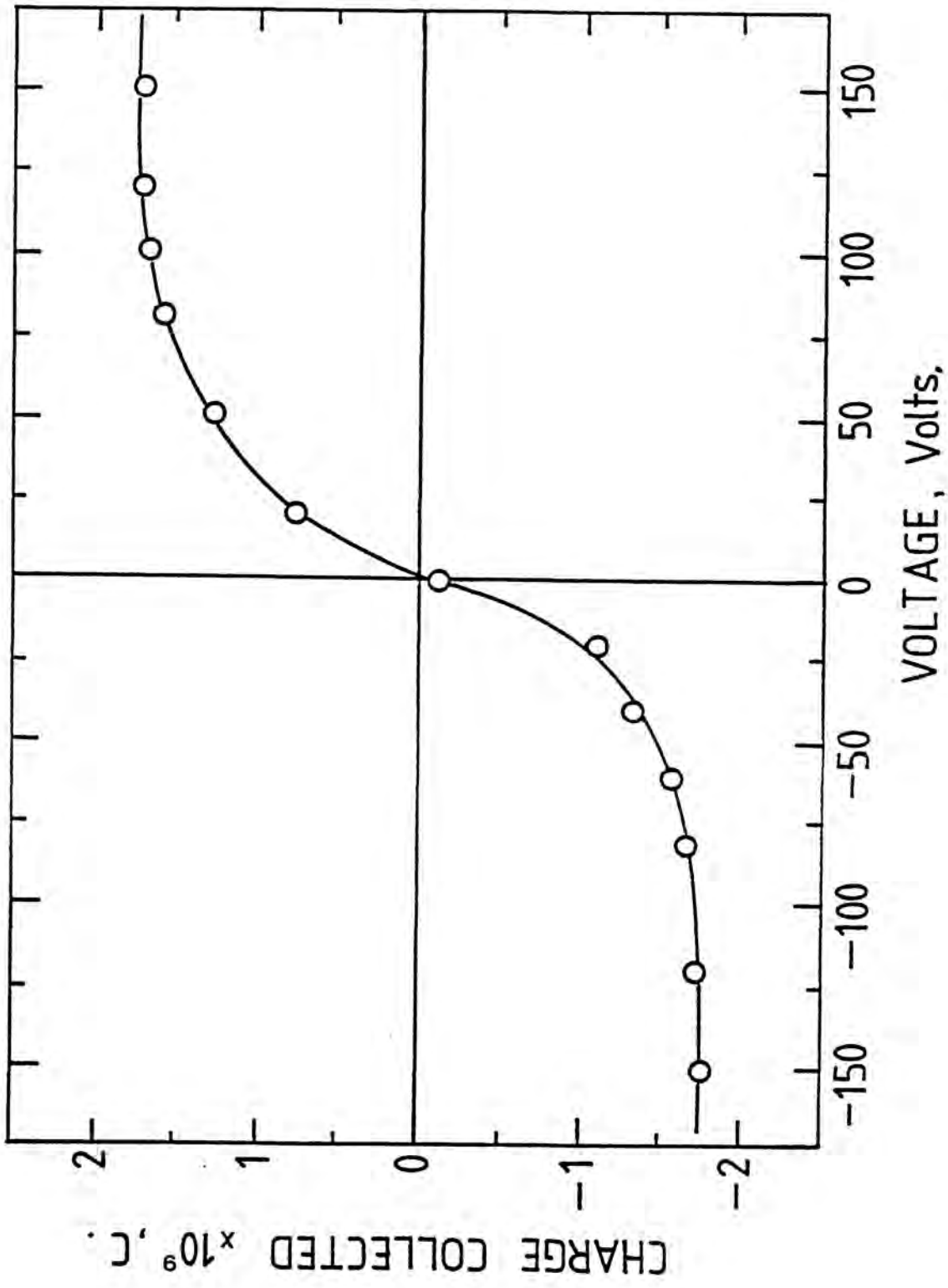

CHARGE COLLECTED x10⁹, C.
2
1
0
-1
-2
-150
-100
-50
0
50
100
150
VOLTAGE, Volts.

FIGURE 25

repelling voltage examined (-200 V to 200 V). A repelling voltage of 100 V was used in all subsequent work, thereby ensuring the complete collection of all the ions generated.

Collector electrodes of 3 mm, 5 mm and 10 mm length were used in the ionization detector. The charge collected was found to be proportional to the length of the collector electrode used. The noise signal was found to be independent of the length of the collector. A 10 mm length electrode was used in all subsequent work in order to improve the signal to noise ratio.

There have been reports of electron multiplication[80,81] due to superelastic collisions of photoelectrons with Se(^{1}S) and subsequent ionization of Se(^{1}S). In order to examine the presence of electron multiplication in the photoionization chamber, molecular nitrogen buffer gas was added up to pressures of 60 mbar. Molecular nitrogen has a large number of low lying vibrational states. When an electron collides with a nitrogen molecule its translational energy can be efficiently converted to molecular vibrational energy[84]. Nitrogen could therefore act as an energy reservoir so that the electron energy never reached a high enough value to collisionally ionize Se(^{1}S).

In figure 26 the charge collected is plotted as a function of N_2 buffer gas pressure for different repelling voltages. Collection of all the charge produced required an increase in the value of the repelling voltage. This was to be expected since the addition of N_2 produced a decrease in the mobility of the charge carriers[85] thus increasing the probability of loss of ions due to recombination. Furthermore, the length of the charge saturation plateau of the ionization detector is

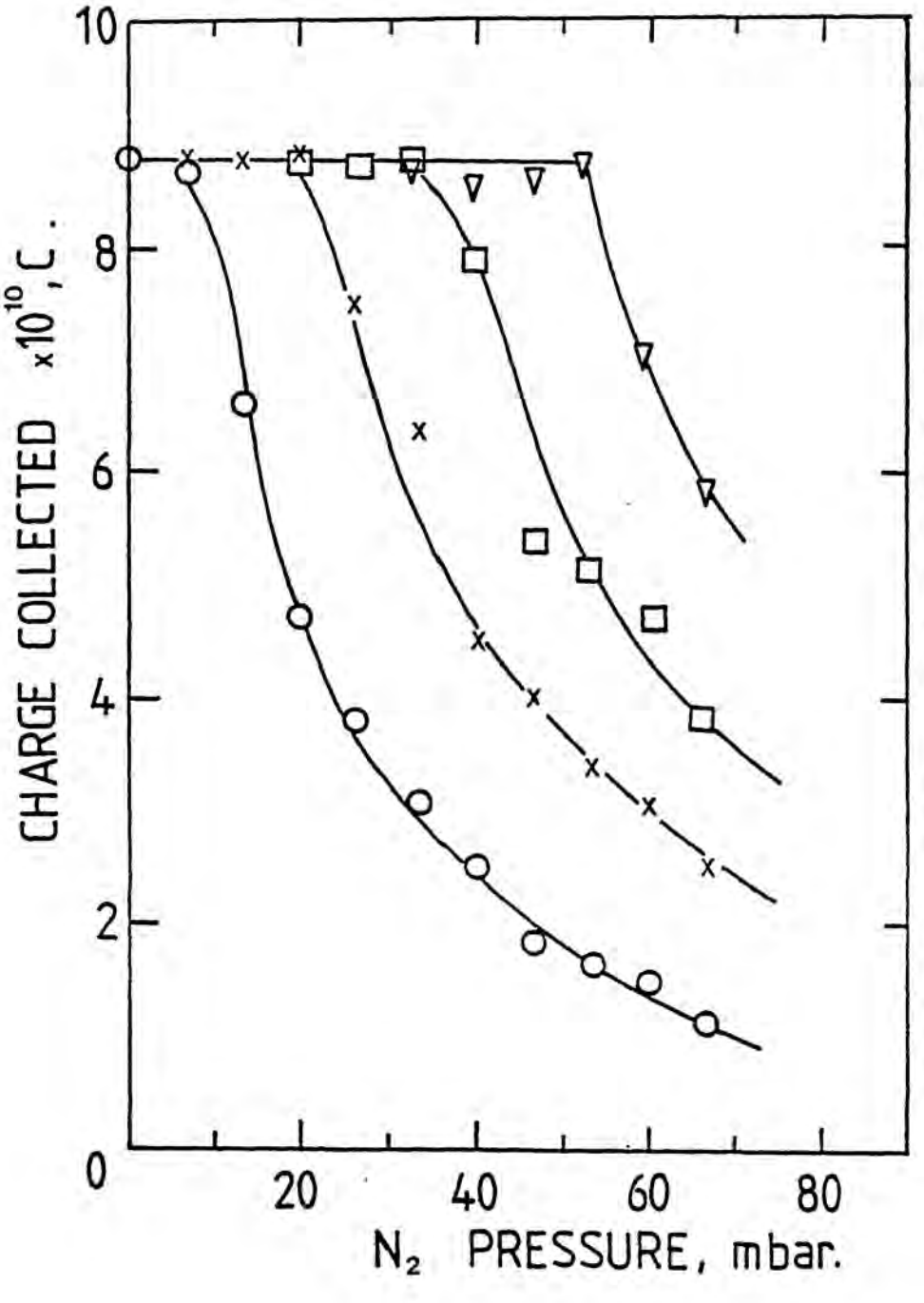

10
8
6
4
2
0
CHARGE COLLECTED x10^10, C.
20
40
60
80
N2 PRESSURE, mbar.
REPELLING POTENTIAL
100 Volts
200 Volts
300 Volts
400 Volts

FIGURE 26

known[86] to depend on the nature and pressure of the gas present in the detector. Figure 26 indicates that the charge collected is independent of the pressure of nitrogen added provided a high enough repelling voltage is applied to overcome the recombination effects caused by the lower mobility of the ions.

Open shutter photographs of the visible fluorescence produced by the photodissociation of OCSe can illustrate the effects of the presence of nitrogen on the mobility of $Se(^1S)$. The fluorescence is due the chemiluminescent quenching reaction:

$$Se(^1S) + OCSe \longrightarrow Se_2 + CO \qquad \text{followed by:}$$

$$Se_2(B^3\Sigma_u^-) \longrightarrow Se_2(X^3\Sigma_g^-) + h\nu \qquad (3.12)$$

The emission is in a broad visible band[87]. A BaF_2 lens was used to focus the xenon laser output inside the OCSe cell. Generation of $Se(^1S)$ was only over the narrow volume illuminated by the 172 nm radiation. When 0.1 mbar was only present in the cell, the thermal velocities of the excited atoms carried them outside the illuminated volume before they could be quenched by the parent molecule (see plate 5(a)). The quenching rate constant for this process is 1.6×10^{-10} cm^3 sec^{-1} (ref. 72). The quenching rate of $Se(^1S)$ by molecular nitrogen is very much smaller[87] and the quenching effects of N_2 can be neglected. However the presence of 44 mbar of N_2 in the dissociation cell prevented the movement of $Se(^1S)$ and collisionally contained the excited atoms within the volume illuminated by the 172 nm radiation (see plate 5(b)).

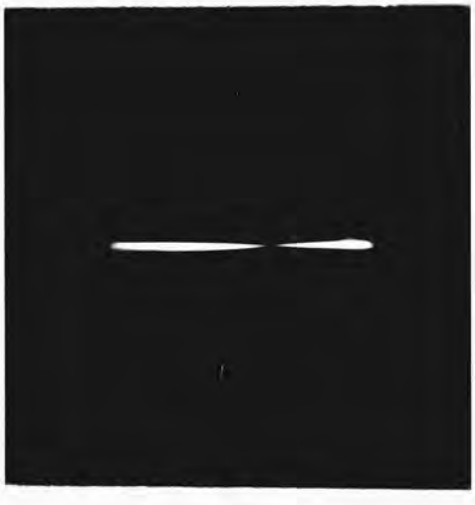
This provided a method of recording the shape of the focused beam. The focal length of the BaF_2 lens was therefore measured at 172 nm with a 2% uncertainty. The lens equation

Plate 5(a) Open shutter photograph of the visible fluorescence produced when the xenon laser output is focused in 0.1 mbar of OCSe. Background scale denotes mm.

Plate 5(b) Open shutter photograph of the visible fluorescence produced when the xenon laser output is focused in 0.1 mbar of OCSe in the presence of 44mbar of N_2.



(a)



(b)

PLATE 5

states that:

$$\frac{1}{f(\lambda_1)} = (\mu(\lambda_1) - 1)\left(\frac{1}{R_1} - \frac{1}{R_2}\right) \qquad (3.13)$$

where $f(\lambda_1)$ is the focal length at λ_1 , $\mu(\lambda_1)$ is the refractive index of the lens material at λ_1 , R_1 and R_2 are the radii of the surfaces of the lens. The focal length of the same lens was measured at 632.8 nm where values of the refractive index of BaF_2 are known[63]. A value of 1.6 $\pm$0.04 was therefore estimated for the refractive index of BaF_2 at 172 nm. This value is in good agreement with the theoretical value of 1.606 obtained from the formula published by Malitson[63].

The photon densities obtainable from the xenon laser were well above the saturation flux of the OCSe at 172 nm. Bleaching of the OCSe was thus ensured and variation of the OCSe number density, ρ_0 , implied an identical variation of the $Se(^1S)$ density produced.

Figure 27 shows the variation of the number of photoelectrons N_e collected for different OCSe number densities ρ_0 , at a constant photon density E. The graph is a straight line for values of $\rho_0 \leqslant 2 \times 10^{15}$ cm^{-3}, in agreement with equation 3.10. However the linearity fails for values of $\rho_0 > 2 \times 10^{15}$ cm^{-3}. At high OCSe number densities the energy required to bleach the OCSe molecules is expected to become a serious loss mechanism for the photon density of the laser pulse. A decrease in the photon density is expected to violate the assumption that the value of V, given by equation 3.7, is always large so that the V^{-1} term in equation 3.9 can be neglected. The linearity between N_e and ρ_0 is therefore only expected to hold for small values of ρ_0 . From the gradient of the plot shown in figure 3.8 a value of $\sigma_i\Phi = 1.3 \times 10^{-20}$ cm^2 was obtained.

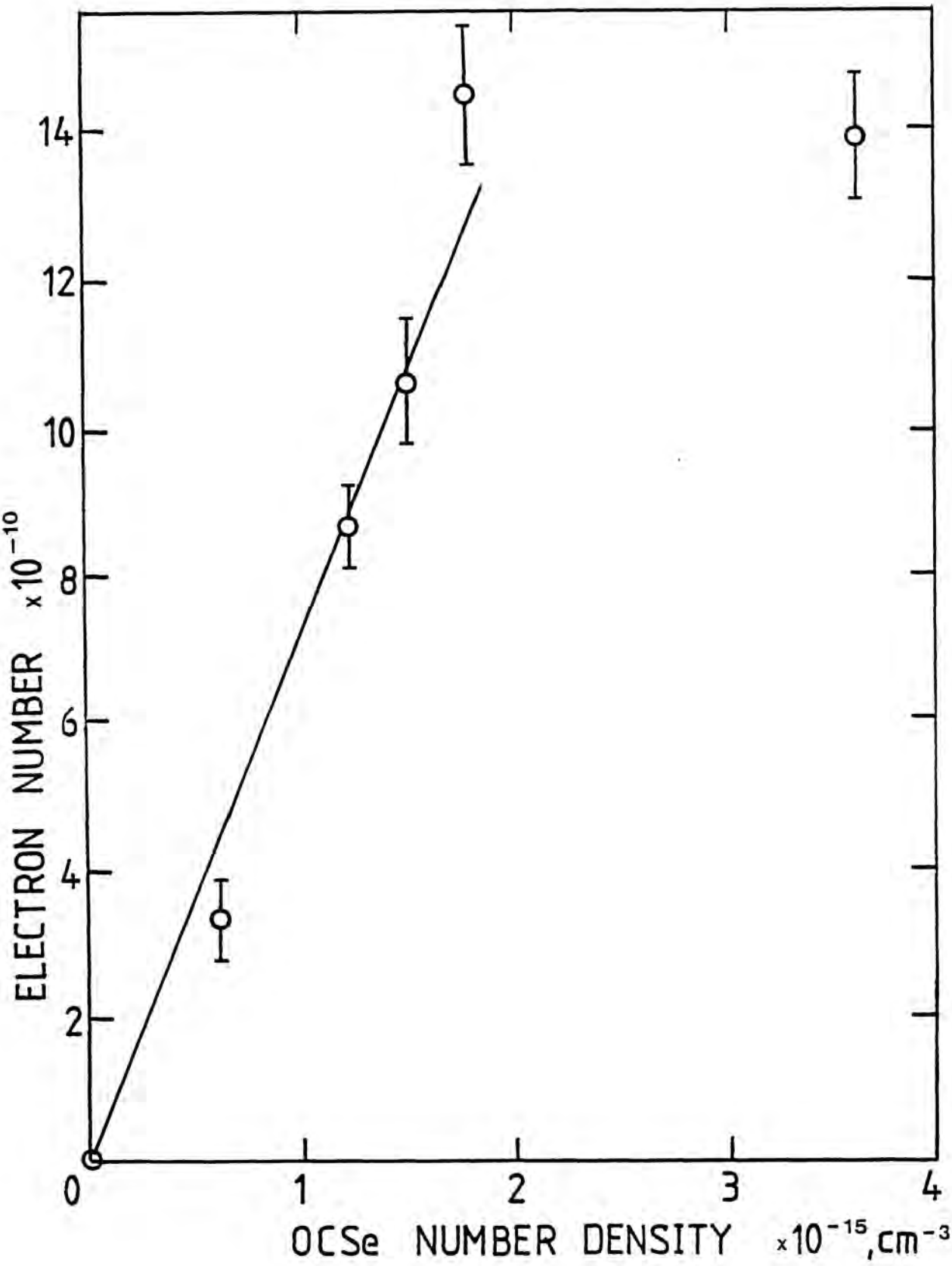

ELECTRON NUMBER x10⁻¹⁰
0
2
4
6
8
10
12
14
0
1
2
3
4
OCSe NUMBER DENSITY x10⁻¹⁵,cm⁻³

FIGURE 27

Measurements of the quantum yield Φ have shown it to be unity at 172 nm[72,73], thus a value of 1.3×10^{-20} cm^2 is determined for the photoionization cross section of $Se(^1S)$ at 172 nm.

Figure 28 shows the variation of the number of photoelectrons collected, N_e, for different xenon laser photon densities, E, with the OCSe number density, ρ_0, maintained constant. The continuous line drawn in the same figure shows the behaviour of the two variables as predicted by equation 3.10. Good agreement between theory and experiment shows that the two assumptions used to derive equation 3.10 are valid for low OCSe number densities and high photon densities. Under these conditions equation 3.10 predicts that the plot of N_e versus E should tend asymptotically, for large values of E, to a straight line of slope $\sigma_i \Phi \rho_0 AL$. The dotted line drawn in figure 28 represents this asymptote. From its slope a value of $\sigma_i = 1.2 \times 10^{-20}$ cm^2 was estimated, which is in good agreement (~8%) with the value obtained from the plot of N_e versus ρ_0. Equation 3.10 further indicates that the intercept of the asymptote with the N_e axis occurs at a value of $N_e = -\sigma_i \Phi \rho_0 AL \sigma_d^{-1}$. Thus a value of $\sigma_i = 1.1 \times 10^{-20}$ cm^2 is calculated.

A final check of the validity of the theory was provided by the intersection of the asymptote with the photon density axis. According to equation 3.10 this occurs at a value of $E = \sigma_d^{-1}$. A value of $\sigma_d = 0.8 \times 10^{-16}$ cm^2 was calculated which is in good agreement with the value of 0.9×10^{-16} cm^2 reported by Black[72].

The operation of the xenon laser in a tuned mode enabled plots of N_e versus E, similar to figure 28, to be constructed at different wavelengths within the 170 to 175 nm range. Values of the photoionization cross section estimated from these plots

20
16
12
8
4
0
-4
-8
ELECTRON NUMBER x10⁻¹¹
0
1
2
3
4
LASER PHOTON DENSITY , x10⁻¹⁶ , cm⁻²

FIGURE 28

are summarized in figure 29 . The value of σ_i obtained with the untuned laser is also shown for completeness. A minimum value of σ_i can be seen in the region 171 to 173 nm.

A systematic uncertainty of 25% in the value of σ_i is shown as error bars in figure 29. The most important sources of systematic error were:

a) The error in the measurement of the charge collected.

b) The error in the determination of the OCSe density.

c) The error in the measurement of the xenon laser energy.

Values of the charge indicated by the electrometer were shown to be within 2% of the calibration values. A total error of 5% was estimated in the measurement of the charge collected to account for errors in the measurement of the length of the collector electrode.

The calculation of the OCSe number density involved the calibration of the pirani gauge to read OCSe pressures. A maximum error of 5% was estimated. A further 5% error was attributed to the uncertainty in the value of the area of the chamber illuminated by the laser beam.

The energy meter used to measure the laser pulse energy was calibrated by the manufacturers (Laser Instrumentation). Comparison with other energy meters indicated that an error of 5 to 10% in the meter reading was to be expected.

3.7 Discussion

The photoionization cross section of Se(^{1}S) was estimated to be 1.2×10^{-20} ($\pm$25%) cm^2. In a recent measurement by Rice[88] in which an indirect method of measuring the number of photoelectrons was used, a value of $\sigma_i = 3 \times 10^{-19}$ cm^2 was reported

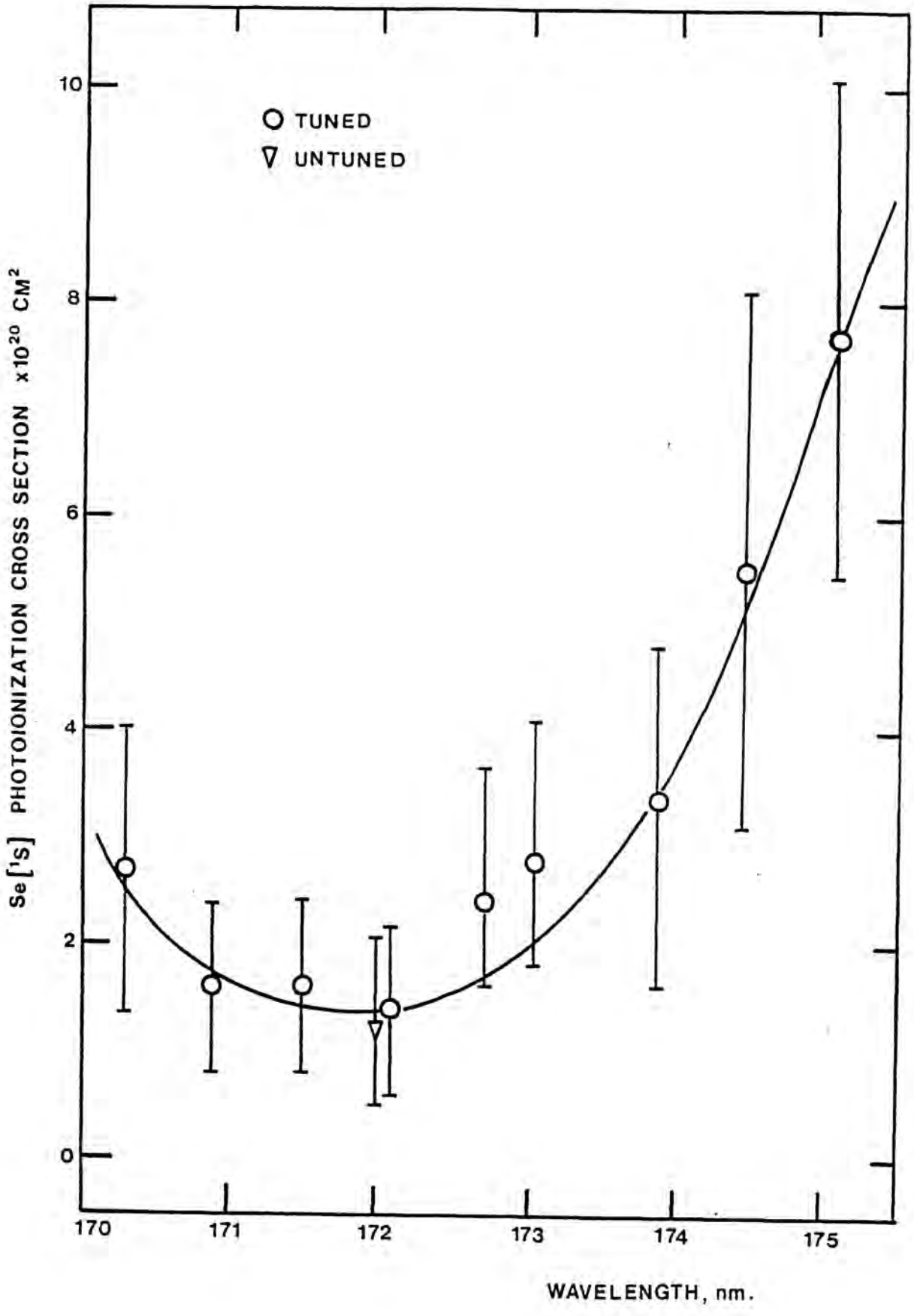

O TUNED
∇ UNTUNED
Se ['S] PHOTOIONIZATION CROSS SECTION x10^20 CM^2
0
2
4
6
8
10
170
171
172
173
174
175
WAVELENGTH, nm.

FIGURE 29

This value agrees well with a theoretically calculated value of 1.5×10^{-19} cm^2 reported by McGuire[89]. However, Rice also reported[89(a)] a value for the photoionization cross section of sulphur(^1S) which is found to be an order of magnitude less than the corresponding theoretical estimate of McGuire[89].

The variation of σ_i with wavelength shown in figure 29 shows a similar trend to that calculated by McGuire. However the theoretical estimates show σ_i to change by three orders of magnitude within the tuning range of the xenon laser. This change is much more dramatic than the variation shown in figure 29.

The measured value of the photodissociation cross section σ_d of OCSe is in good agreement (within 20%) with the values reported by Black[72] and Finn[75].

The number of photoelectrons collected was found to be independent of the pressure of N_2 buffer gas added. This implied that for the Se(^1S) concentrations used in this experiment ($\sim 10^{15}$ cm^{-3}) electron multiplication did not take place.

The value of the photoionization cross section estimated here is nearly four orders of magnitude smaller than the photodissociation cross section of OCSe. This suggests that there is a wide range of values of laser flux over which bleaching of the OCSe can be achieved whereas direct loss of Se(^1S) by absorption of pump radiation can be insignificant.

Since the maximum value of Φ and the minimum value of σ_i both lie at 172 nm, the xenon laser appears a suitable candidate for the excitation of Se(^1S) by the photodissociation of OCSe.

CHAPTER 4

ABSOLUTE DETERMINATION OF THE PHOTOIONIZATION CROSS SECTION OF GROUND STATE CAESIUM AT 172 nm

4.1 Introduction

Alkali metals are characterized by one valence electron outside a closed shell of core electrons. The core electrons are expected to shield the nucleus from the valence electron, thus leaving a net nuclear charge of one interacting with the valence electron. The term structure of alkali metals is therefore essentially hydrogenic, making them good candidates for theoretical treatment.

Their importance in a variety of laboratory processes coupled with the fact that for alkali metals theory and experiment can be easily compared, has stimulated a number of investigations into their properties. Historically the agreement between theoretical and experimental measurements has been poor. This is the situation concerning the photoionization of ground state caesium.

The aim of the work described in this chapter is to measure the photoionization cross section of ground state caesium at 172 nm. This is a photodissociation process described by:

$$Cs(6s,\,^2S_{\frac{1}{2}}) + h\nu(172\ nm) \longrightarrow Cs^+ + e^- \qquad (4.1)$$

4.2 Summary of previous work

The first investigation of the photoionization cross section of ground state caesium was reported by Mohler[90] in 1926, who used the effect of positive ions on a thermionic current, which

is limited by negative space charge to detect photoionization. This method is very sensitive[91,92] but appears prone to a certain amount of instability and is incapable of giving an absolute value of the cross section[93].

All subsequent attempts to measure the photoionization cross section absolutely can be classified as either "direct" or "indirect" measurements. In a "direct" measurement, as used by Little[94], Mohler and Boeckner[95] and Cook et al[96], the number of photoions produced by the passage of light though caesium vapour is measured. Knowing the photon flux, the density of caesium vapour and the cell geometry, the cross section can be calculated.

In an "indirect" measurement, as used by Braddick and Ditchburn[97] and Marr and Creek[98], the ratio of the transmitted intensity of light through a cell with and without caesium vapour is measured. Knowing the density of the vapour and the cell geometry, the cross section can be calculated.

Theoretical values of the cross section have been reported by Weisheit[99] and Norcross[100] in the wavelength regions extending to 150 nm and 230 nm respectively. Both theoretical calculations used a semi-empirical model potential to approximate the field due to the inner core electrons. While the two calculations are in good agreement with each other (~15%) and with the experimental values obtained by Cook et al[96], they are approximately a factor of 2 lower than all other experimental values. Cook et al [96] who used the second harmonic of a dye laser crossed with a particle beam of ground state caesium atoms for their direct experiment, were able to report values of the cross section down to 240 nm.

The present experiment was undertaken in order to resolve

the discrepancy between the theoretical[99] and experimental[98] values of the photoionization cross section of ground state caesium in the VUV. Comparison between this measurement and independent estimates of the photoionization cross section of caesium can also provide a check on the accuracy of the measurement of the photoionization cross section of Se(^{1}S) as described in chapter 3.

4.3 Theoretical background

Consider a cell containing caesium vapour of atomic density n_c . When ionizing radiation of wavelength λ and photon flux density $F(\lambda,t)$ enters the cell, the rate of photoionization is given by:

$$\frac{dn_e}{dt} = \sigma_i(\lambda) n_c F(\lambda,t) \qquad (4.2)$$

where n_e is the electron (or ion) number density and $\sigma_i(\lambda)$ is the photoionization cross section of caesium at wavelength λ .

The photoelectron density is obtained by integrating eq. 4.2:

$$n_e = \sigma_i(\lambda) \int_0^\infty n_c F(\lambda,t)\,dt \qquad (4.3)$$

If the density of ground state caesium atoms is not significantly altered by the ionizing radiation, n_c can be considered a constant so it can be taken out of the integral:

$$n_e = \sigma_i(\lambda) n_c \int_0^\infty F(\lambda,t)\,dt \qquad (4.4)$$

The integral is now the photon density:

$$\int_0^\infty F(\lambda,t)\,dt = \frac{P}{A} \qquad (4.5)$$

where P is the total number of photons in the laser pulse and

A is the laser beam cross sectional area.

The total number of photoelectrons generated can be written as:

$$N_e = n_e A l \tag{4.6}$$

where l is the interaction length. Substituding equations 4.5 and 4.6 in equation 4.4:

$$N_e = \sigma_i(\lambda) n_c l P \tag{4.7}$$

The photoionization cross section $\sigma_i(\lambda)$ can therefore be determined by measuring the total number of photoelectrons produced by a laser pulse of known energy provided the atomic density of caesium can be measured. Note that the cross sectional area A of the laser beam does not enter equation 4.7. Thus the errors arising from the measurement of the interaction volume are minimized since only the interaction length l needs to be determined.

4.4 The experimental apparatus

The apparatus used for the measurement of the photoionization cross section of atomic caesium was based on the ionization detector described in chapter 3. The detector was housed in a modified chamber to allow the uniform heating of the chamber to temperatures up to 420 K.

The chamber was placed in a large (30 cm x 30 cm x 40 cm) home made oven whose temperature could be controlled to ±1 K. The walls of the oven were made of Trident ceramic fibre boards sandwiched between aluminium sheets. The walls were attached to speedframe and could be easily removed for easy access to the chamber. Two small apertures on opposite sides of the oven allowed the admission and exit of the xenon laser beam. The

apertures were slightly larger than the diameter of the evacuated pipe used to transport the laser beam. The section of the pipe inside the oven was wrapped with heating tape and heated 5 K higher than the oven temperature to prevent the deposition of caesium metal on the spectrasil windows. Two more small apertures in the oven walls allowed extension rods to manipulate taps connecting the chamber to the vacuum system and the chamber to the caesium side-arm reservoir.

Heating was provided by three 1 kW commercially available heaters, placed symmetrically inside the oven. The electric current through the heaters was controlled by a platinum probe temperature regulator via a system of relays. An independent safety cut off was incorporated to switch off the current if the temperature of the oven exceeded 430 K. Heat resistant wire was used for all connections. The oven was operated in the temperature region 350 to 400 K to obtain caesium pressures in the region of 1.2×10^{-4} to 3×10^{-3} Torr.

Caesium was prepared by Mr B. Weekly by the reduction of caesium chromate with powdered aluminium using materials of spectroscopic quality ($>$ 99.9% purity). Caesium was distilled into a glass ampule and sealed under vacuum. Five turns of nickel wire were wound round the ampule before it was placed in the glass side-arm which was connected to the chamber via a stainless steel packless valve. The ampule was broken using a magnet when the system was evacuated to less than 10^{-6} mbar.

Knowledge of the cross sectional area of the xenon laser beam was not required (see equation 4.7). A 4 mm diameter aperture, placed in front of the entrance window, was introduced to collimate the beam entering the chamber. The aperture was at the centre of a thin perspex disc. Black ink was used

to paint the disc. After a few shots, the black ink had been removed from areas of the disc exposed to the xenon laser radiation. Using this effect the alignment of the system could be checked. From the shape of the burn mark, the cross sectional area of the beam was shown to be circular to within 8%.

Stainless steel was used were possible since other metals are chemically attacked by caesium vapour. A 10 mm long collector electrode was used in the ionization detector. Charge was measured using the calibrated Keithley 601 electrometer. The temporal profile of the charge collected was displayed on a fast oscilloscope (Tektronix type 7904). The xenon laser pulse energy was measured using the energy meter (Laser Instrumentation Model 142 LR).

4.5 Experimental results

Initially the characteristics of the ionization detector were determined. The temperature of the oven was allowed to stabilise for approximately 12 hours to ensure a uniform caesium atomic number density throughout the chamber. The energy output of the xenon laser was kept constant to ensure the generation of equal numbers of photoelectrons inside the interaction volume for every laser shot. Values of the charge collected for different values of the repelling potential are shown in figure 30. Because of the low pressure inside the chamber ($\sim 10^{-3}$ Torr) the mean free path of the electrons and caesium ions was considerably greater than the 1 cm dimension of the detector. The mobility of the charge particles was expected to be high and the collection of all ions generated was achieved with values of the repelling voltage as low as

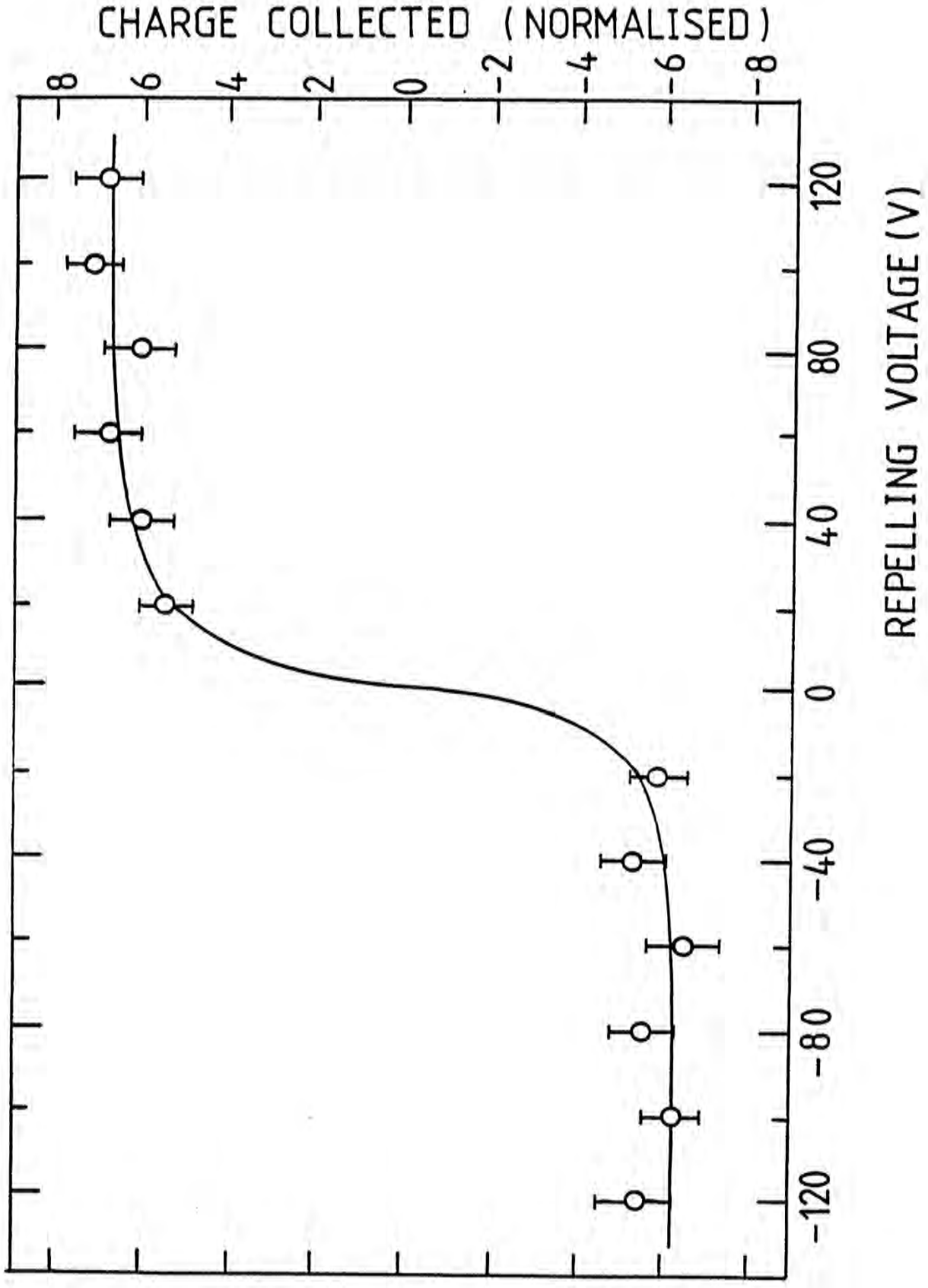

CHARGE COLLECTED (NORMALISED)
8
6
4
2
0
-2
-4
-6
-8
120
80
40
0
-40
-80
-120
REPELLING VOLTAGE (V)

FIGURE 30

± 20 V . A repelling voltage of + 100 V was used in all subsequent work on caesium.

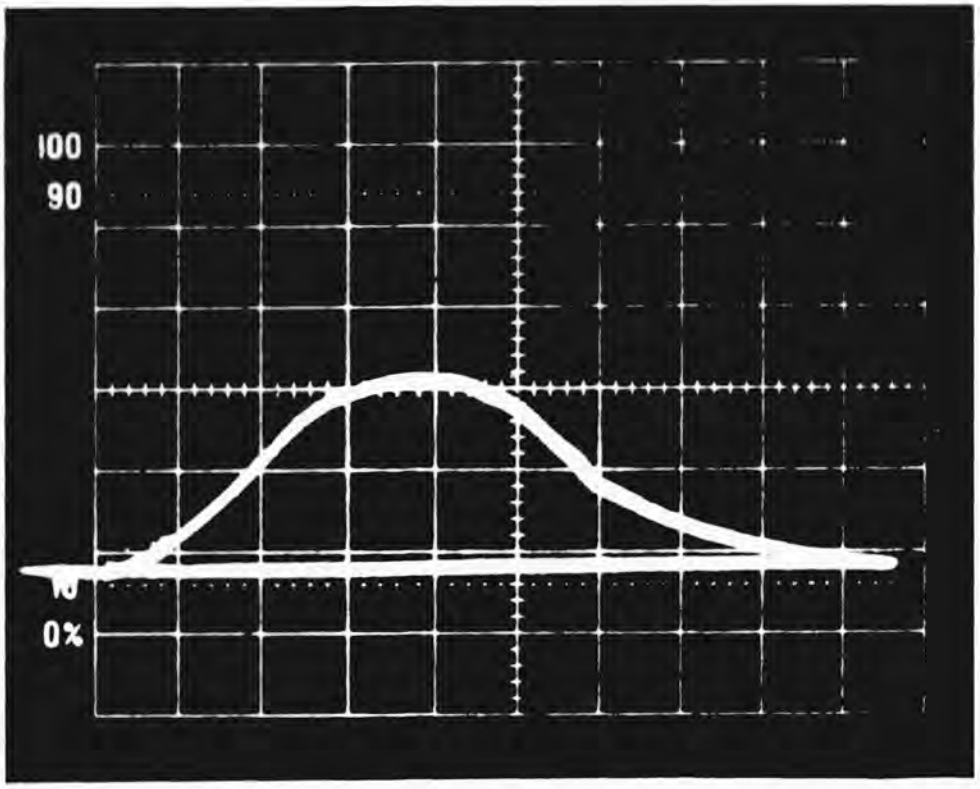
Plate 6 shows the temporal profile of the collection of the charge generated. The oscilloscope sweep speed was 2 μs/div..

In order to measure the photoionization cross section, the positive charge collected was monitored as a function of the xenon laser pulse energy entering the chamber for eight different temperatures in the region of 350 to 400 K. Figure 31 shows one such plot obtained at a temperature of 388 K. The plot is a straight line in agreement with equation 4.7. The gradient of each plot gave a value of $\sigma_i n_c$, where n_c is the caesium atomic density at the operating temperature.

Figure 32 shows the variation of the product $\sigma_i n_c$ estimated at different temperatures, as a function of the caesium atomic density n_c , calculated from the vapour pressure measurements published by Honig[101]. From the gradient of figure 32 , the photoionization cross section of ground state caesium was estimated to be 0.9×10^{-19} (±30%) cm^2.

4.6 Discussion

Equation 4.7 is valid provided the caesium number density remained constant throughout the interaction volume, throughout the duration of the laser pulse. A reduction of the caesium ground state density n_c due to photoionization, of less than 1% required that the product $\sigma_i PA^{-1}$ should be less than 0.01%. This implied that there was an upper limit on the value of the photon density, PA^{-1}. Variation of the pulse energy of the xenon laser by more than an order of magnitude showed no saturation of the photoionization process (see figure 31). Furthermore, no space charge effects became apparent for the



TEMPORAL PROFILE OF THE CHARGE

COLLECTED (2 μs/div.)

PLATE 6

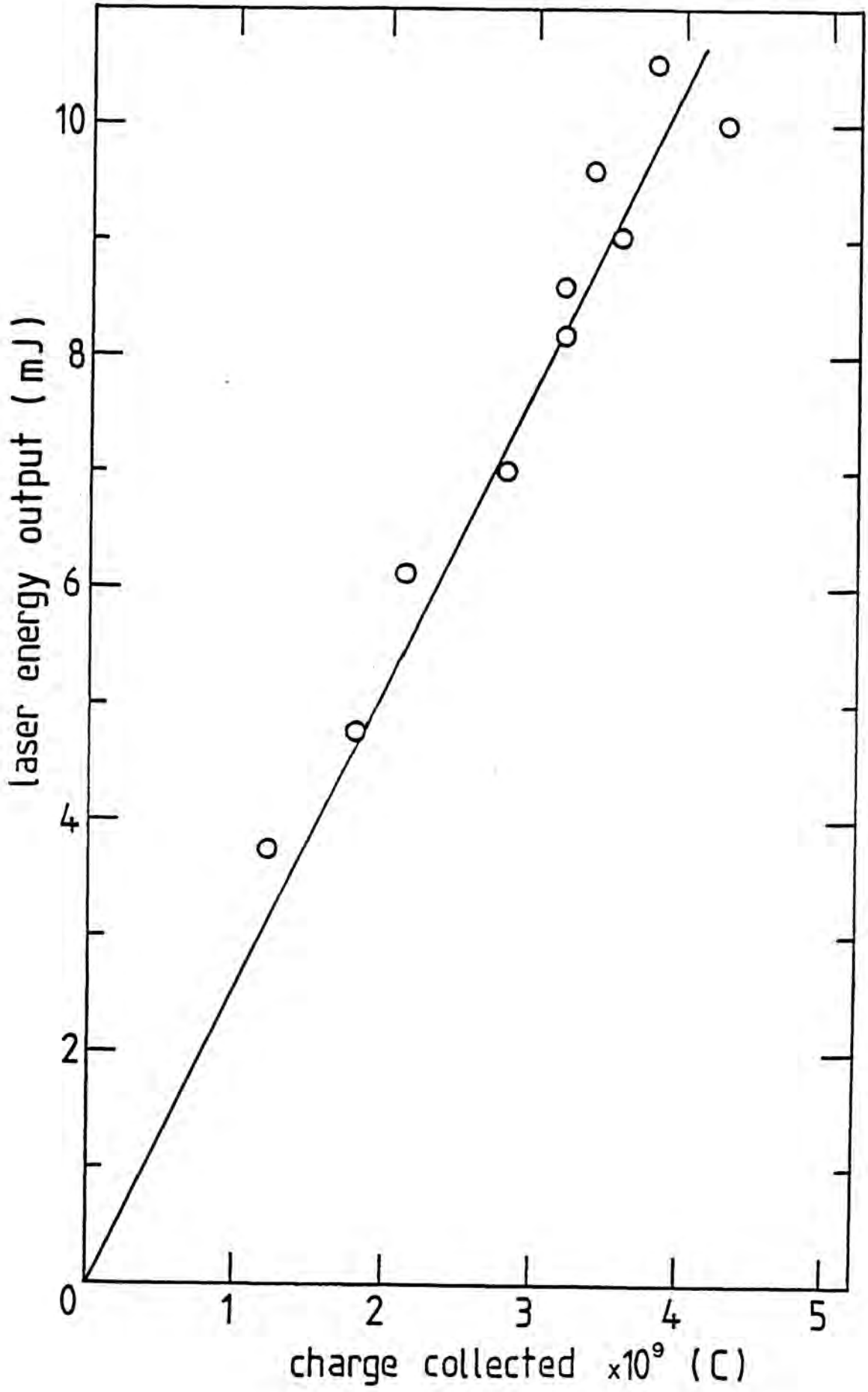

laser energy output (mJ)
0
2
4
6
8
10
1
2
3
4
5
charge collected x10⁹ (C)

FIGURE 31

GRADIENT , $\sigma_i n_c$, $\times 10^6$ (cm^{-1})
CAESIUM NUMBER DENSITY $\times 10^{-13}$(cm^{-3})
0
2
4
6
8
10

FIGURE 32

degree of ionization produced during this experiment.

The major sources contributing to the uncertainty in the value of σ_i were:

a) The error in the determination of the caesium density.

b) The error in the measurement of the charge collected.

c) The error in the measurement of the photon density of the incident laser pulse.

Accurate knowledge of the caesium number density required accurate measurement of the oven temperature. The maximum error in the measurement of the value of the temperature was estimated to be $\pm$ 2 K, including the contribution due to the error of the temperature probe. Using the recent determination of the caesium vapour pressure by Honig[101] a $\pm$ 15% error in n_c was estimated at 380 K. The error arising from the photoionization of the caesium molecules Cs_2 , was estimated to be less than 1%[102, 103].

Uncertainties in the measurement of the charge collected and of the laser energy were identical to the values reported for the measurement of the photoionization cross section of $Se(^1S)$ (see chapter 3). Secondary emission from the collector electrode due to the bombardment by low energy caesium ions was estimated to be negligible[104] since the energy of the caesium ions was much less than 100 eV.

A total error of $\pm$30% was thus estimated for the measurement of the photoionization of ground state caesium.

The result of this experiment is shown in figure 33, together with some of the previously published values for comparison. This result appears to substantiate the theoretically calculated value by Weisheit[99] at the same wavelength. The present experiment is not consistent with previous measurements by Marr and Creek[98]. The agreement between the present result

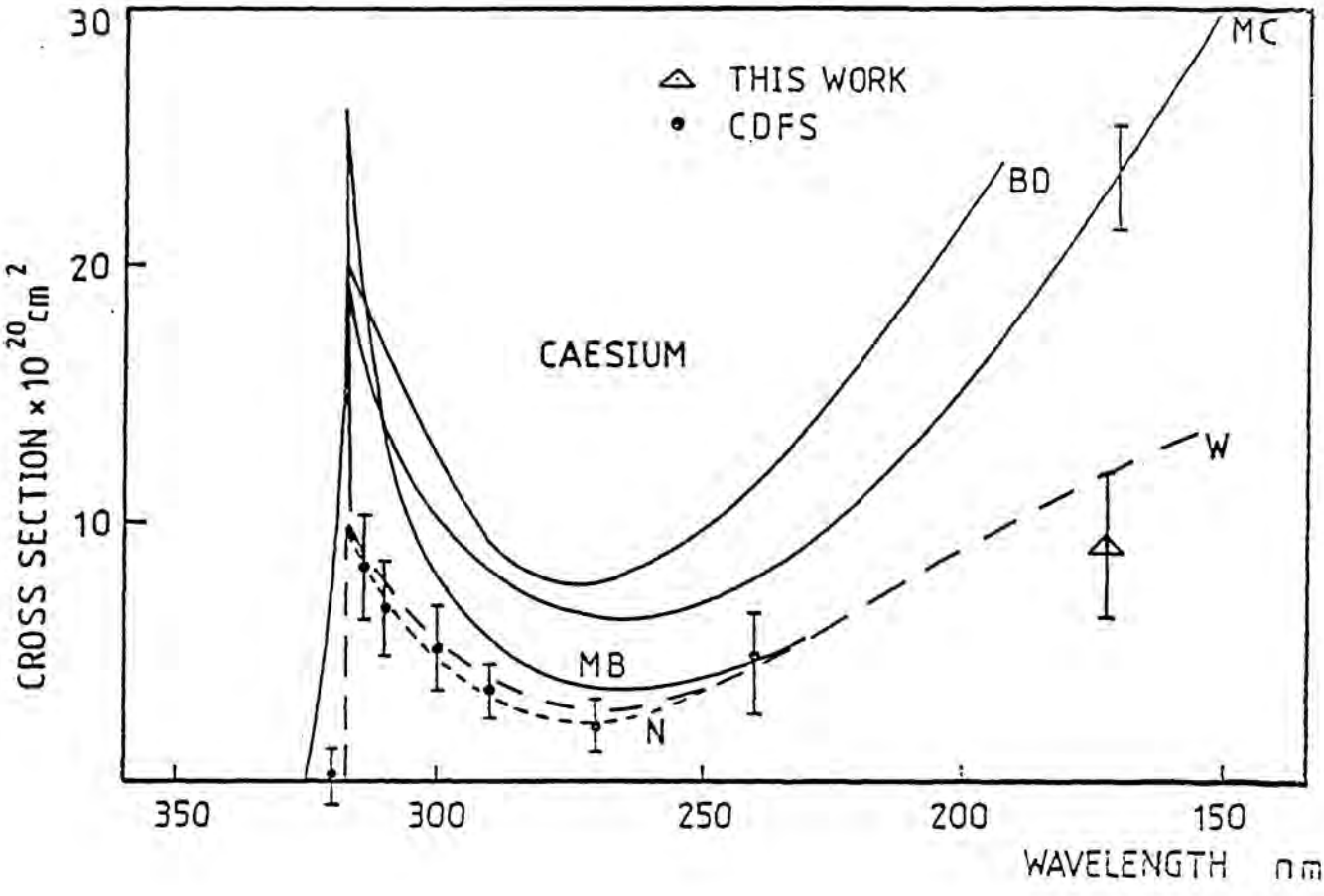


FIGURE 33

Comparison with other work. Solid lines represent experimental measurements, (BD - Braddick and Ditchburn[97], MB - Mohler and Boeckner[95], MC - Marr and Creek[98], CDFS - Cook et al[96]), with earlier results reflecting modern vapour pressure measurements (Honig[101]). Dashed lines represent theoretical work, (W-Weisheit[99], N - Norcross[100]).

with the theoretical work just noted suggests that the measurements of Marr and Creek must be in error. They obtained their measurements in a cell raised to a temperature ranging from 570 to 620 K. In addition to questions about the accuracy of the vapour pressure data, at high pressures the concentration of caesium dimers, Cs_2 , is known to become significant[102,103].

In conclusion, the photoionization cross section of ground state atomic caesium at 172 nm was measured to be 0.9×10^{-19} ($\pm 30\%$) cm^2. This value is in good agreement with theoretical calculations, but is in disagreement by a factor of two with previous experimental measurements.

CHAPTER 5

PHOTODISSOCIATION STUDIES IN THE MERCURIC HALIDES

5.1 Introduction

Since the operation of the first laser[105], a search has been going on for the discovery of efficient, high power lasers operating in the visible and ultra-violet part of the spectrum. The rare gas halide lasers, whose output scans the ultra-violet have been shown to be one of the few success stories of this search. Mercury halide lasers appear promising candidates to fill the visible part of the spectrum.

Lasing has been achieved in HgI(443 nm), HgBr(502 nm) and HgCl(558 nm) using E-beam pumping[106,107], transverse discharge excitation[108,109] and by photodissociation of the parent mercuric halide, HgX_2(X = I, Br and Cl)[110,111], according to the reactions:

$$HgX_2 + h\nu_p \longrightarrow HgX_2^*$$

$$HgX_2^* \longrightarrow HgX^* + X$$

$$HgX^* \longrightarrow HgX + h\nu_f$$

Photodissociation continua correlating to specific dissociation channels have spectral bandwidths of several thousand cm^{-1}. Molecular photodissociation thus permits the coupling of large amounts of optical energy into a gas. The excitation of the mercuric halides by photodissociation can be of practical interest since the HgX radical in its ground state can combine with a free halogen atom to form HgX_2[110]. The construction of such a laser can thus be simple and inexpensive,

involving only a heated, sealed off dissociation cell and a pump source.

Excitation of the HgX(B $\longrightarrow$X) fluorescence gives rise to emissions with broad bandwidths ($\Delta\lambda > 100$ nm), because the vibrational levels of the upper state are not relaxed. Vibrational relaxation can be achieved by adding a buffer gas. This reduces the emission bandwidth, thus increasing the gain. In order to optimize the efficiency of these lasers, an accurate knowledge of the quenching coefficients of the upper laser states by the various buffer gases is required.

The xenon laser described in chapter 2 is shown to be capable of populating the $HgX^*(B^2\Sigma_{\frac{1}{2}})$ states by photodissociation of the HgX_2 parent molecule. In this experiment the variation of the intensity of the HgX(B $\longrightarrow$X) emission with the concentration of argon or xenon gas was used to determine the quenching coefficients of $HgX^*(B^2\Sigma_{\frac{1}{2}})$ by argon or xenon.

5.2 Historical background

The first report of the emission produced by the mercuric halides was by Pierce[112] in 1879, who made his observations in an electric discharge. In 1926 Terenin[113] reported that the irradiation of HgX_2 vapour with ultra-violet light produced strong visible fluorescence. Terenin subsequently assigned[114] the emission bands to HgX radicals, realizing that the photodissociation of HgX_2 produced an excited HgX^* radical and a ground state halogen atom, X. His conclusions were in good agreement with earlier theoretical predictions by Mulliken[115].

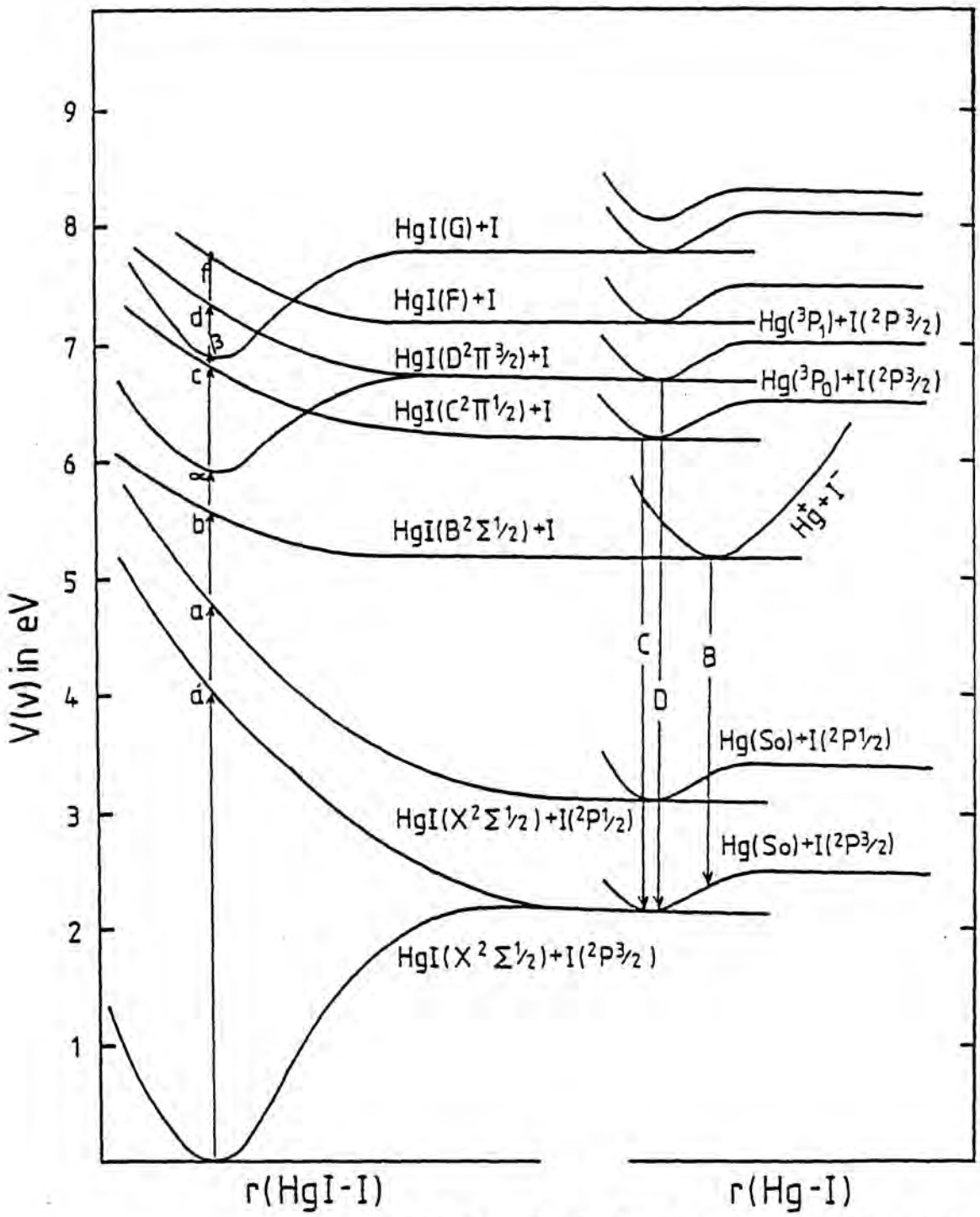
Terenin's work was continued by Butkow[116], Spooner[117], Kondratjew[118] and Wieland[119,120] who reported a series of studies into the spectroscopy of the mercuric halides.

Wieland was able to separate up to eight absorption bands for each of the mercuric halides in the wavelength region extending from 150 to 300 nm. Using different light sources and filters Wieland[120] was able to correlate different absorption continua with different fluorescence emissions. Although the results reported in this chapter do not agree entirely with Wieland's observations, his work remains the most complete single source of information on the spectroscopy of the mercuric halides.

Recent interest in the spectroscopy of the mercuric halides has been accelerated when Singer and Gorog[121] and Rautian and Sobelman[122] realized that photodissociative processes which produce excited state fragments can be used to produce population inversion in excited atoms or radicals. In 1965 Zare and Herschbach[123] proposed the mercuric halide dissociation lasers. However, no intense ultra-violet pump source was available[124] so the first demonstration of photodissociation as a laser pumping scheme was not made in a mercuric halide but in CF_3I and CH_3I molecules where the iodine atom lased at 1.315 μm[125]. This lasing transition was aided by the lower lasing threshold condition afforded by the use of an atomic line. With the availability of the rare gas monohalide lasers, lasing action has been observed in HgBr[110], HgCl[111] and HgI[108] by photodissociating the HgX_2 parent molecule.

5.3 The spectroscopy of the mercuric halides

Wieland was the first to attempt to construct the potential energy curves of the mercuric halides on the basis of the correlation of the different absorption and emission bands. Figure 34 shows the energy levels of HgI_2 and HgI , based on the dissociation paths deduced by Wieland[120]. Similar energy



ENERGY LEVELS OF HgI_2 AND HgI

FIGURE 34

curves can be drawn for the $HgCl_2$ and $HgBr_2$.

Absorption studies have shown the existence of continuous as well as discrete bands. Continuous absorption bands a,b, c,d ..., in order of decreasing wavelength, were identified and named by Wieland. Greek letters $\alpha, \beta, \gamma, \ldots$ denote discrete bands.

In the HgI_2 , the first absorption band "a" occurs at 270 nm. Butkow[116] identified it with the production of $HgI(X^2\Sigma_{\frac{1}{2}})$ and a ground state iodine atom, $I(^2P_{3/2})$. In a recent experiment Hoffman and Leone[126] showed that both excited and ground state iodine atoms are produced and measured the wavelength dependent branching ratio for the $I(^2P_{\frac{1}{2}})$ and $I(^2P_{3/2})$ production.

Wieland reported[120] that the absorption of radiation in the b,c and d bands stimulated the B,C and D emission bands respectively. A particular fluorescence band is thus associated with a particular absorption band. However, the same fluorescence band may be excited with an even higher efficiency by the absorption of light in a continuum of shorter wavelength[127]. Furthermore, absorption of radiation in the α and β bands is still known to stimulate the fluorescence of the diatomic radical, provided such a process is energetically possible. All these observations suggest numerous curve crossings in the trimer, in accordance with the theoretical predictions of Wadt[128].

The first excited state of the mercury halide radical $HgX^*(B^2\Sigma_{\frac{1}{2}})$ is predominantly ionic and is formed from the $Hg^+(^2S)$ and $X^-(^1S)$ states[129]. The ground state, labelled $HgX(X^2\Sigma_{\frac{1}{2}})$ is found to be predominantly covalent. The difference in nature of the two states gives rise to a large relative displacement of their respective equilibrium internuclear distances. Transitions from the lowest vibrational level of

the upper state $HgX^*(B^2\Sigma_{\frac{1}{2}})$ are found to terminate to very high vibrational levels of the ground state. This can be used to generate population inversion between the two states. Parks observed no bottlenecking of the lower laser level under lasing conditions[106,107].

5.4 Theoretical background

Assume the excitation of the $HgX^*(B)$ state by the photodissociation of HgX_2 in a period considerably shorter than the radiative lifetime of the $HgX^*(B)$. If $\left[HgX^*(B)\right]_{(0)}$ and $\left[HgX^*(B)\right]_{(t)}$ denote the population densities of $HgX^*(B)$ at times 0 and t seconds respectively, then they are connected by the relationship:

$$\left[HgX^*(B)\right]_{(t)} = \left[HgX^*(B)\right]_{(0)} \exp\left(\frac{-t}{\tau}\right) \qquad (5.1)$$

where:

$$\frac{1}{\tau} = \frac{1}{\tau_R} + k_1[Q] + k_2[Q]^2 \qquad (5.2)$$

τ_R is the $HgX(B \longrightarrow X)$ radiative lifetime and k_1 and k_2 are the two and three body quenching constants of $HgX^*(B)$ by the species of concentration Q .

By varying the pressure of the quenching gas Q , the fluorescence profile can be obtained at different concentrations of Q. For short pulse excitation, the fluorescence intensity will quickly reach a maximum and then will decay exponentially, the rate of decay governed by equation 5.2 . By plotting the decay rates obtained at different concentrations of Q, the quenching constants k_1 and k_2 can be estimated. Furthermore, by extrapolating to zero concentration of Q, a value for the

radiative lifetime τ_R of the $HgX^*(B \longrightarrow X)$ transition can be obtained.

5.5 The experimental apparatus

The apparatus consisted of a small stainless steel cell which could be evacuated to pressures less than 10^{-6} Torr and heated up to 450 K using the oven described in chapter 4. Samples of solid HgX_2 salts were inserted in a glass side-arm which was connected to the photodissociation cell via a stainless steel packless valve. The valve could be adjusted from outside the oven. The mercuric halide salts used in this experiment were of reagent grade and were supplied by B.D.H. Chemicals.

A Vacuum Generators CR 14 all metal valve joined the cell to argon and xenon reservoirs.

The population densities of the mercuric halides was estimated from the knowledge of the oven temperature using the vapour pressure data published by Quille[130]. The photolysis radiation was obtained from the xenon excimer laser described in chapter 2. The 172 nm radiation transmitted through the mercuric halide vapour was analysed using a one metre, home made, concave grating spectrograph. The excited HgX^* radicals produced upon photodissociation of HgX_2 were detected by monitoring their fluorescence using an I.T.L. photodiode with an S5 photocathode, through an appropriate narrow band transmission filter. The signal was displayed on a Tektronix type 7904 oscilloscope. Time integrated spectra of the fluorescence signal were recorded using a Chelsea Instruments type S-100 grating spectrograph. A 20 cm focal length quartz

lens was used to focus the fluorescence light onto the entrance slit of the spectrograph, thus improving its collection efficiency. The spectra were analysed on a Joyce-Loebl microdensitometer.

5.6 Experimental results

Maya[131] reported values of the absorption cross section of the ground state of the HgX_2 (X=Cl,Br,I) for wavelengths down to 200 nm which are in the region of 10^{-17} cm^2. Furthermore, it was pointed out[132] that the absorption cross sections were found to be consistently higher as the wavelength decreased because of the larger densities of dissociative states at higher energies.

From the formula $E_s = h\nu\sigma^{-1}$, a high absorption cross section σ implies a low saturation energy flux E_s for the excitation of the medium. For example, a value of $\sigma = 10^{-16}$ cm^2 implies a saturation flux of 10 mJ cm^{-2}. The xenon laser can provide at least 100 mJ cm^{-2}, thus ensuring the complete saturation of the absorption of the HgX_2 parent molecules.

Absorption of a 172 nm photon causes the HgX_2 to dissociate. The propagation of a 172 nm pulse through the HgX_2 vapour is therefore identical to the propagation of a laser pulse through a saturable absorber of infinitely long recovery time.

Consider a plane wave of photon flux P(t) propagating through an absorbing medium of uniform number density n. The wave will propagate into the absorber by bleaching the absorbing molecules. The velocity of propagation of the front that divides the opaque from the transparent parts of the medium is given by[133]:

$$V = \frac{P(t)}{n} \qquad (5.3)$$

The transition length between opaque and transparent regions of the medium is equal to the absorption length of the medium, given by[133]:

$$L = \frac{1}{n\sigma} \qquad (5.4)$$

For a particular point in the medium, the time taken between the arrival of the leading edge of the pulse and the complete bleaching of the medium at that point, is equal to the time taken for the bleaching wavefront to propagate through one absorption length. Using equations 5.3 and 5.4 :

$$T = \frac{1}{\sigma P(t)} \qquad (5.5)$$

A 10 ns xenon laser pulse of 30 mJ energy has a photon flux of 10^{25} photons cm^{-2} s^{-1}. For an absorption cross section of 10^{-16} cm^2, the effective excitation of the medium is T = 1 ns. This is considerably shorter than the theoretically calculated lifetimes of the $HgX^*(B)$ states[134]. Note that the excitation time of the medium, given by equation 5.5, is independent of the density of the absorber, provided the absorption losses cause an insignificant reduction in the laser pulse photon flux.

The validity of the above theory was checked by examining the temporal profile of the xenon laser pulse transmitted through the same length of a cell containing different number densities of HgI_2 molecules. The transmitted signal was monitored using a solar blind photodiode and displayed on a Tektronix type 519 oscilloscope. The oscilloscope was triggered externally from the output of a second solar blind photodiode, which was monitoring the xenon laser radiation entering the

photodissociation cell. This way the relative positions in time of the transmitted pulses could be compared.

Plate 7(a) shows the temporal profile of the transmitted pulse when the absorption cell was maintained at 298 K. The xenon laser output could bleach the HgI_2 vapour with negligible effects on its temporal profile. Increasing the temperature of the oven to 373 K required the xenon laser pulse to spend its leading edge in bleaching the column of HgI_2 vapour through which it passed (see plate 7(b)). From the same plate it can be seen that the presence of the absorption cell appeared to have no effect on the trailing edge of the laser pulse. This confirms the suggestion that the excitation of HgI_2 vapour took place on a much shorter time scale than the duration of the excitation pulse.

Plate 7(c) shows the xenon laser pulse transmitted through the HgI_2 cell whose temperature had been raised to 398 K. The laser pulse appeared to be just capable of bleaching its way through the absorption cell. At higher temperatures no transmission was observed.

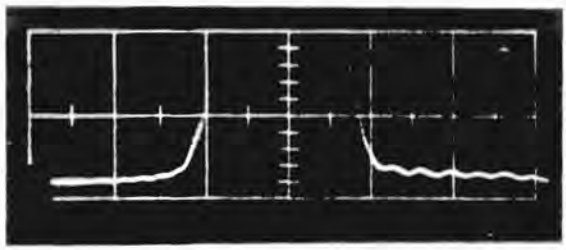
Using an S-5 photodiode in combination with a narrow band filter, the temporal position of the HgI ($B \longrightarrow X$) emission was recorded , using the same arrangement to externally trigger the type 519 displaying oscilloscope. Plate 7(d) shows the fluorescence signal obtained at a cell temperature of 373 K. The emission can be seen rising to a maximum and then decaying slowly. What is important is that the fluorescence maximum occurred well before the peak of the excitation pulse had been reached. This was a confirmation that the excitation of the medium took place on a time-scale much shorter than the duration of the xenon laser pulse.

Plate 7(a) Temporal profile of the xenon laser ouput transmitted through a HgI_2 cell, maintained at 298 K, 20 ns/div.

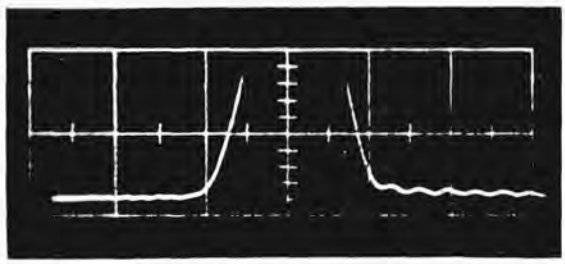
Plate 7(b) Temporal profile of the xenon laser output transmitted through a HgI_2 cell, maintained at 373 K, 20 ns/div.

Plate 7(c) Temporal profile of the xenon laser output transmitted through a HgI_2 cell, maintained at 398 K, 20 ns/div.

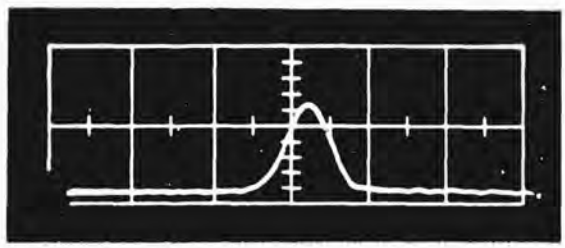
Plate 7(d) Temporal profile of the HgI(B $\rightarrow$ X) emission excited by the photodissociation of HgI_2 vapour, at an oven temperature of 373 K, 20 ns/div.



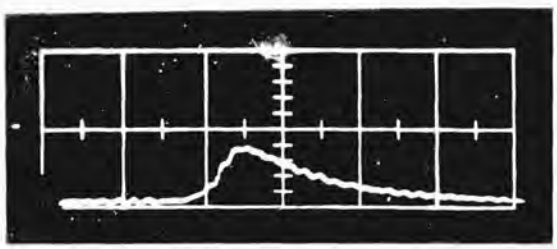
(a)



(b)



(c)



(d)

PLATE 7

5.6.1 Studies in the HgI_2

Initially the absorption spectrum of HgI_2 was recorded in the wavelength region 169 to 175 nm, at a vapour pressure corresponding to an oven temperature of 373 K. Continuous absorption was observed, in agreement with the observations of Wieland[120].

From the HgI_2 energy level diagram, shown in figure 34, absorption of a 172 nm photon is expected to populate the trimer state dissociating to a $HgI^*(D)$ excited radical and a ground state iodine atom. However, no $HgI(D \rightarrow X)$ emission was observed, while both $HgI(C \rightarrow X)$ and $HgI(B \rightarrow X)$ emissions were recorded. This observation is in disagreement with the published data of Wieland[120]. However, in recent studies[135] where a xenon flashlamp was used to excite the HgI_2 vapour, no $HgI(D \rightarrow X)$ emission was observed, in agreement with the results of the present experiment. Three reasons are put forward to account for the discrepancy between the results of this work and the observations of Wieland:

a) The $HgI(D \rightarrow X)$ emission lies in the region of 265 to 280 nm. However, this region coincides with the "a" absorption band of the HgI_2 ground state molecule. Thus the $HgI(D \rightarrow X)$ fluorescence emitted can be readily reabsorbed by the HgI_2 unexcited vapour.

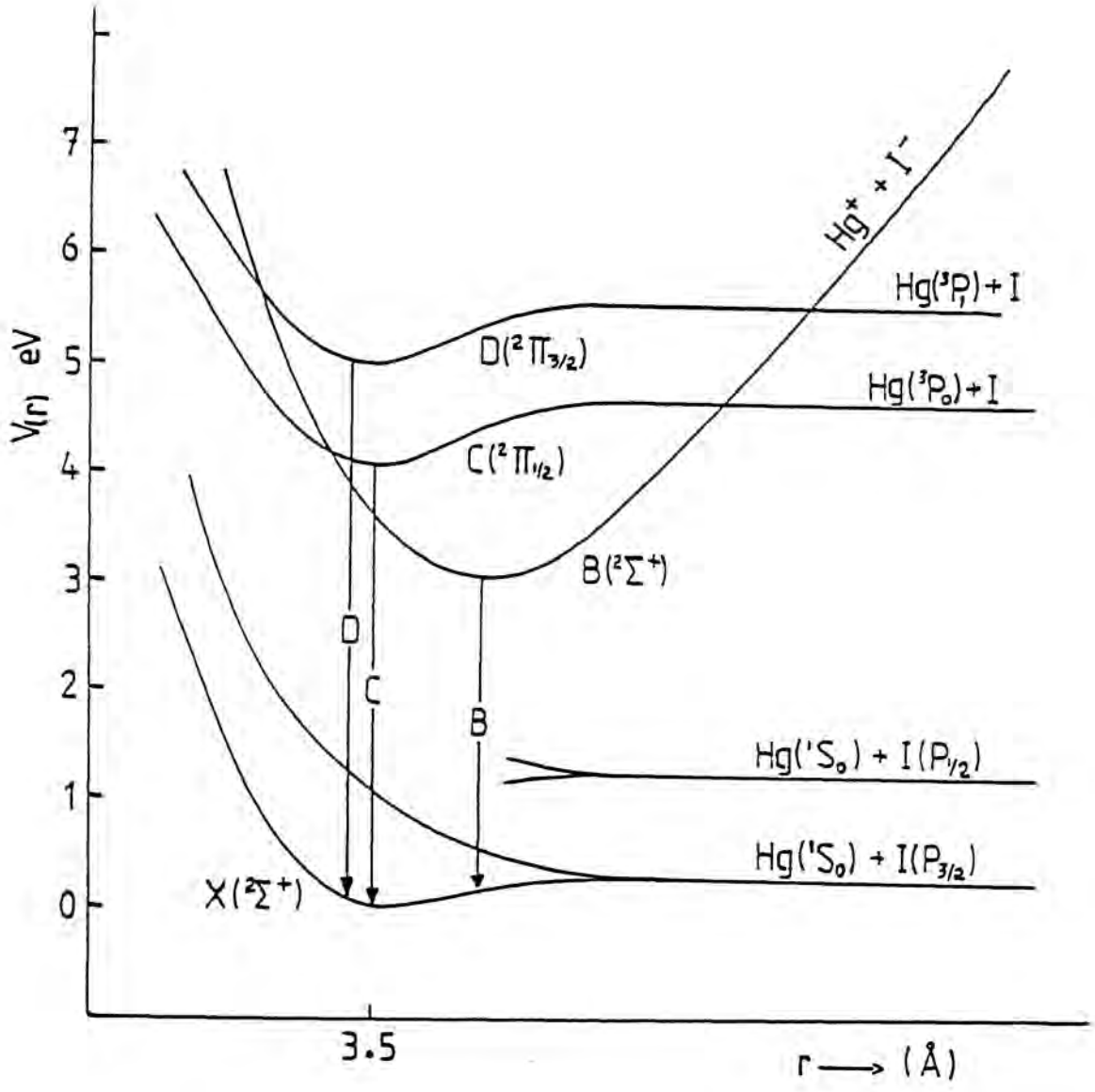
b) Wieland's observations are in error. Wieland used an unfiltered magnesium arc as his source of 173.5 nm radiation. However, it is likely that shorter wavelength emission lines were present in the stimulating radiation. For example Wieland was able to stimulate the $HgI(C \rightarrow X)$ fluorescence using the 202.6 nm emission line of the zinc arc. However, this process

is energetically impossible, suggesting the presence of shorter wavelengths in the excitation spectrum.

c) Quenching of the $HgI^*(D)$ state. During the course of the present experiment it was found that addition of small concentrations of argon gas in the photodissociation cell resulted in a dramatic reduction of the HgI(C $\rightarrow$ X) emission. At the same time the HgI(B $\rightarrow$ X) emission increased significantly. Although the presence of a small amount of argon gas may change the dissociation pattern of the trimer, a more acceptable explanation is the quenching of the $HgI^*(C)$ state to the $HgI^*(B)$ state[135]. Similarly, quenching of the $HgI^*(D)$ state can account for the absence of any HgI(D $\rightarrow$ X) emission.

Figure 35 shows a simplified arrangement of the HgI radical energy levels, which can qualitatively explain the quenching behaviour of the excited states. Known spectroscopic details, such as the binding energies of the various states, have been used to construct the figure. States D, C and X are covalent in nature and are expected to have similar shapes, but shifted vertically along the energy axis. The HgI(B) state is ionic in character and has a much larger binding energy. This causes its potential minimum to occur at a much larger interatomic distance. Curve crossings can, therefore, be expected between state B and states C and D, as indicated in figure 35. Thus predissociation of states C and D to state B is to be expected. The overlap between the vibrational levels of the three states will give rise to an equilibrium between their relative populations. However, addition of argon is expected to cause the vibrational relaxation of the states thus accomplishing the efficient quenching of states C and D.

Figure 36 shows the spectral profile of the HgI (B $\rightarrow$ X)



ENERGY LEVELS OF HgI

FIGURE 35

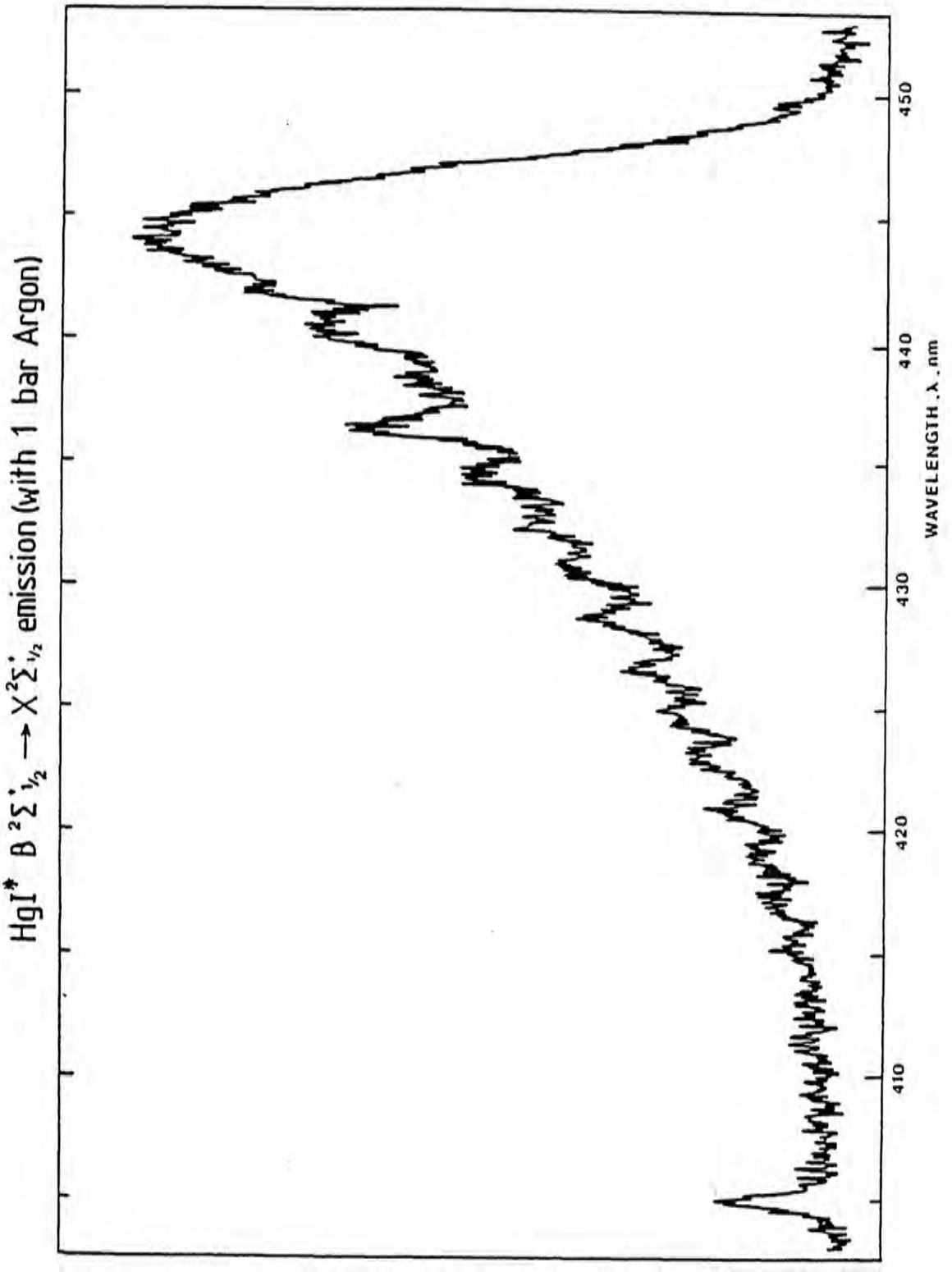

HgI* B ²Σ'½ → X²Σ'½ emission (with 1 bar Argon)
410
420
430
440
450
WAVELENGTH, λ, nm

FIGURE 36

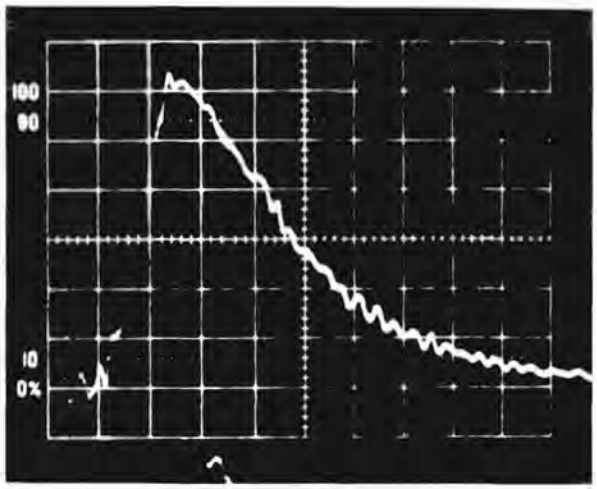
emission in the presence of 1 bar of argon. The presence of argon causes the vibrational relaxation of the $HgI^*(B)$ state, so structure can be resolved in the emission spectra due to transitions from the lowest vibrational level of the upper state to a large number of vibrational levels of the ground state. In the absence of argon, more vibrational levels of the upper state are populated and emission to different vibrational levels of the ground state overlap, giving rise to a fluorescence spectrum that appears continuous.

Plate 8(a) shows the temporal profile of the $HgI(B \rightarrow X)$ fluorescence, excited by the photodissociation of HgI_2 vapour by 172 nm radiation at a cell temperature of 373 K. The intensity of the fluorescence can be seen to decay exponentially for over an order of magnitude change in intensity. The decay constant was measured for different pressures of argon buffer gas present in the photodissociation cell. Figure 37 shows the variation of the decay constant with the argon number density. The graph is a straight line suggesting that the three body quenching rate is negligible for pressures of argon up to 1 bar. From the gradient of the plot a value of 1.45×10^{-13} ($\pm$10%) $cm^3\ s^{-1}$ was calculated for the two body quenching rate of $HgI^*(B)$ state by atomic argon. By extrapolating to zero concentration of argon a value of 24.1 ($\pm$10%) ns was calculated for the radiative lifetime of the $HgI(B \rightarrow X)$ transition.

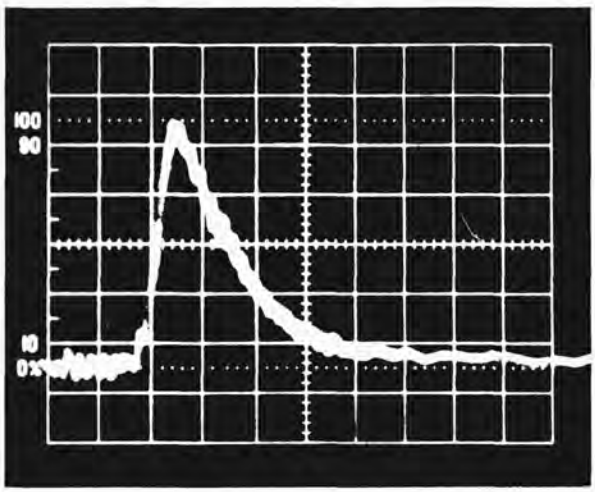
The procedure was repeated using xenon as the quenching agent. Figure 38 shows the Stern-Volmer plot for the quenching of $HgI^*(B)$ state by xenon. From the gradient of the plot, a two body quenching constant of 6.8×10^{-13} ($\pm$10%) $cm^3\ s^{-1}$ was calculated. A radiative lifetime of 24.3 ($\pm$10%) ns was estimated from the zero xenon population density intercept of

Plate 8(a) Temporal profile of the HgI(B → X) emission excited by the photodissociation of HgI_2 vapour by 172 nm radiation, 10 ns/div.

Plate 8(b) Temporal profile of the HgCl(B → X) emission when the excited vapour was enclosed in an optical cavity, 10 ns/div.



(a)



(b)

PLATE 8

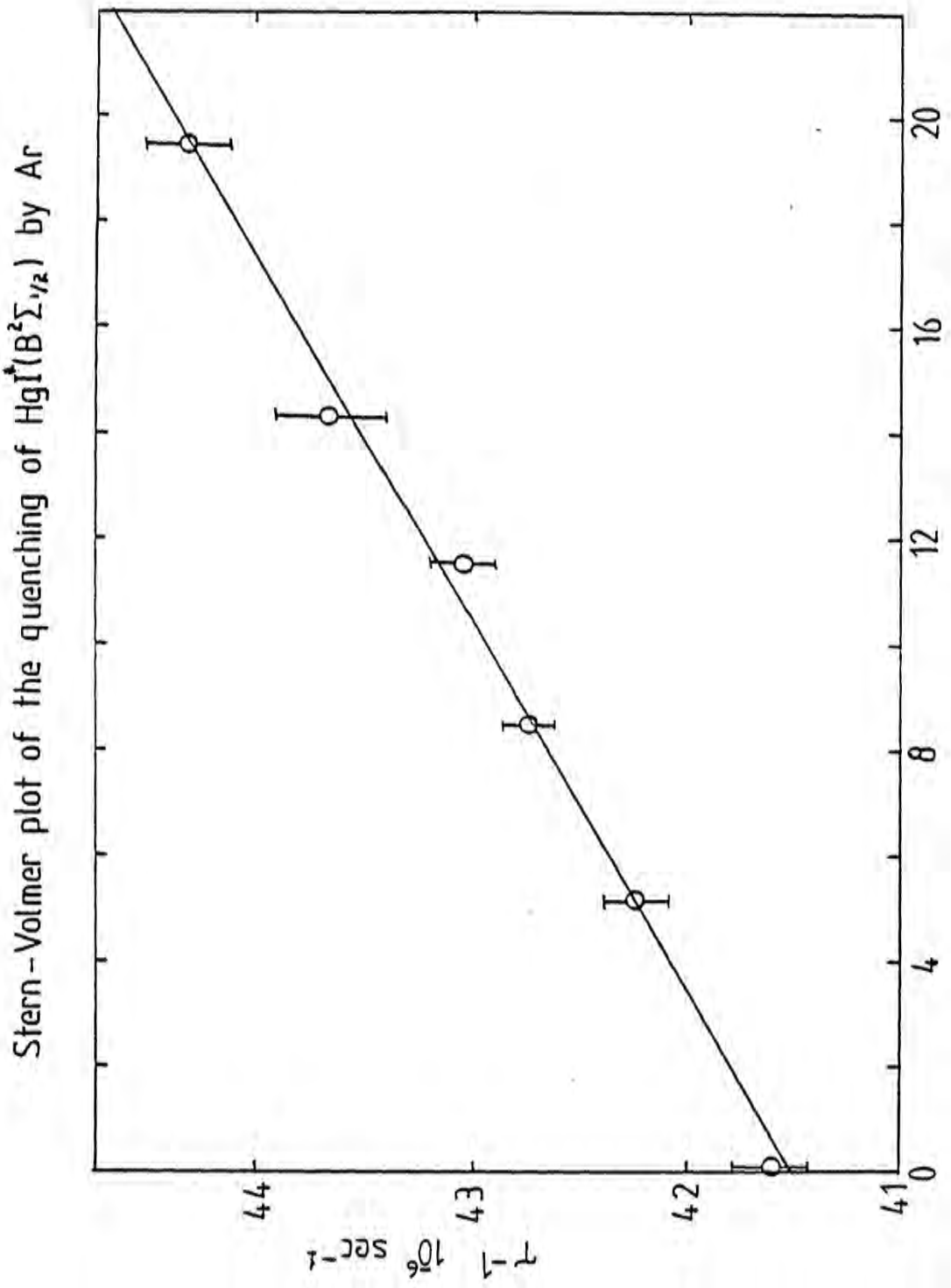

Stern-Volmer plot of the quenching of $HgI^*(B^2\Sigma_{1/2})$ by Ar
τ^{-1} 10^6 sec^{-1}
44
43
42
41
0
4
8
12
16
20
[Ar] 10^{18} cm^{-3}

FIGURE 37

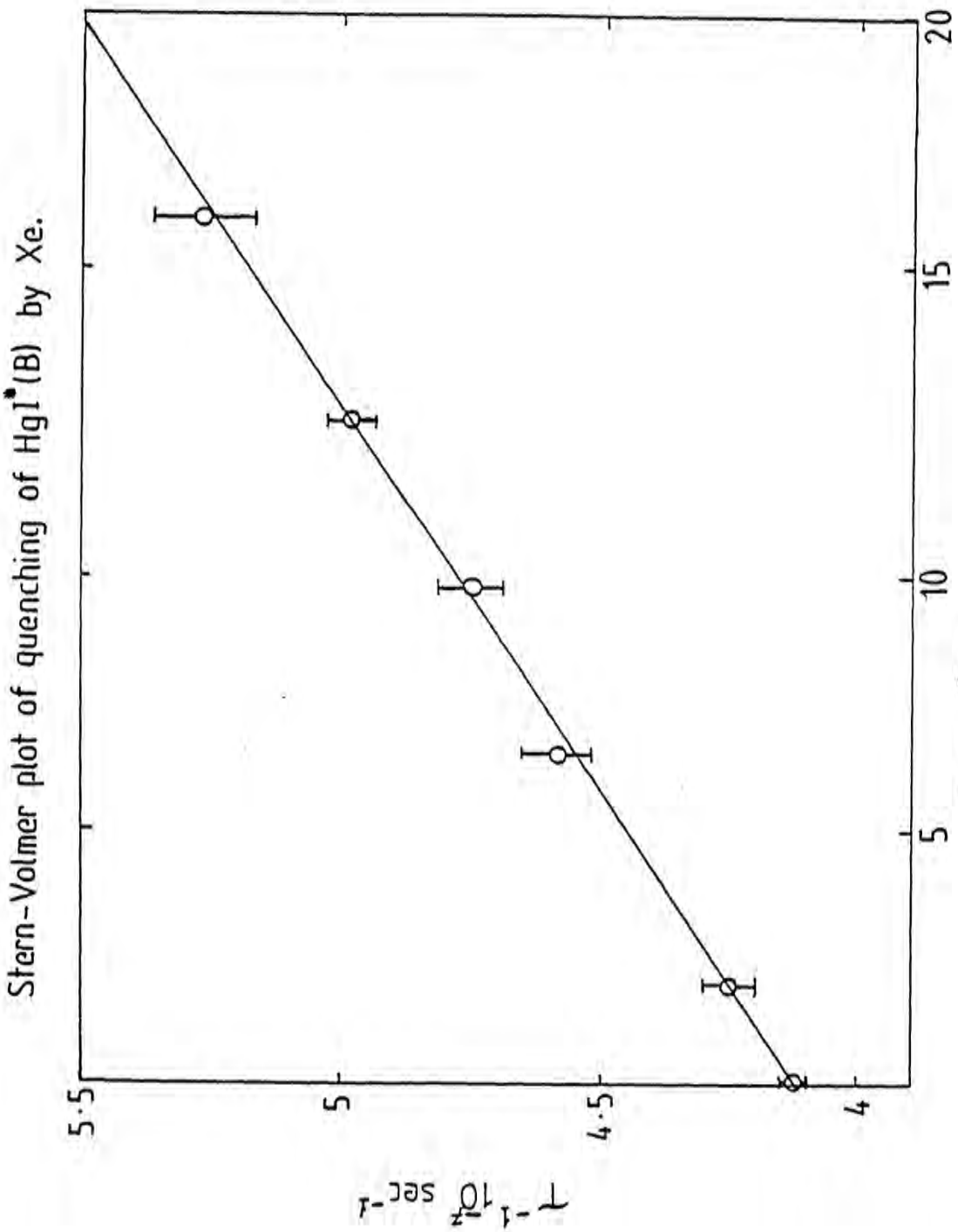

Stern-Volmer plot of quenching of HgI*(B) by Xe.
$\tau^{-1}10^{-7}$ sec^{-1}
5·5
5
4·5
4
5
10
15
20
[Xe] 10^{18} cm^{-3}

FIGURE 38

the graph. This value agrees well with the value of the lifetime estimated from figure 37.

5.6.2 Studies in $HgBr_2$

Photodissociation of $HgBr_2$ vapour using 172 nm radiation gave rise to an emission band extending to the short wavelength side of 500 nm. This was identified with the HgBr (B → X) emission band. Its time integrated spectrum in the presence of one atmosphere of argon buffer gas, is shown in figure 39. All the observed features of the band were found to originate from transitions from the lowest vibrational level of the upper state, thus indicating that 1 bar of argon was sufficient to accomplish the vibrational relaxation of the $HgBr^*(B)$ state. Failure to detect the HgBr(C → X) emission confirmed that the 172 nm photons are not energetic enough to populate the $HgBr^*(C)$ state, in agreement with the observations of Wieland[119].

Rapid formation of the $HgBr^*(B)$ state was achieved by operating at an oven temperature of 373 K. The HgBr(B → X) emission was monitored for different argon partial pressures present in the photodissociation cell. By fitting the decaying portion of each waveform to a single exponential, the fluorescence decay constants were measured at different pressures of argon. Figure 40 shows the variation of the decay constant with the concentration of argon. From its slope, the two body quenching rate of $HgBr^*(B)$ state by argon was determined to be 1.1×10^{-13} ($\pm 10\%$) $cm^3\ s^{-1}$. From the intersection of the graph with the zero argon concentration axis, the value of the HgBr(B → X) radiative lifetime was measured to be 23.2 ($\pm 8\%$) ns.

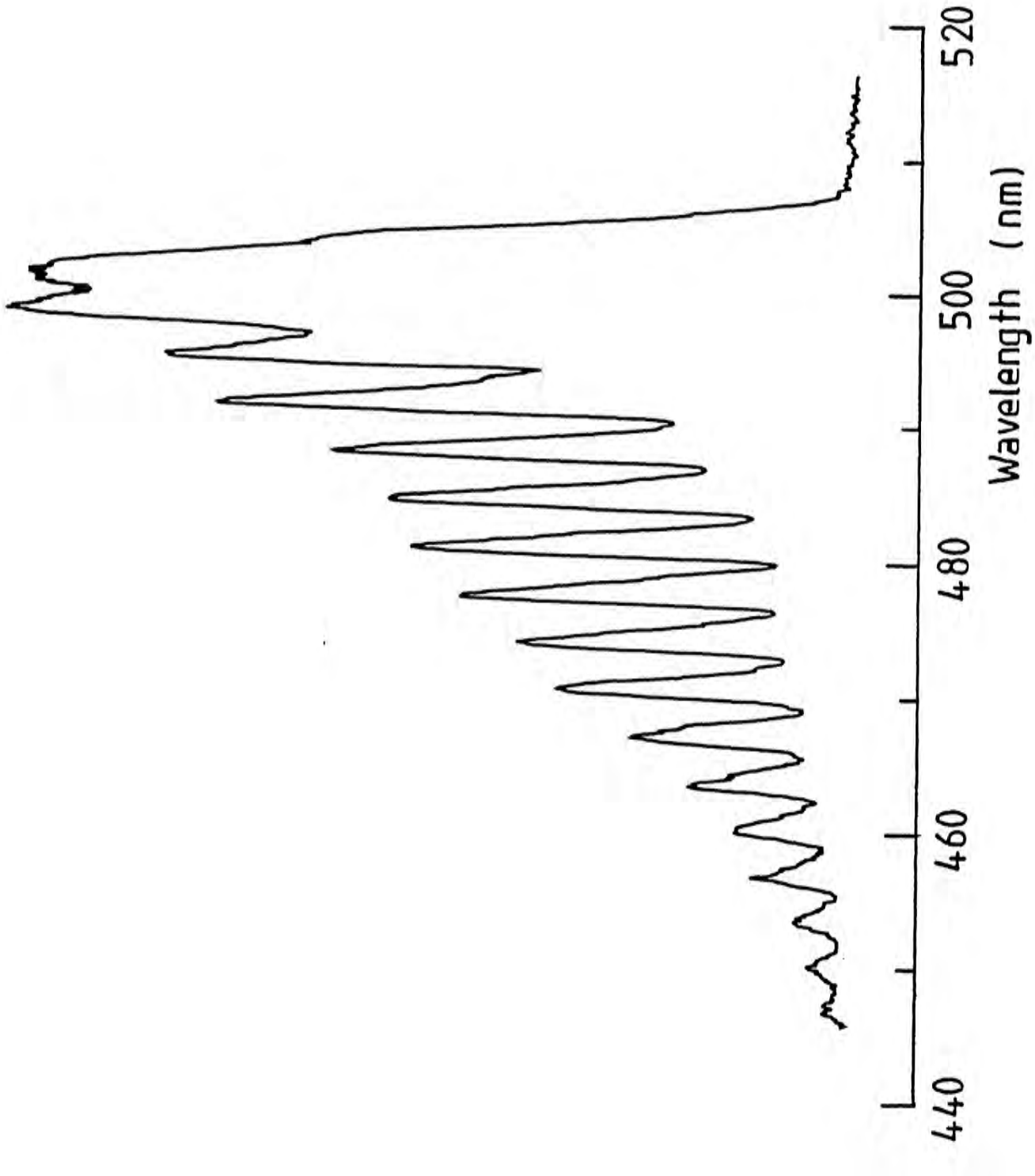
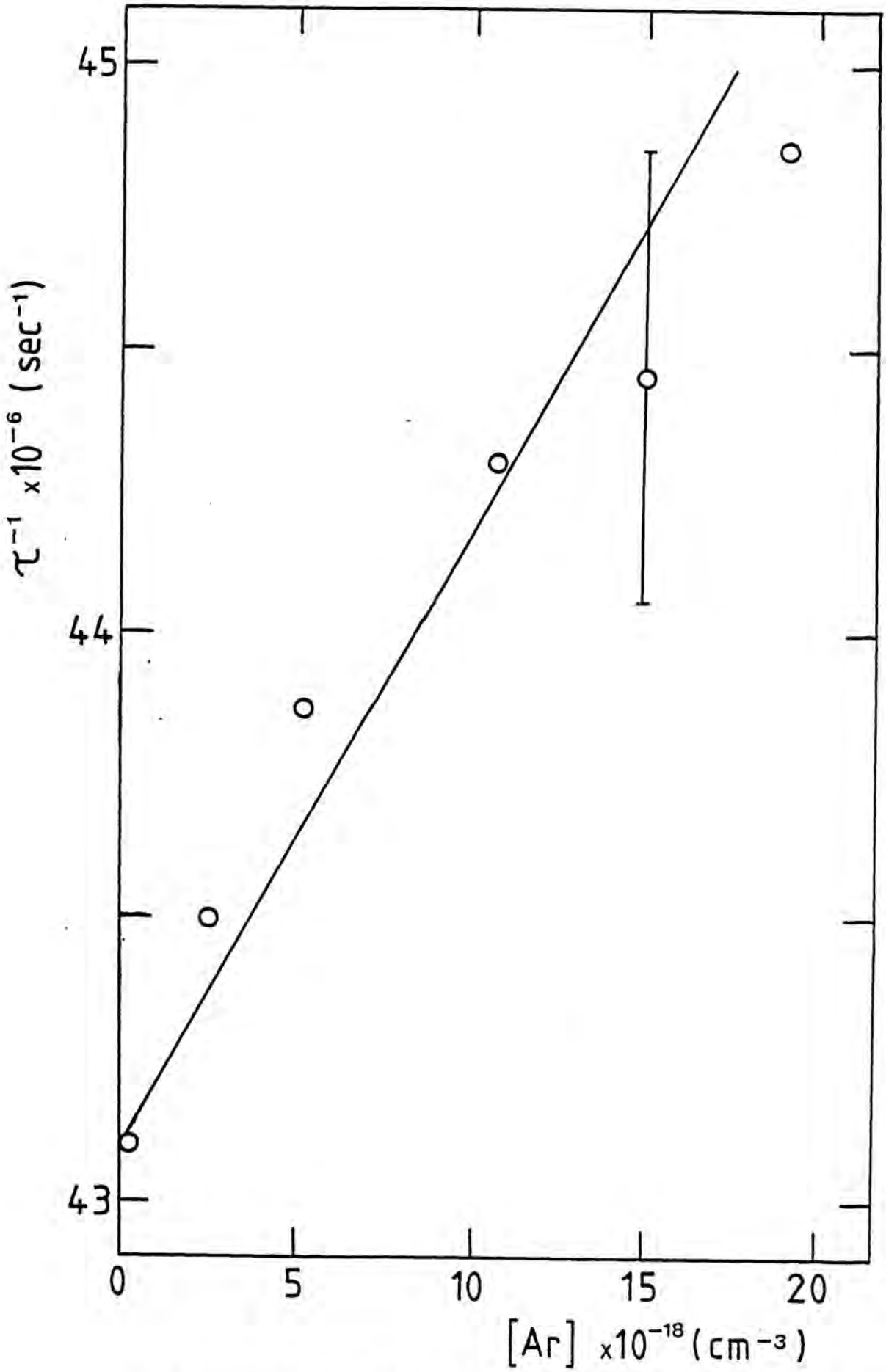


FIGURE 39



QUENCHING OF $HgBr^{*}(B^{2}\Sigma_{1/2})$ BY ARGON

FIGURE 40

5.6.3 Studies in $HgCl_2$

The absorption spectrum of a column of $HgCl_2$ vapour, 20 cm long, was recorded for an oven temperature of 350 K in the wavelength range 169 to 175 nm. This is shown in figure 41. Four absorption bands are resolved, in agreement with the observations of Wieland[119] and Wehrli[136]. All these bands have been assigned[137] to transitions originating from the lowest vibrational level of the ground state, indicating little population of higher vibrational levels. At oven temperatures of 400 K the absorption spectrum became continuous and no structure could be resolved.

Figure 42 shows the spectrum of the HgCl(B → X) emission in the presence of 400 Torr of argon. All the observed bands originate from the lowest vibrational level of the upper state. The existence of two chlorine isotopes, Cl^{35} and Cl^{37}, gives rise to two sets of bands. However, owing to the lower abundance of the Cl^{37} isotope, bands due to $HgCl^{37}$ can just be observed[129].

The temporal profile of the HgCl(B → X) emission was studied at different concentrations of argon up to 400 Torr. Figure 43 shows the variation of the fluorescence intensity decay constant, with the concentration of argon buffer gas. The slope measured from the graph of figure 43 gives a value of 4.5×10^{-14} (±10%) $cm^3\ s^{-1}$ for the two body quenching rate of $HgCl^*(B)$ state by argon. From the zero argon density intercept, a value of 22.0 (±8%) ns was calculated for the radiative lifetime of HgCl(B → X) transition.

The HgCl(B → X) fluorescence was observed to decay with a time constant in the region of 22ns. However, by increasing

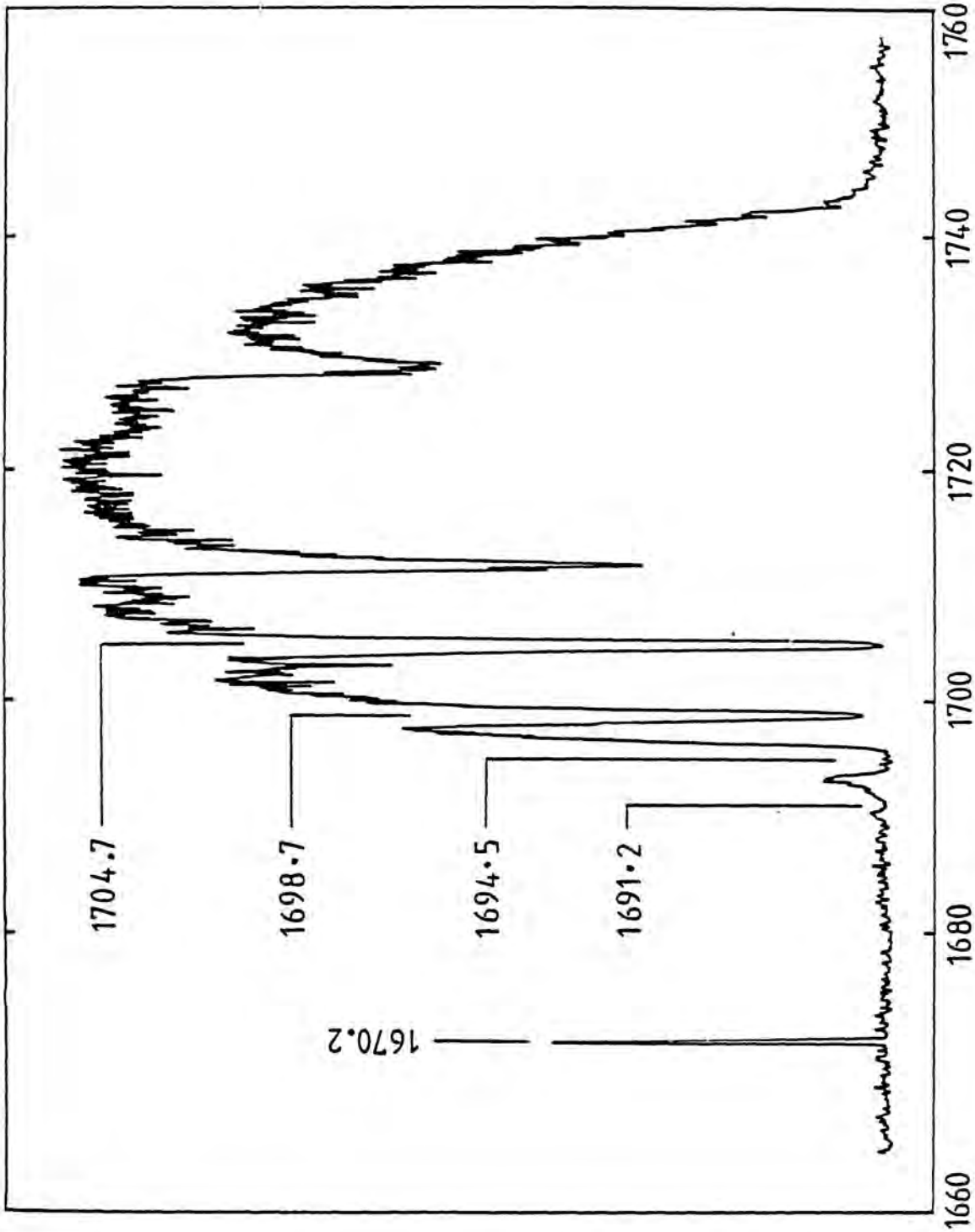


FIGURE 41

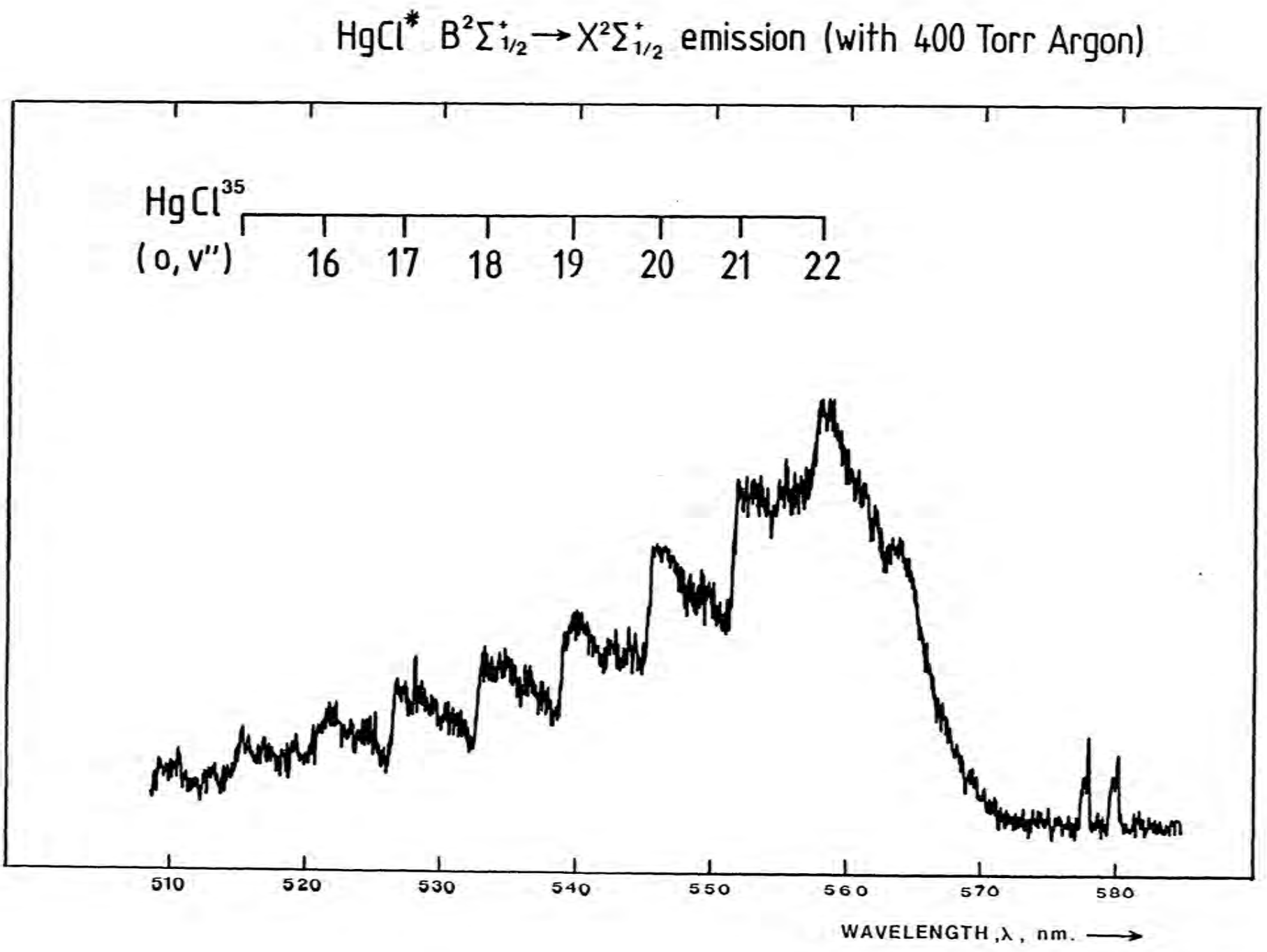

HgCl* B²Σ+1/2 → X²Σ+1/2 emission (with 400 Torr Argon)
HgCl35
(o, v'')
16
17
18
19
20
21
22
510
520
530
540
550
560
570
580
WAVELENGTH, λ, nm.

FIGURE 42

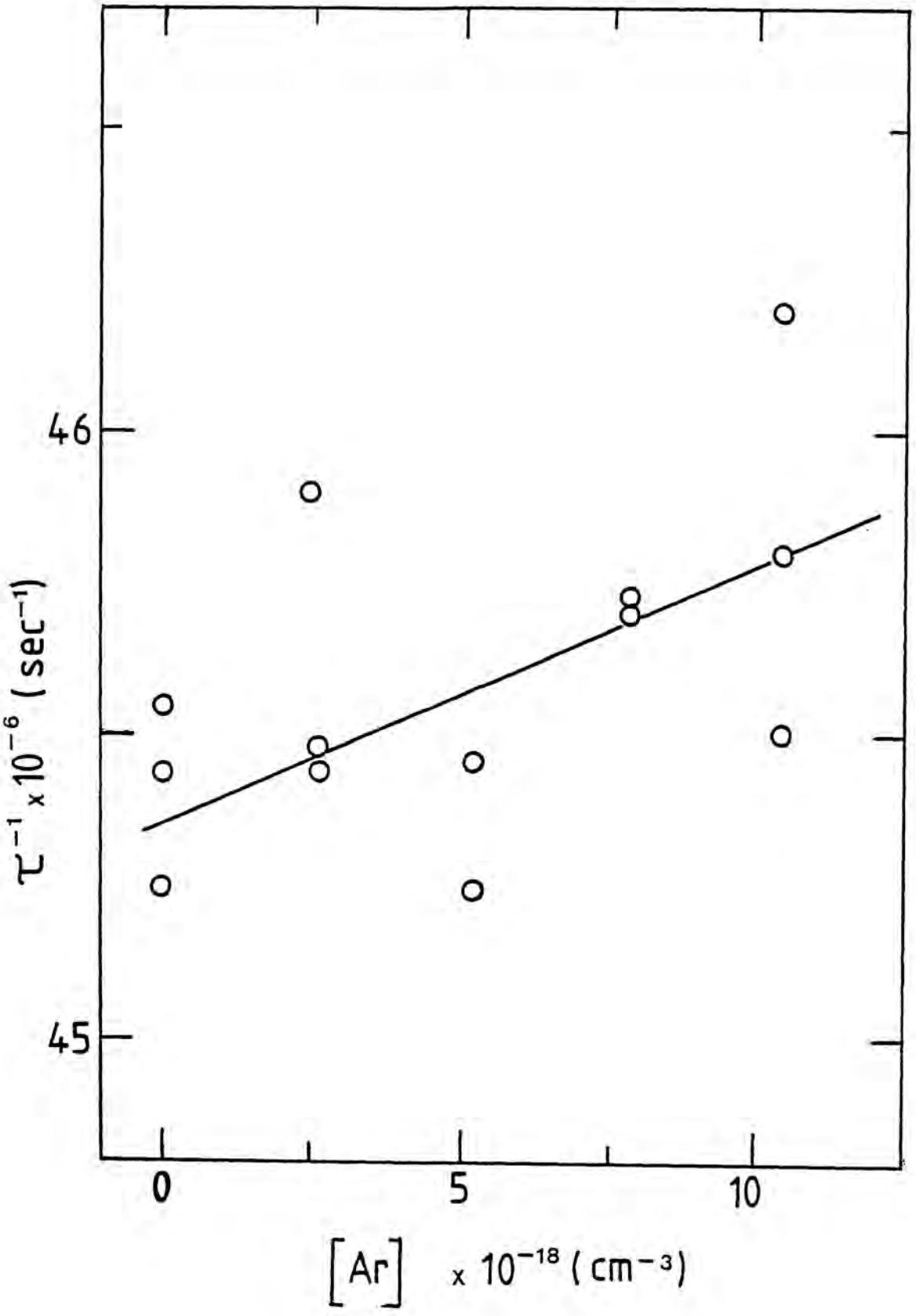


FIGURE 43

the vapour pressure of $HgCl_2$ so that complete absorption of the xenon laser pulse was taking place and enclosing the excited medium in a cavity, the decay constant was observed to decrease down to ~10 ns. The cavity consisted of a stainless steel flat, polished to optical flatness, with a 6 mm aperture to allow the xenon laser radiation to enter the cavity. A 90% aluminium mirror with a flat glass substrate was used to complete the cavity. The intra-cavity flux was monitored through the 90% reflector, using an S5 photodiode, viewing through a narrow band filter. Plate 8(b) shows the observed signal. The change in shape of the output signal was taken as an indication of lasing although no spectral observations of the output were performed. Stimulated emission on the HgCl(B $\rightarrow$ X) transition has also been reported by Eden[111] using the xenon excimer fluorescence to photodissociate $HgCl_2$ and excite the upper state.

5.6.4 Photodissociation studies in HgX_2 solutions

One of the practical advantages of working with the mercuric halides is their high volatility. However, temperatures in excess of 400 K are required for molecular concentrations of 10^{16} cm^{-3} (ref. 130). In order to avoid using ovens, studies were performed in solutions of the mercuric halides in water and acetonitrile. Published data[138] indicate that the absorption cross section of solutions of the mercuric halides in acetonitrile exhibits the same features as the absorption cross section of the salts in the vapour phase. Furthermore it has been reported[139,140] that longer wavelengths are effective in stimulating the visible fluorescence of the HgX radical in

aqueous solution than those required to excite the salts in the vapour phase.

A small quartz cell with a 2 mm thick CaF_2 window was constructed and attached to the system so that the xenon laser output could enter the cell through the CaF_2 window. The cell was filled with 7.5×10^{-5} Molar aqueous solution of $HgCl_2$. No HgCl(B $\rightarrow$ X) emission was observed when the solution was excited with 172 nm radiation. A similar solution of $HgBr_2$ was subsequently excited with the 193 nm output of an ArF excimer laser[141] but no HgBr(B $\rightarrow$ X) emission was observed, even though it was checked that the presence of disolved $HgBr_2$ salt had caused the total absorption of the 193 nm radiation.

Similar results were obtained when acetonitrile was used as the solvent. These observations appear to be in conflict with previous reports[139], but the absence of any fluorescence from the solutions was not surprising since the effects of the solvent is to prevent the complete separation of the dissociation fragments[142].

5.7 Discussion

The major source of error in the measurement of the quenching rates and radiative lifetimes was the uncertainty in measuring the fluorescence intensity I(t) at a particular time t from the oscilloscope trace. The zero level fluorescence intensity was defined by triggering the oscilloscope without firing the xenon laser. However, as time increased the uncertainty in measuring I(t) also increased, partly due to the finite thickness of the oscilloscope traces. Using the early part of the pulse, errors were limited to $\pm$5%. The error

introduced in the measurement of the pressure of the quenching gas was less than 2%.

The quenching rate constants determined for the $HgX^*(B)$ states are summarized in table 5.1 . The table includes recently published values of the rates for comparison. The results of the present experiment are in good agreement with the values reported by Roxlo[135] and Mandl[143,144], except for the quenching rate of the $HgI^*(B)$ state by xenon, which is a factor of three higher than the value estimated by Roxlo[135]. Roxlo[135] and Mandl[145] used a xenon flashlamp to excite the $HgX^*(B)$ states and a modified theory was needed to account for the quasi-C.W. excitation of the upper states. Interpretation of their results required the knowledge of the radiative lifetimes of the $HgX^*(B)$ states.

A summary of the values of the radiative lifetimes of the $HgX(B \rightarrow X)$ transitions is given in table 5.2 . Values of the lifetimes available in the literature are also included for comparison. There is good agreement between the lifetimes of $HgCl(B \rightarrow X)$ and $HgBr(B \rightarrow X)$ transitions estimated here and those reported by Eden[111], Weynant[146] and Djeu[147]. However, the value obtained for the $HgI(B \rightarrow X)$ lifetime is approximately 12% smaller than the value of Waynant[146], whereas the theoretically calculated values of Duzy and Hyman[134] are considerably shorter than those estimated from experimental measurements.

Most of the emphasis in the determination of the quenching rate constants of the $HgX^*(B)$ states has been devoted to the rates due to the ground state triatomic molecule, HgX_2[111,146]. However, it was shown in the course of this work that the use of a high power photolysis source can destroy the parent molecule so fast that the quenching of the photodissociation

TABLE 5.1

Summary of the quenching rates constants for HgX ($B^2\Sigma^+_{1/2}$) state for Argon and Xenon (Units cm^3sec^{-1})

	Present work		Roxlo et al. (135)		Mandl et al. (143)	Mandl et al. (144)
	ARGON	XENON	ARGON	XENON	ARGON	ARGON
$HgI^*(B^2\Sigma^+_{1/2})$	1.45×10^{-13}	6.8×10^{-13}	1.1×10^{-13}	2.2×10^{-13}		
$HgBr^*(B^2\Sigma^+_{1/2})$	1.1×10^{-13}		7.2×10^{-14}			
$HgCl^*(B^2\Sigma^+_{1/2})$	4.5×10^{-14}				$<10^{-13}$	5×10^{-14}

TABLE 5.2

SUMMARY OF THE HgX ($B^2\Sigma^+_{1/2} \longrightarrow X^2\Sigma^+_{1/2}$) RADIATIVE LIFETIMES

	Present work	Djeu et al (147)	Eden (111)	Waynant (146)	Duzy et al. (134)
HgI (B→X)	24.2ns			27.3ns	12ns
HgBr(B→X)	23.2ns	23.25ns		23.7ns	16ns
HgCl(B→X)	22ns		22.2ns		20ns

products by the parent molecules can be neglected.

In conclusion, short pulse excitation of the $HgX^*(B)$ state by the photodissociation of the triatomic HgX_2 , in the presence of a buffer gas has been used to measure the quenching rate constants of the HgX(B) states by argon and xenon, as well as calculate the radiative lifetimes of the HgX(B $\rightarrow$ X) transitions. Accurate knowledge of these quantities is useful for the understanding of the kinetics and for optimizing the performance of the mercury halide lasers. The use of optical excitation to populate the $HgX^*(B)$ state is ideal since it avoids any complications which might be introduced by the presence of electrons.

CHAPTER 6

CONCLUSIONS-SUGGESTIONS FOR FURTHER WORK

The availability of practical laser sources, together with the experimental difficulties associated with the VUV has limited photodissociation studies to wavelengths longer than 190 nm. However, most of the dissociation continua of small molecules lie in the VUV.

In this thesis the characteristics of the xenon excimer laser were studied. It was shown that the coaxial pumping geometry, employed in the excitation of the high pressure gas, allowed the rapid and convenient change of the power density deposited in the gas, while maintaining uniform excitation throughout the high pressure gas. The ability to alter the pumping power density was shown to be important in optimizing the performance of the xenon laser.

Optimum energy output was obtained using a 6 mm diameter anode tube, in combination with a cavity consisting of a high reflectivity (> 97%) dielectric mirror and a single plate spectrasil etalon. Using this arrangement, pulses with energy in excess of 30 mJ were obtained, with very little damage to optical components.

The spectral bandwidth of the laser was narrowed by introducing a dispersive element inside the cavity. Using an aluminium coated 1200 lines mm^{-1} diffraction grating, a x2 spectral narrowing was observed, when the cavity was tuned to the middle of the tuning range. Using a 3600 lines mm^{-1} grating, the bandwidth of the spectral output was reduced to $\sim$0.25 nm over the entire tuning range. Reliable tuning was

also observed when a spectrasil prism, or a BaF_2 prism, or two spectrasil prisms were inserted in the cavity. The laser output was found to be continuously tunable in the wavelength range 169 to 175 nm.

Examination of the temporal profile of the tuned laser indicated that the most important parameter determining the efficiency of the tuning was the build up time of the intra-cavity flux. This, in turn, was shown to depend on the gain provided by the excited medium at the resonant wavelength and on the value of the quality factor, Q of the cavity. Tuning could be achieved in a region of low gain with a cavity of low Q provided the gain can be maintained for a long enough period, so that the intra-cavity flux could rise above the noise level.

The spectral bandwidth of the tuned output was shown to be dependent on the laser pulse energy. A narrow spectral output was obtained when the laser was operated in a regime, just above threshold.

The xenon excimer laser can provide high power tunable radiation, with photon energy in excess of 7 eV and is therefore ideal for photodissociation studies. The laser was shown to be capable of photodissociating the OCSe molecule, producing the excited state $Se(^1S)$. The 172 nm photon is energetic enough to photoionize the $Se(^1S)$ state. A simple ionization detector was constructed and the photoionization cross section of $Se(^1S)$ was measured in the region 170 to 175 nm. A value of 0.8×10^{-16} cm^2 was also measured for the photodissociation cross section of OCSe by 172 nm radiation. Observation of the chemiluminescence from the excited medium allowed a value of 1.6 to be estimated for the refractive index of BaF_2 at 172 nm.

The xenon excimer laser was used to measure the photoionization cross section of ground state atomic caesium in the VUV. A value of 0.9×10^{-19} cm^2 was measured at 172 nm. This value appears to substantiate the theoretical predictions of Weisheit.

The xenon laser was also shown to be capable of exciting the $HgX^*(B)$ state, (X=I,Br,Cl) by the photodissociation of the HgX_2 molecule. In the case of the mercuric iodide, the $HgI(C \rightarrow X)$ emission was observed, indicating the population of the $HgI^*(C)$ state.

The use of a high power excitation source enabled the effective excitation time of the medium to be considerably shorter than the duration of the pumping pulse. Monitoring the temporal profile of the $HgX(B \rightarrow X)$ fluorescence intensity in the presence of argon gas, enabled the measurement of the quenching rate constants of the $HgX^*(B)$ states by argon. The radiative lifetimes of the $HgX(B \rightarrow X)$ transitions were also estimated.

Excitation sources used in early photodissociation studies consisted of metal lines emitted from sparks, or the emission of different discharge lamps. However, the developement of high power UV lasers opened new dimensions in photodissociation studies. In particular, the availability of the rare gas halide lasers provided powerfull photodissociation sources down to 193 nm. This is a convenient wavelength, since the photon energy is relatively high ($\sim$ 6.4 eV), whereas atmospheric absorption is low, so that no vacuum paths are required for the transport of the laser output.

The ArF laser was shown to be capable of exciting the $HgBr(B \rightarrow X)$ and $HgI(B \rightarrow X)$ fluorescence by the photodissociation

of the triatomic molecule. However, wavelengths below 181 nm are required for the excitation of the $HgCl^*(B)$ state. It was shown in chapter 5 that the xenon excimer laser can excite the HgX(B → X) fluorescence of all three radicals, due to the higher photon energy at 172 nm. The xenon excimer laser can therefore complement the rare gas halides and extend dissociation studies using high power radiation in the VUV.

Photodissociation of the alkali halides has been used to produce excited state alkali atoms[148], known as superalkali atoms. This process is very efficient because the ground state of the alkali halide molecules is strongly bound by ionic attraction, whereas the excited states are all repulsive, except for shallow minima that occur for separations much larger than the position of the ground state minimum. In alkali atoms the low lying excited states are coupled to the ground state by strongly allowed transitions. Using the photodissociative excitation of alkali metal atoms, alkali atom resonance line superfluorescence lasers have been produced[149,150]. However, the photolysis radiation photon energy limits the number of states that can be populated. Using 193 nm radiation to photodissociate CsI vapour, atomic states up to Cs(8s) can be populated. Using the output from the xenon excimer laser, caesium states near the ionization limit can be produced. Moving progressively to CsBr, CsCl and CsF, the 172 nm radiation can populate the states Cs(8p), Cs(7p) and Cs(5d) respectively.

Similar behaviour is exhibited by group IIIa metal halides[151,152]. During the course of this work, lasing was observed on the indium $6S_{\frac{1}{2}} \rightarrow 5P$ transition at 451.1 nm. The upper state was produced by the photodissociation of InI_3

by 172 nm radiation.

Excimer lasers suffer from poor beam quality due to the small number of cavity round trips that can take place in 10 ns, the duration of lasing. In experiments involving non-linear optics, however, good beam quality and narrow spectral bandwidths are required[153]. There exists a method that will allow even the fluorescence from a fast source to be used in wavelength up-conversion experiments. Photodissociation can be used to generate large densities of atomic excited states, which will allow the wavelength shift of other lasers by stimulated Raman upconversion.

Assume the use of a poor beam quality laser in the photo-dissociation of a gas. Provided the laser beam flux is much higher than the saturation flux for the photodissociation of the medium, complete decomposition of the parent molecules will occur. What is more important, non-uniformities in the photo-lysis radiation beam will appear as different penetration depths in the photodissociation cell, whereas the excited photofragments will have a uniform distribution. Furthermore, the spectral bandwidth of the photolysis radiation is only limited by the production of a single dissociation product and can be as broad as many thousand cm^{-1}.

The excited state dissociation products can be used to Raman-upconvert a second laser of better beam quality. Two reports exist in the literature, where such a process has been attempted. In the first[154], a flashlamp was used to photodisso-ciate trifluoromethyliodide (CF_3I), producing excited state iodine, $I(P_{\frac{1}{2}})$. Gain was observed at 588.4 nm when the disso-ciation products were pumped with a Nd : Yag laser operating at 1.06 um.

In a more recent experiment[155], the 4th harmonic of a Nd : Yag laser was used to photodissociate TlBr vapour, in order to populate the Tl($6p^2P_{3/2}$) metastable. However, no Raman upconversion was possible, since the photodissociation of TlBr at 266 nm favours the production of Tl($6p^2P_{\frac{1}{2}}$) ground state. It is therefore important to use a photodissociation process that produces the excited state with high quantum yield.

It was shown in chapter 3 that the xenon excimer laser can excite the Se(^1S) metastable state by the photodissociation of OCSe. The quantum yield has been measured to be unity[72,73]. The Se(^1S) metastable state can therefore be employed in Raman upconversion experiments and add 1.6 or 2.5 eV to the energy of the pump laser photon.

APPENDIX A

The etching of the anode tubes

Anode tubes of approximately 30 μm wall thickness were required, in order to allow maximum transmission of the E-beam electrons with a minimum loss of energy. Stainless steel tubes can be obtained commercially with a 150 μm wall thickness. Reduction of the wall thickness can be achieved by chemically etching the tube to the desired thickness. The etching solution consisted of 33% nitric acid, 10% hydrochloric acid and the remainder being water. The actual etching was done by the hydrochloric acid. The nitric acid was acting as a catalyst.

Chemical etching was found to be unreliable, because the rate of etching was found to increase with increasing temperature of the etching solution. The etching reaction was itself exothermic and this could lead to a runaway process. On average only one tube in three was successfully etched. Furthermore the etched surface had a very rough finish.

Electropolishing is a process used by metallurgists to prepare metal samples to be examined in electron microscopes. It is the inverse process of electroplating and was used as an alternative method of etching the anode tubes.

The tube to be polished was made the anode, in an electrolysis process in which the electrolyte consisted of 10% orthophosphoric acid, 10% sulphuric acid, 20% water and 60% glycerol. Glycerol was used to reduce the mobility of the charge carriers, thus increasing the etching period and allowing more control during the etching process. In order to achieve uniform etching, cylindrical symmetry had to be employed. A 50 cm long glass

tube of 6 cm internal diameter, was used to contain the electrolyte. The cathode was made in the form of a coaxial cylinder, out of stainless steel mesh. The tube to be etched was positioned along the axis of the system, as shown in figure A1. The part of the tube that was to be etched was defined by masking the rest of the tube by painting it with nail varnish, obtainable from the local chemist shop. However, higher rates of etching were observed at the interface of the nail varnish and the etched part of the tube.

In an improved design, the unetched parts of the tube were inserted in perspex tube. The internal diameter of the perspex tube was deliberately kept large ($\sim$1cm) so that etching could be extended slightly into the perspex tube, thus allowing a uniform transition between the etched and unetched parts of the tube. The transition was so smooth that it could not be visually distinguished.

A 4 Ampere D.C. current was passed through the system. Every 15 minutes the circuit was broken and the tube was washed thoroughly to remove the black deposit that appeared on the surface. This was thought to be nickel oxide, from the nickel content of the stainless steel. The thickness of the anode tube was monitored at different points along its length. In order to remove any effects due to the asymmetry in the etching geometry, the tube was rotated every 15 minutes. Using this method, tubes could be etched down to 25 μm. A 10% tolerance, quoted by the manufacturers in the thickness of the unetched tube, appeared to be the only limit in the eventual wall thickness that could be achieved.

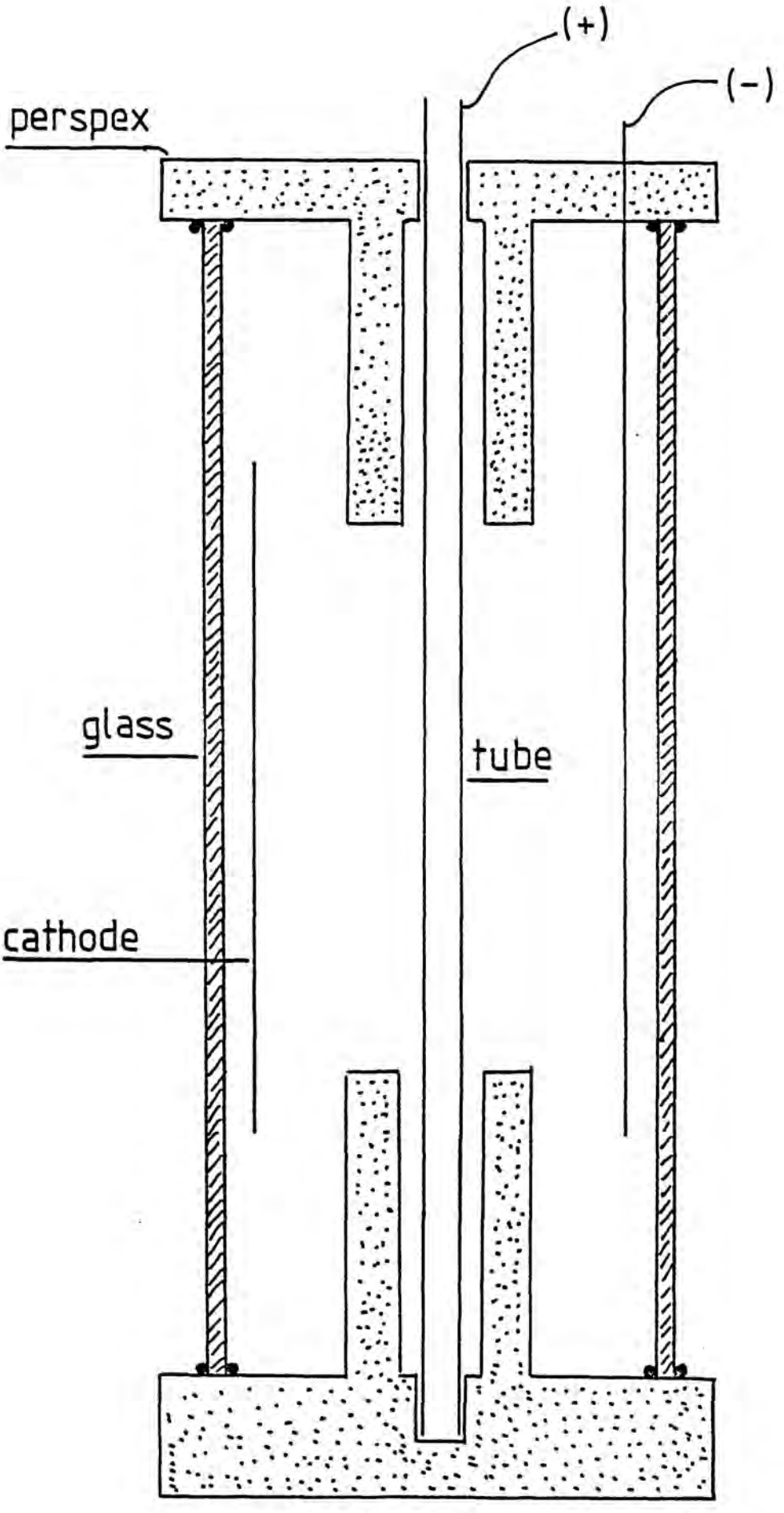


FIGURE A1

REFERENCES

1. CALVERT, J.G., PITTS, J.N.
   Photochemistry. Published by John Wiley and Sons
2. HERZBERG, G.
   Spectra of Diatomic Molecules. Published by Van Nostrand Reinlhold Co., 1950
3. ROSEN, B.
   Spectroscopic Data Relative to Diatomic Molecules. Pergamon Press, Oxford 1970
4. FILSETH, S.V., WELGE, K.H.
   Journal of Chemical Physics 51, 839, 1969
5. GAYDON, A.G.
   Dissociation Energies and Spectra of Diatomic Molecules. Published by Chapman and Hall, 1968
6. SAMSON, J.A.R.
   Techniques of Vacuum Ultraviolet Spectroscopy Published by John Wiley and Sons, 1967
7. WILKINSON, P.G., TANAKA, Y.
   Journal of the Optical Society of America 45, 344, 1955
8. TANAKA, Y.
   Journal of the Optical Society of America 45, 710, 1955
9. TANAKA, Y., TURSA, A.S., LEBLANC, F,J.
   Journal of the Optical Society of America 47, 105, 1957
10. HOUTERMANS, F.G.
    Helvetica Physica Acta 33, 933, 1960
11. BASOV, N.G., DANILYCHEV, V.A., POPOV, Y.M.
    J.E.T.P. Letts. 12, 329, 1970
12. KOEHLER, H.A., FERDERBER, L.J., REDHEAD, D.L., EBERT, P.J.
    Applied Physics Letters 21, 198, 1972

13. HOFF, P.W., SWINGLE, J.C., RHODES, C.K.
Applied Physics Letters 23, 245, 1973

14. HUGHES, W.M., SHANNON, J., HUNTER, R.
Applied Physics Letters 24, 488, 1974

15. MULLIKEN, R.S.
Journal of Chemical Society of America 91, 4615, 1969

16. MULLIKEN, R.S.
Journal of Chemical Physics 52, 5170, 1970

17. BONIFIELD, T.D., RAMBOW, F.H.K., WALTERS, G.K.
Journal of Chemical Physics 72, 2914, 1980

18. WERNER, C.W., GEORGE, E.V., HOFF, P.W., RHODES, C.K.
I.E.E.E. Journal of Quantum Electronics 13, 769, 1977

19. LORENTZ, D.C.
Physica 82C, 19, 1976

20. ZAMIR, E., WERNER, C.W., LAPATOVICH, W.P., GEORGE, E.V.
Applied Physics Letters 27, 56, 1975

21. KOEHLER, L.J., FERDERBER, L.J., REDHEAD, D.L., EBERT, P.J.
Physical Review A 9, 768, 1974

22. GERARDO, J.B., JOHNSON, A.W.
Applied Physics Letters 26, 582, 1975

23. CAPBELL, J.D., CENTER, R.E.
Journal of Applied Physics 51, 2348, 1980

24. DUZY, C., BONESS, J.
I.E.E.E. Journal of Quantum Electronics 16, 640, 1980

25. GERARDO, J.B., JOHNSON, A.W.
I.E.E.E. Journal of Quantum Electronics 9, 748, 1973

26. FOURNIER, G.R.
Optics Communications 13, 385, 1975

27. WERNER, C.W., GEORGE, E.V., HOFF, P.W., RHODES, C.K.
Applied Physics Letters 25, 235, 194

28. DUZZY, C., BONESS, M.J.W.
Applied Physics Letters 35, 903, 1979

29. SMITH, D., DEAN, A.G., PLUMB, I.C.
Journal of Physics B 5, 2134, 1972

30. BARDSLEY, J.N., BIONDI, M.A.
Advances in Atomic and Molecular Physics 6, 2, 1970

31. FREEMAN, C.J., McEWAN, M.J., CLARIDGE, R.F., PHILLIPS, L.F.
Chemical Physics Letters 10, 530, 1971

32. TIMPSON, P.R., ANDERSON, J.M.
Canadian Journal of Physics 48, 1817, 1970

33. THORNTON, G., POLIAKOFF, E.D., MATTHIAS, E, SHIRLEY, D.A.
Journal of Chemical Physics 71, 133, 1979

34. JOHNSON, A.W., GERARDO, J.B.
Journal of Chemical Physics 59, 1738, 1973

35. EDWARDS, C., HUTCHINSON, M.D., MARTIN,J.C., STORR, T.H.
A.W.R.E. Aldermaston report SSWA/J.C.M./775/99, 1975

36. EDWARDS, C.B.
Ph.D. Thesis, London University, 1978

37. MARTIN, J.C.
A.W.R.E. Report SSWA/JCM/704/49

38. DAUGHERTY, J.D., MANGANO, J.A., JACOB, J.H.
Applied Physics Letters 28, 581, 1976

39. KNOP, G., PAUL, W.
Alpha, beta, gamma ray spectroscopy, Volume 1, Page 12
North Holland Publishing Co. 1965

40. ROSSI, B.
High Energy Particles. Chapter 2, Prentice Hall,
Englewood Cliffs Publishing Co. 1952

41. SMITH, R.C., SCHUMACHER, B.W.
Nuclear Instruments and Methods 118, 73, 1974

42. BRADLEY, D.J., HULL, D.R., HUTCHINSON, M.H.R., McGEOCH, M.W.
Optics Communications 11, 335, 1974

43. BRADLEY, D.J., HUTCHINSON, M.H.R., HULL, D.R., McGEOCH, M.W.
Optics Communications 14, 1, 1975

44. HULL, D.R.
Ph.D. Thesis, London University, 1976

45. HUGHES, W.M., SHANNON, J., KOLP, A., AULT, E., BHAUMIK, M.
Applied Physics Letters 23, 385, 1973

46. BRAUNSTEIN, R., OCKMAN, N.
Physical Review 134, A499, 1964

47. HUNTER, W.R.
Private communication

48. VIECELLI, J.A.
Lawrence Livermore Lab. Report UCRL 51374, 1973

49. DUNNING, T.H., HAY, P.J.
Journal of Chemical Physics 66, 3767, 1977

50. GOODMAN, J., TULLY, J.C., BONDYBEY, V.E., BRUS, L.E.
Journal of Chemical Physics 66, 4802, 1977

51. POWELL, H.T., MURRAY, J.R., RHODES, C.K.
Applied Physics Letters 25, 730, 1974

52. BASOV, N.G., BABEIKO, Y.A., ZUEV, V.S., MIKHEEV, L.D.
Soviet Journal of Quantum Electronics 6, 505, 1976

53. HUESTIS, D.L., GUTCHECK, R.A., HILL, R.M., LORENTZ, D.C.
SRI Report 75-18, 1975

54. FINK, E.H., COMES, F.J.
Chemical Physics Letters 30, 267, 1975

55. WALLACE,SS.C., DREYFUS, R.W.
Applied Physics Letters 25, 498, 1974

56. WROBEL, W.G., ROHR, H., STEUER, K.H.
Applied Physics Letters 36, 113, 1980

57. JONES, M.

Ph.D. Thesis, London University, 1981

58. LITTMAN, M.G., METCALF, H.J.

Applied Optics 17, 2224, 1978

59. CORNEY, A., MANNERS, J., WEBB, C.E.

Optics Communications 31, 354, 1979

60. STROME, F.C., WEBB, J.P.

Journal of Applied Optics 10, 1348, 1971

61. Handbook of Chemistry and Physics. Chemical Rubber Publishing Company

62. Harshaw Optical Crystals Cataloque. Published by the Harshaw Chemical Company

63. MALITSON, I.H.

Journal of Optical Society of America 54, 628, 1964

64. STOCKBARGER, D.C.

O.S.R.D. Report Number 4690, 1944

65. Available from the Harshaw Chemical Company, U.S.A.

66. SCHAFER, F.P., MULLER, H.

Optics Communications 2, 407, 1971

67. MILES, R.B., HARRIS, S.E.

I.E.E.E. Journal of Quantum Electronics 9, 470, 1973

68. DALGARNO, A., KINGSTON, A.E.

Proceedings of the Royal Society 259, 424, 1960

69. KOCH, E.E., (editor)

VUV Radiation Physics. (page 683), Published by the Pergamom Press, 1974

70. STICKLEY, C.M.

Physics Today 31, 50, May 1978

71. RHODES, C.K. (editor)

Excimer Lasers. (page 60) Springer-Verlag, 1979

72. BLACK, G., SHARPLESS, R.L., SLANGER, T.G.
Journal of Chemical Physics 64, 3985, 1976

73. SHAW, M.J., GOWER, M.C., ROLT, S.
Chemical Physics Letters 73, 478, 1980

74. PACK, R.T.
Journal of Physical Chemistry 65, 4765, 1976

75. FINN, E.J., KING, G.W.
Journal of Molecular Spectroscopy 56, 39&52 1975

76. POWELL, H.T., EWING, J.J.
Applied Physics Letters 15, 165, 1978

77. POWELL, H.T., PROSNITZ, D., SCHLEICHER, B.R.
Applied Physics Letters 34, 571, 1979

78. BLACK, G., SHARPLESS, R.L., SLANGER, T.G., LORENTS, D.C.
Journal of Chemical Physics 62, 4274, 1975

79. CUNNINGHAM, D.L., CLARK, K.C.
Journal of Chemical Physics 61, 1118, 1974

80. POWELL, H.T., HAZI, A.U.
Chemical Physics Letters 59, 71, 1978

81. RICE, J.K., WOODWORTH, J.R.
Research Progress Report, Sandia Labs., 1978

82. DUNCAN, W.
Ph.D. Thesis, University of Edinburgh, 1976

83. PEARSON, T.G., ROBINSON, P.L.
Journal of the Chemical Society, page 652, 1932

84. MASSEY, H.S.W., BURHOP, E.H.S., GILBODY, H.B.
Electronic and ionic impact Phenomena, Volume II
Page 777. Published by Clarendon Press, 1969

85. FLOWERS, B.H., MENDOZA, E.
Properties of Matter, Chapter 6, Published by John
Wiley and Sons, London, 1970

86. LOVELOCK, J.E.

Analytical Chemistry 33, 162, 1961

88. BLACK, G., SHARPLESS, R.L., SLANGER, T.G.

Journal of Chemical Physics 64, 3993, 1976

88. RICE, J.K., WOODWORTH, J.R., TROTT, W.M.

Sandia National Laboratories, Report SAND 79-2480

89. McGUIRE, E.J.

Physical Review A 19, 1978, 1979

89(a). RICE, J.K., WOODWORTH, J.R.

Journal of Applied Physics 50, 4415, 1979

90. MOHLER, F.L., FOOTE, A.

Physical Review 27, 37, 1926

91. MARR, G.V., WHERRETT, S.R.

Journal of Physics B 5, 1735, 1972

92. POPESCU, D., PASCU, M.L., COLLINS, C.B., JOHNSON, B.W.

Physical Review A 8, 1666, 1973

93. SEATON, M.J.

Proceedings of the Royal Society A 208, 408, 1951

94. LITTLE, E.M.

Physical Review 30, 109, 1927

95. MOHLER, F.L., BOECKNER, C.

Bureau of Standards Journal of Research 3, 303, 1929

96 COOK, T.B., DUNNING, F.B., FOLTZ, G.W., STEBBINGS, R.F.

Physical Review A 15, 1526, 1977

97. BRADDICK, H.J.J., DITCHBURN, R.W.

Proceedings of the Royal Society A 143, 472, 1934

98. MARR, G.V., CREEK, D.M.

Proceedings of the Royal Society A 304, 233, 1968

99. WEISHEIT, J.C.

Physical Review A 5, 1621, 1972

100. NORCROSS, D.N.

Physical Review A 7, 606, 1973

101. HONIG, R.E.

R.C.A. Review 23, 567, 1962

102. CREEK, D.M., MARR, G.V.

Journal of Quant. Spectr. and Rad. Trans. 8, 1431, 1968

103. POPESCU, D., POPESCU, I., MAURER, J., COLLINS, C.B.

Physical Review A 12, 1425, 1975

104. WATERS, P.M.

Physical Review 111, 1053, 1958

105. MAIMAN, T.H.

Nature, 187, 493, 1960

106. PARKS, J.H.

Applied Physics Letters 31, 192, 1977

107. PARKS, J.H.

Applied Physics Letters 31, 296, 1977

108. SCHIMITSCHEK, E.J., CELTO, J.E.

Optics Letters 2, 64, 1978

109. BURNHAM, R.

Applied Physics Letters 33, 156, 1978

110. SCHIMITSCHEK, E.J., CELTO, J.E., TRIAS, J.A.

Applied Physics Letters 31, 608, 1977

111. EDEN, J.G.

Applied Physics Letters 33, 495, 1978

112. PEIRCE, F.O.

Wied. Ann. 6, 597, 1879

113. TERENIN, A.

Nature 118, 843, 1926

114. TERENIN, A.

Zeitschrift fur Physik 44, 713, 1927

115. MULLIKEN, R.S.

Physical Review 26, 1, 1925

116. BUTKOW, K.

Zeitschrift fur Physik 71, 673, 1931

116. SPOONER, H.

Z. fur Phys. Chem. B 11, 425, 1931

118. KONTRATJEW, V.

Z. fur Phys. Chem. B 11, 470, 1931

119. WIELAND, K.

Helvetica Physica Acta 76, 157, 1932

120. WIELAND, K.

Helvetica Physica Acta 76, 801, 1932

121. SINGER, J.R., GOROG, I.

Bulletin of the American Physical Society 7, 14, 1962

122. RAUTIAN, S.G., SOBELMAN, I.I.

Soviet Physics J.E.T.P. 14, 1433, 1962

123. ZARE, R.N., HERSCHBACH, D.R.

Applied Optics Supplement 2, 193, 1965

124. WALTER, W.T., JARRET, S.M.

Applied Optics Supplement 2, 201, 1965

125. KASPER, J.V.V., PIMENTEL, G.C.

Applied Physics Letters 5, 231, 1964

126. HOFMANN, H., LEONE, S.R.

Journal of Chemical Physics 69, 3819, 1978

127. PRINGSHEIM, P.

Fluorescence and Phosphorescence. (page 275)

128. WADT, W.R.

Journal of Chemical Physics 72, 2469, 1980

129. WIELAND, K.

Helvetica Physica Acta 14, 420, 1941

130. QUILLE, L.L.

The Chemistry and Metallurgy of Miscellaneous Materials. Published by McGraw-Hill, 1950

131. MAYA, J.

Journal of Chemical Physics 67, 4976, 1977

132. MAYA, J.

I.E.E.E. Journal of Quantum Electronics 7, 579, 1979

133. MURRAY, J.R., RHODES, C.K.

Journal of Applied Physics 47, 5041, 1976

134. DUZY, C., HYMAN, H.A.

Chemical physics Letters 52, 345, 1977

135. ROXLO, C., MANDL, A.

Journal of Chemical Physics 72, 541, 1980

136. WEHRLI, M.

Helvetica Physica Acta 11, 339, 1938

137. SPOONER, H., TELLER, E.

Journal of Chemical Physics 7, 382, 1939

138. TEMPLET, P., McDONALD, J.R., McGLYNN, S.P.

Journal of Chemical Physics 56, 5746, 1972

139. NOYES, W.A., LEIGHTON, P.A.

The Photochemistry of Gases. Reinhold Publishing Company, New York, 1941

140. WINTHER, C.

Z. Wiss. Phot. 11, 60, 1912

141. DICKINSON, P.

Ph.D. Thesis, London University 1980

142. FRANCK, J., RABINOWITCH, E.

Transactions of the Faraday Society 30, 120, 1934

143. MANDL, A., PARKS, J.H.

Applied Physics Letters 33, 498, 1978

144. MANDL, A., PARKS, J.H., ROXLO, C.

Journal of Chemical Physics 72, 504, 1980

145. MANDL, A., PARKS, J.H.

Review of Scientific Instruments 50, 127, 1979

146. WANANT, R.W., EDEN, J.G.

Applied Physics Letters 33, 703, 1978

147. DJEU, N., MAZZA, C.

Chemical Physics Letters 46, 172, 1977

148. TERENIN, A.

Naturwissenschaften 15, 73, 1927

149. EHRLICH, D.J., OSGOOD, R.M.

Applied Physics Letters 34, 655, 1979

150. EHRLICH, D.J., OSGOOD, R.M.

I.E.E.E. Journal of Quantum Electronics 16, 257, 1980

151. BURNHAM, R.

Applied Physics Letters 30, 132, 1977

152. DEUTSCH, T.F., EHRLICH, D.J., OSGOOD, R.M.

Optics Letters 4, 376, 1979

153. BJORKLUND, G.C.

I.E.E.E. Journal of Quantum Electronics 11, 287, 1975

154. CARMAN, R.L., LOWDERMILK, W.H.

Physical Review Letters 33, 190, 1974

155. WHITE, J.C., ZDASIUK, G.A.

Journal of Chemical Physics 69, 2256, 1978

ACKNOWLEDGEMENTS

I wish to thank my supervisor, Professor D.J. Bradley, and Dr M.H.R. Hutchinson, for their help and guidance during the past four years.

I am indebted to Dr K.T.V. Grattan, my co-worker during the selenium and caesium experiments. I would also like to thank Drs C.B. Edwards, M. Jones, P.W. Smith, J.R. Taylor, J. Vukusic, and the other members of the Laser Group for their co-operation.

Thanks are also due to Messrs B. Weekley, C. Cooper, R. Morrison, J. Bean, and J. Clark for their technical assistance.

I would also like to thank my flat-mates, Ms R. Snell, and Mr T.S. Theocharis. Many thanks to Ms W. Jackson for reading the manuscript and making many valuable comments.

Finally, I wish to thank my parents, who manage to give me constant support, even though they were 2000 miles away.

The author was supported by a University of London Studentship and a research assistantship from the SRC.

J. Phys. B: Atom. Molec. Phys. 13 (1980) 2931–2935. Printed in Great Britain

Absolute determination of the photoionisation cross section for ground-state atomic caesium in the vacuum ultraviolet

K T V Grattan, M H R Hutchinson and E S Theocharous
Blackett Laboratory, Imperial College, Prince Consort Road, London SW7 2BZ, England

Received 3 March 1980

Abstract. Measurement of the absolute photoionisation cross section of caesium vapour is made in the vacuum ultraviolet using a xenon excimer laser. A value of $0{\cdot}9 \times 10^{-19}$ cm^2 is reported at 172 nm, in agreement with recent theoretical calculations.

1. Introduction

The photoabsorption of alkali metals has been a subject of both theoretical and experimental studies for many years as these elements are important in a variety of laboratory processes and instruments, e.g. photoemissive devices, electron sources in plasma physics etc. Historically, the agreement between theoretical and experimental measurements of the cross section has been poor, particularly in the vacuum ultraviolet region of the spectrum.

Previous measurements have largely been confined to the near ultraviolet spectral region and may be classified as either 'direct' measurement which monitors the photo-current to determine the cross section (Little 1927, Mohler and Boeckner 1929) or 'indirect' measurement where the decrease in the intensity of light transmitted through a vapour cell is measured (Braddick and Ditchburn 1934, Marr and Creek 1968). This latter work extended measurement below 200 nm using DC gas discharge lamps as optical sources. However, these experimental measurements indicate cross sections which are substantially larger than the recent theoretical values of Norcross (1973) and Weisheit (1972) in the wavelength regions extending to approximately 230 nm and 150 nm respectively. These theoretical calculations are in close agreement with each other in the region of common study. Recent work by Cook *et al* (1977) using a dye laser beam crossed with an atomic beam of Cs has shown excellent agreement with the latter theoretical calculation in the spectral region extending to about 240 nm but as yet there exists no agreement between theoretical and experimental measurements in the VUV.

In this work, a high power xenon laser is used to determine the cross section for the photoionisation of caesium atoms in the VUV, at 172 nm, using a 'direct' method of measurement. The use of such a high-power laser rather than a discharge lamp enables lower number densities of caesium to be used which decreases the errors arising from dimer formation. Errors in photon flux measurement are also reduced by the use of a collimated beam of radiation.

0022-3700/80/152931+05$01.50 © 1980 The Institute of Physics

2. Theoretical background

The rate of photoionisation which is caused by the propagation of the laser beam through a cell containing caesium vapour is given by

$$\frac{dn}{dt} = \sigma_i(\lambda) n_c F(\lambda, t)$$

where n is the electron (or ion) number density, n_c is the caesium number density, $F(\lambda, t)$ is the ionising flux density in photons $cm^{-2}\ s^{-1}$ and $\sigma_i(\lambda)$ is the photoionisation cross section. If the density of caesium atoms is not significantly altered by the radiation, the total number of electrons or ions produced by the laser pulse is

$$N = \sigma_i(\lambda) n_c A l \int_0^\infty F(\lambda, t)\, dt$$

where A is the laser beam cross sectional area and l is the interaction length. If the total number of photons in the pulse is P, then

$$N = \sigma_i(\lambda) n_c l P.$$

Hence the photoionisation cross section may be determined by measuring the total charge produced by a laser pulse of known energy, the caesium number density being determined from published measurements of vapour pressure as a function of temperature. Errors arising from the measurement of the interaction volume are minimised since only the length l need be measured and hence no particular constraints are necessary on the cross sectional laser beam profile.

3. Experimental

Positive ions produced by the photoionisation of Cs atoms were collected using a simple ionisation chamber, described in a previous publication (Grattan *et al* 1980). Three collinear cylindrical electrodes were contained in a stainless steel vacuum housing, which was resistant to chemical attack by caesium vapour and could be evacuated to below 10^{-6} mbar. The central electrode collected charge over a well defined 10 mm length with the two outer electrodes acting as guard rings. A thin wire was slightly displaced from the axis of the chamber. This carried a small voltage, variable in the region −400 to +400 V, sufficient to ensure that the device operated on the plateau region of the detector characteristic. The total time-integrated charge was measured with an electrometer (Keithley type 601). Positive ions, rather than electrons, were collected because thermal electrons from the walls and electrodes were always present. The mean free path of electrons in the low-pressure (10^{-4} to 10^{-3} mbar) Cs vapour used experimentally was considerably greater than the approximately 1 cm dimension of the detector, ensuring negligible error from collisional ionisation.

Laser radiation from a 1 Hz xenon laser (Edwards *et al* 1979), of maximum energy output around 30 mJ at 172 nm, was admitted to the cell via a thin Spectrosil window. In order to reduce the background signal caused by the generation of photoelectrons by scattered light, the laser beam passed through the cell and out through a second window.

Caesium was prepared by the reduction of caesium chromate with powdered aluminium, materials of spectroscopic purity (>99·9%) being used. The metal was transferred to a glass ampule under vacuum and this was placed in the glass sidearm which was attached to the ionisation chamber. The ampule was then broken in the sidearm when the chamber was evacuated. The entire device was enclosed in a large oven, the temperature of which was controlled to ±1 K, with small apertures for the admission and exit of the laser beam. Heat loss from the small windows was minimised by the vacuum pipes used to transmit the laser beam into and from the ionisation cell. Thus the temperature of the ionisation cell was both well known and regulated. The oven was operated in the temperature region 350–400 K to obtain the required Cs vapour pressures. At these temperatures the dimer concentration of the caesium vapour is small, of the order of 0·1 → 0·5%. Corrections for dimer absorption have had to be applied in other measurements (Marr and Creek 1968) and in the near ultraviolet region the Cs_2 absorption cross section is about 10^2 times larger than that for atomic caesium, making this a potentially significant source of error. However, in the vacuum ultraviolet, the dimer absorption cross section is less than 1×10^{-19} cm^2 (Creek and Marr 1968), making such errors in this work approximately 1% or less.

The characteristic of the detector is shown in figure 1, and to ensure complete collection of the ions produced, the device was operated at 100 V.

The laser energy was measured using a laser calorimeter (Laser Instrumentation Limited—Model 142 LR).

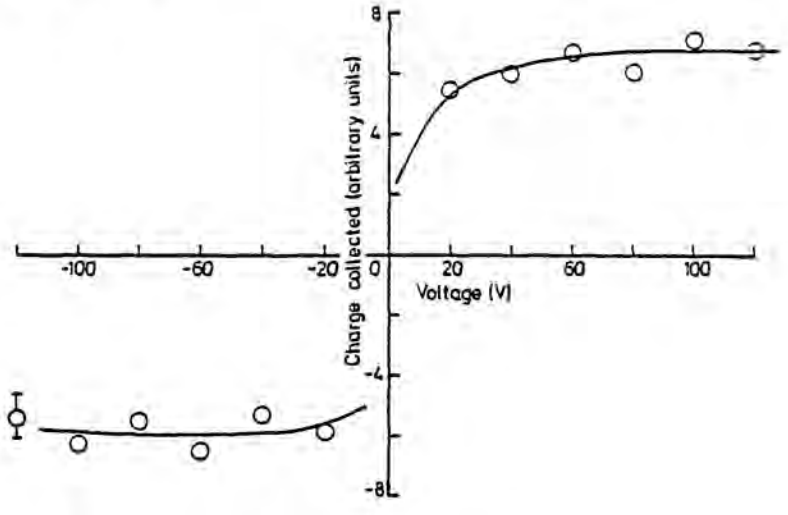


Figure 1. Characteristic response of the photoionisation detector.

4. Experimental results and discussion

The positive charge collected was monitored as a function of laser energy for eight temperatures in the region 350–400 K. At each temperature, a graph was plotted of the number of charges collected (N) against the number of input photons (P), the gradients of which yield $\sigma_i n_c$. By plotting this against the caesium number density (n_c) as shown in figure 2, σ_i was obtained. Using the vapour pressure measurements reported by Honig (1962), σ_i was determined to be $0{\cdot}9\times10^{-19}$ cm^2 (±30%).

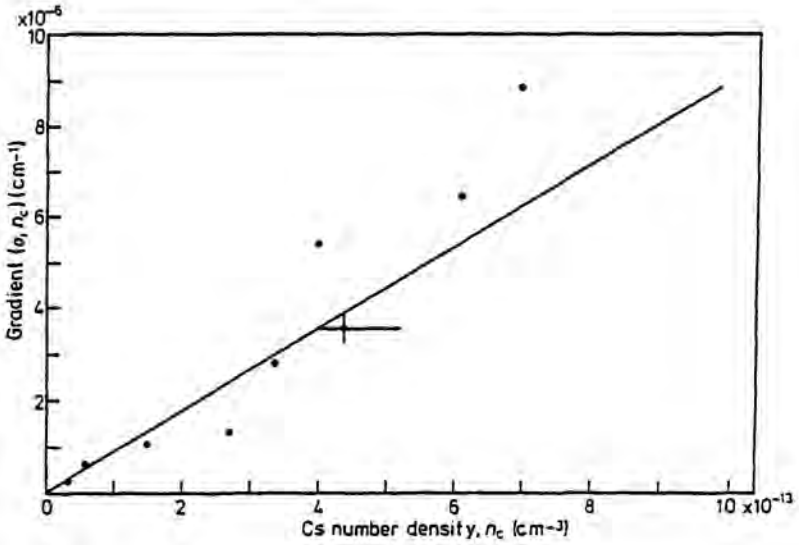


Figure 2. $\sigma_1 n_c$ plotted against caesium number density, n_c.

The main source of error in the result is in the determination of the caesium vapour pressure. The maximum error in temperature measurement is estimated at ±2 K (including the error of the temperature probe) resulting in about a ±15% error in n_c. The only other significant source of error is in the measurement of the laser energy as N and l are well defined. Secondary emission from the cathode due to bombardment by low-energy Cs^+ ions is negligible under the conditions of the experiment (Waters 1958). Consequently, a total error of ±30% is reported.

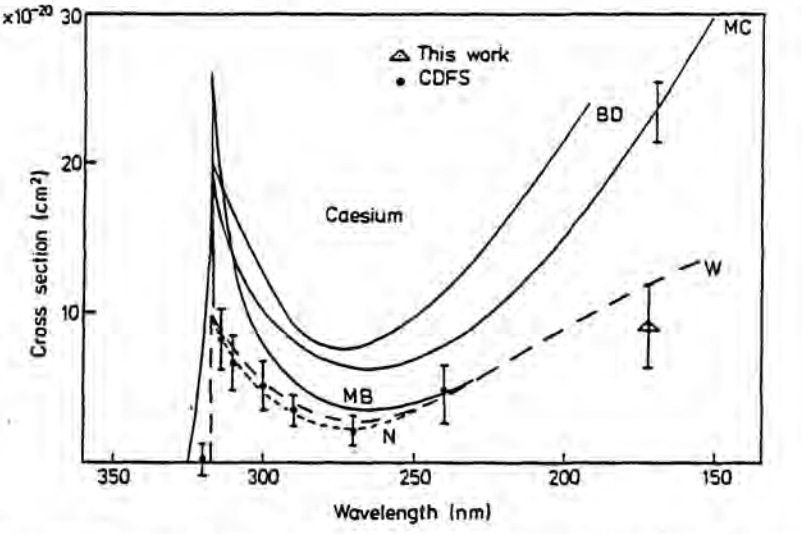


Figure 3. Comparison with other work. Full curves represent experimental measurements; BD, Braddick and Ditchburn (1934); MB, Mohler and Boeckner (1929); MC, Marr and Creek (1968); CDFS, Cook *et al* (1977) with earlier results reflecting modern vapour pressure measurements (Honig 1962). Broken curves represent the theoretical work of Weisheit 1972 (W) and Norcross (1973) (N).

In conclusion, the result obtained is compared with other work, in figure 3, and appears to substantiate the calculation of Weisheit (1972) at the same wavelength, in disagreement with the result of Marr and Creek (1968), thereby extending the agreement of the work of Cook *et al* (1977) in the near ultraviolet into the vacuum ultraviolet.

Acknowledgments

The authors wish to express their thanks to Professor D J Bradley for the provision of laboratory facilities and to Dr C J Latimer for helpful information. The preparation of the caesium sample by Mr B Weekly is appreciated, as was funding by the SRC and the Rutherford and Appleton Laboratories.

References

Braddick H J J and Ditchburn R W 1934 *Proc. R. Soc.* A **143** 472
Cook T B, Dunning F B, Foltz G W and Stebbings R F 1977 *Phys. Rev.* A **15** 1526
Creek D M and Marr G V 1968 *J. Quant. Spectrosc. Radiat. Transfer* **8** 1431
Edwards C B, Hutchinson M H R, Bradley D J and Hutchinson M D 1979 *Rev. Sci. Instrum.* **50** 1201
Grattan K T V, Hutchinson M H R and Theocharous E S 1980 *IEEE J. Quantum Electron.* **QE-16** No 9
Honig R E 1962 *RCA Rev.* **23** 567
Little E M 1927 *Phys. Rev.* **30** 109
Marr G V and Creek D M 1968 *Proc. R. Soc.* A **304** 233
Mohler F L and Boeckner C J 1929 *J. Res. NBS* **3** 303
Norcross D W 1973 *Phys. Rev.* A **7** 606
Waters P M 1958 *Phys. Rev.* **111** 1053
Weisheit J C 1972 *Phys. Rev.* A **5** 1621

Measurement of the Wavelength-Dependent Photoionization Cross Section of Se*(^1S) in the Spectral Region of 170–175 nm

KENNETH T. V. GRATTAN, HENRY R. HUTCHINSON, AND EVANGELOS S. THEOCHAROUS

Abstract—The photoionization cross section of excited atomic selenium, Se($^1S_0$), obtained by photodissociation of OCSe, has been measured in the wavelength region of 170–175 nm using a tunable xenon laser. A minimum value, at 172 nm, was found to be 1.2×10^{-20} cm^2, approximately ten times less than a recently calculated value. The photodissociation cross section for OCSe, at the same wavelength, was found to be 0.8×10^{-16} cm^2, in good agreement with published work. The effect of an election cooling buffer gas upon the electron production from excited selenium was also investigated.

I. Introduction

FORBIDDEN electric dipole transitions originating from the metastable (^1S) levels of the group VI-A elements (O, S, Se, and Te) offer the possibility of constructing lasers with high optical storage densities, suitable for the generation of high intensity pulses [1] with efficiencies of 1–2 percent. The auroral ($^1S - {}^1D$) and transauroral ($^1S - {}^3P$) transitions have optical cross sections of $\sim 4 \times 10^{-19}$ cm^2 and provide a suitable compromise between the suppression of parasitic gain and the ability to saturate amplifiers at laser fluences below the damage threshold of the associated optics. These excited atoms can be produced by VUV photodissociation of simple triatomic molecules, e.g., N_2O, OCS, or OCSe. Of particular interest are the metastable (^1S) states of S and Se which can be produced with near unit quantum efficiency (ϕ) by photolysis with Kr_2^* and Xe_2^* excimer radiation, respectively [2], [3]. Laser action has recently been demonstrated in atomic selenium and sulphur by Powell *et al.* [4], [5] using such an excitation scheme.

Stored energy in the laser upper level may be reduced by quenching by the parent triatomic molecule, viz.,

$$\mathrm{Se}(^1S) + \mathrm{OCSe} \rightarrow \mathrm{Se}_2^* + \mathrm{CO} \tag{1}$$

and by photoionization by the photolysing radiation, viz.,

$$\mathrm{Se}(^1S) + h\nu(172\ \mathrm{nm}) \rightarrow \mathrm{Se}^+ + e^-. \tag{2}$$

Quenching reaction (1) may be reduced by bleaching the absorption of OCSe by photolysis radiation of sufficient fluence ($E > h\nu/\sigma_d$ where σ_d is the photodissociation cross section). However, quenching by superelastic collisions with the electrons produced by photoionization causes electron heating and subsequent multiplication with a drastic decrease in the overall laser efficiency. Accurate kinetic modeling therefore requires a knowledge of the photodissociation cross section (σ_d) and the photoionization cross section (σ_i).

In this work, an experimental measurement of the photoionization cross section of Se(^1S) is made with a tunable Xe laser in the wavelength range of 170–175 nm.

II. Theoretical Background

When a sample of OCSe is photolyzed by 172 nm radiation to yield Se(^1S) atoms, the photoionization rate of this product may be given by

$$\frac{\partial n_e(x,t)}{\partial t} = \sigma_i I(x,t)\, \rho^*(x,t) - [\mathrm{loss}] \tag{3}$$

where $n_e(x,t)$ is the electron number density, σ_i is the photoionization cross section (at 172 nm) for Se(^1S), and $\rho^*(x,t)$ is the Se(^1S) number density. This may be given in terms of the initial OCSe density $\rho_0(x)$ by

$$\rho^*(x,t) = \phi[\rho_0(x) - \rho(x,t)]$$

where ϕ is the quantum yield for (^1S) production and $\rho(x,t)$ is the time varying OCSe density. $I(x,t)$ is the input laser pulse intensity and [loss] represents an electron loss rate, mainly due to recombination, which is sufficiently slow to be ignored. Superelastic collisions of electrons with Se(^1S) atoms produce electron heating and these higher energy electrons can in turn ionize the excited selenium atoms, thus providing a secondary source of electrons. The rate of production of electrons by this avalanching process can be reduced substantially by introducing a buffer gas (e.g., N_2) to cool the electrons or by keeping the number densities of electrons and excited atoms sufficiently small. This was ensured both by operating at low pressures of OCSe ($\sim 10^{-2}$ mbar) which, at the laser fluences used, gave rise to electron number densities of $\sim 10^{11}$ cm^{-3} and atomic (^1S) densities of $\sim 10^{15}$ cm^{-3} and by using N_2 as a buffer gas. The Se(^1S) atoms may be quenched by both electrons and buffer gas molecules [4], [5]. However, the quenching rates are sufficiently small for these processes to be insignificant during the ~10 ns duration of the VUV laser pulse which produces photoionization from Se(^1S).

The solution of (3) is given [7] by

$$N_e = \frac{\sigma_i \phi \rho_0}{\sigma_d} \{\ln[V/\exp(\sigma_d \rho_0 x)] + [1 - \exp(\sigma_d E)]\ V^{-1}\} \tag{4}$$

where

Manuscript received February 27, 1980. This work was supported by the S. R. C. Rutherford Laboratory.

The authors are with the Blackett Laboratory, Imperial College, University of London, London SW7 2BZ England.

0018-9197/80/1100-1170$00.75 © 1980 IEEE

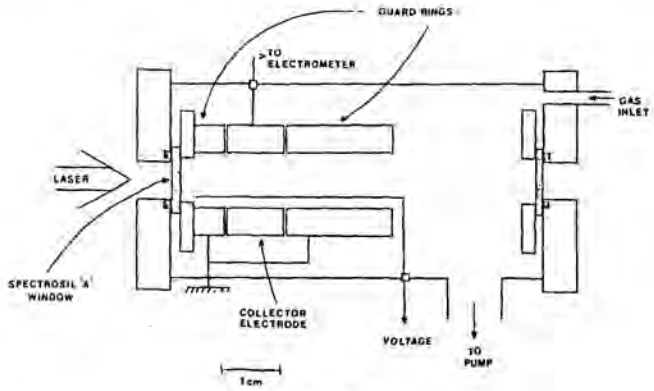


Fig. 1. Ionization chamber.

$$V = \exp(\sigma_d E) + \exp(\sigma_d \rho_0 x) - 1 \tag{5}$$

and E is the laser fluence (photon density).

Under the conditions of the experiment ($\rho_0 \sim 10^{15}$ cm^{-3}, $\sigma_d \sim 10^{-16}$ cm^2, $x \sim 1$ cm, and $E \sim 1\text{-}5 \times 10^{16}$ cm^{-2}), $\sigma_d E \gg \sigma_d \rho_0 x$ and $\exp(\sigma_d \rho_0 x) \sim 1$. Hence, (5) may be simplified thus,

$$V \approx \exp(\sigma_d E) \tag{6}$$

and (4) may be simplified to

$$N_e = \frac{\sigma_i \phi \rho_0 AL}{\sigma_d} [\ln V + V^{-1} - 1] \tag{7}$$

where N_e is the total number of electrons detected, A is the area of the input laser beam, and L is the length of the collection region. With high incident laser fluences ($E \geqslant 5 \times 10^{16}$ cm^{-2}), $V^{-1} \ll 1$, and (7) may be further simplified to (8):

$$N_e = \frac{\sigma_i \phi \rho_0 AL}{\sigma_d} [\ln V - 1] \tag{8}$$

implying that a plot of the number of electrons collected against the initial number density of OCSe (ρ_0) will be a straight line of slope $\sigma_i \phi AL\ [\ln V - 1]/\sigma_d$. Furthermore, a graphical representation of the electron number (N_e) against laser fluence (E) yields a curve which tends to a straight line at high fluences of slope $\sigma_i \phi \rho_0 AL$. This has an intercept on the N_e axis of $-\sigma_i \phi \rho_0 AL/\sigma_d$ and from the intercept on the E axis σ_d^{-1} is obtained.

III. Experimental Apparatus

Electrons (or ions) produced by the photoionization of Se(^1S) atoms were collected using a simple ionization chamber, as illustrated in Fig. 1. A high vacuum housing, which could be evacuated to a pressure of less than 10^{-6} mbar, was used to contain a system of three collinear cylindrical electrodes. The detector was made from stainless steel where possible since most other metals are chemically attacked by OCSe [8].

A central cylindrical electrode collected charge over a well defined length and the outer cylinders, insulated from the collector electrode by 0.25 mm thick mylar spacers, served as earthed guard rings. A thin wire slightly displaced from the axis of the collector carried a small voltage, which could be varied in the range of -400 to +400 V, the breakdown voltage of the detector being approximately 420 V. This was sufficient to ensure the device operated on the plateau of the photo-

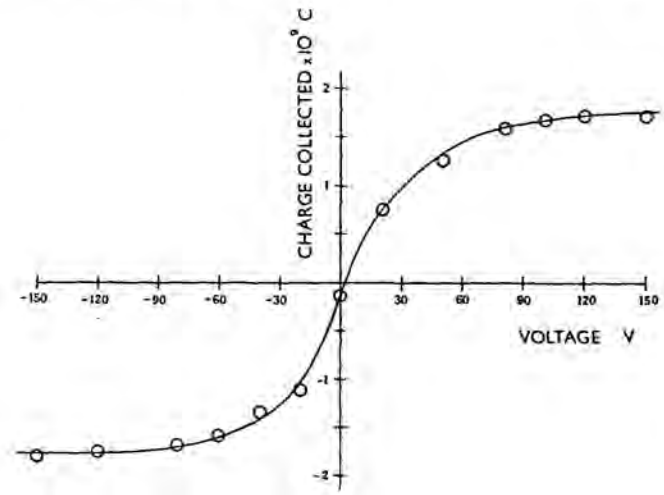


Fig. 2. Characteristic response of the detector.

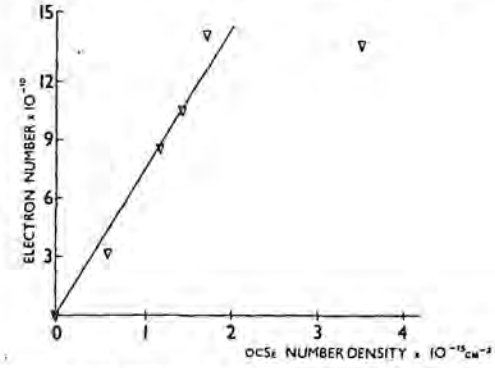


Fig. 3. The electron number as a function of the OCSe number density at a constant laser energy.

electron current against the voltage curve. Electrons and ions produced were detected with an electrometer (Keithley type 601) or a fast oscilloscope (Tektronix type 7904).

Laser radiation from a 1 Hz xenon laser [9], capable of a maximum output in excess of 25 mJ in pulses of approximately 10 ns duration, was admitted to the cell through a well defined aperture via a thin (1-2 mm) Spectrosil window. The laser beam passed through the cell and left the cell through a second window. This reduced the background signal caused by the generation of photoelectrons from scattered light within the cell to a typical value of a few percent of the actual signal observed with OCSe present.

Carbonyl selenide was prepared by the action of dry CO on heated Se [10] and purified by trap to trap distillation, its purity being checked by its infrared absorption spectrum. The sample was stored as a solid at liquid nitrogen temperatures to prevent decomposition.

The characteristic of the detector was determined for a known pressure of OCSe and is given in Fig. 2. This shows a plateau with both positive and negative signals and an operating voltage of 100 V was used in subsequent experiments, thereby ensuring complete collection of electrons.

VI. Experimental Results

Initially, the xenon laser was operated untuned ($\lambda \sim 172$ nm, $\Delta\lambda \sim 1$ nm) with a 10 mm collector electrode in the ionization chamber. The observed relationship between N_e and ρ_0 is shown in Fig. 3, in good agreement with the linear dependence

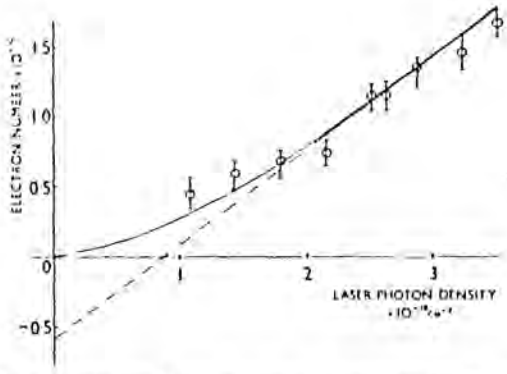


Fig. 4. The electron number as a function of photon density for a constant OCSe pressure.

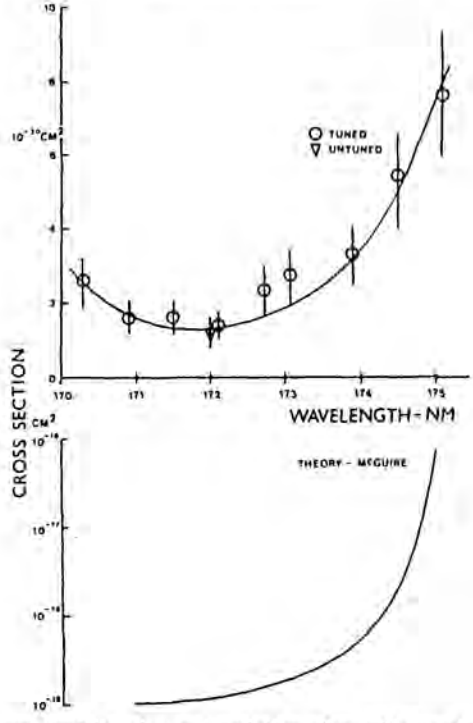


Fig. 5. Experimentally observed variation of σ_i with wavelength (top) and theoretical calculation of σ_i over the same wavelength region (bottom) by McGuire [12].

at low OCSe densities predicted by (8). From a knowledge of the quantum efficiency, $\phi \approx 1$ [3], [11], σ_i was determined to be 1.3×10^{-20} (±25 percent)cm^{-2}.

Fig. 4 is a plot of N_e against laser fluence (photon density). The curve shown is a plot fitted to (7) and the dotted line illustrates the linear relationship, seen at high fluences. From its slope and intercept on the electron number axis, σ_i was determined to be 1.2×10^{-20} (±25 percent)cm^2 and 1.1×10^{-20} (±25 percent)cm^2, respectively. An average value of 1.2×10^{-20} (±25 percent)cm^2 is thus reported for σ_i. From the intercept on the photon density axis, σ_d was found to be 0.8×10^{-16} (±25 percent)cm^2.

Operation of the laser in the tuned mode enabled σ_i to be measured over the range of 170–175 nm. The results are shown in Fig. 5, illustrating a minimum in σ_i in the region of 171–173 nm, which agrees well with the value obtained at 172 nm using the untuned laser.

In addition to cooling the electrons, a molecular buffer has

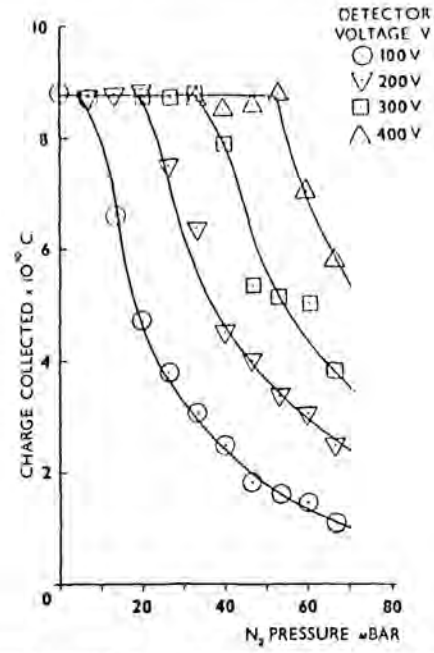


Fig. 6. Charge collected as a function of N_2 buffer gas pressure, for different detector operating voltages.

been shown by Powell *et al.* [4] to provide quenching of the $Se(^3P_1)$ of $Se(^1D_2)$ lower laser levels, produced either directly by photodissociation or by quenching of $Se(^1S)$ by electrons. To ensure that electron multiplication by ionization of $Se(^1S)$ by hot electrons does not occur in the detector, the effect of the addition of N_2 on the charge collected was studied. The characteristic operating voltage of the ionization chamber needed to be increased with increasing N_2 pressure to collect all the charge produced, but Fig. 6 clearly indicates that at the pressures studied, up to the breakdown voltage of the detector, the charge collected is independent of the pressure of added N_2.

V. Discussion

The experimentally obtained value for σ_i with the laser untuned is considerably smaller than a recently calculated value by McGuire [12], who reported $\sigma_i \sim 10^{-19}$ cm^2 at 172 nm. However, similar measurements for sulphur for the $S^*(^1S)$ state by Rice *et al.* [7] also show a value approximately one order of magnitude less than that calculated by McGuire [12] for sulphur. Also, in the case of the laser tuned over the 170–175 nm region, while the experimental results show a similar trend to that calculated by McGuire, the change in σ_i with wavelength is much less dramatic and suggests that a modification to the theoretical model may be necessary.

The fact that no change in electron signal was recorded with the addition of N_2 suggests that the $Se(^1S)$ concentration is unaffected by the presence of N_2 (up to the added pressure of 60 mbar) and that, at the OCSe pressures [and hence the $Se(^1S)$ concentrations] used in the experiment, electron avalanching is not important.

The measured value of the photodissociation cross section σ_d is in good agreement with the values reported by other experimenters, taking into account the excitation bandwidth of the laser [3], [13].

Thus, the maximum value of ϕ and a minimum value of σ_i both lie at 172 nm, the pump wavelength of the xenon laser, and confirm that Xe_2^* excimer radiation is a suitable choice of excitation for the Se photodissociation laser.

Acknowledgment

The authors would like to thank Dr. M. J. Shaw for providing the sample of OCSe used in this work and gratefully acknowledge the provision of research facilities by Prof. D. J. Bradley.

References

[1] J. R. Murray and C. K. Rhodes, "The possibility of high-energy-storage lasers using the auroral and transauroral transitions of column-VI elements," *J. Appl. Phys.*, vol. 47, pp. 5041–5058, 1976.

[2] G. Black, R. L. Sharpless, T. G. Slanger and D. C. Lorents, "Quantum yields for the production of S (^{1}S) from OCS (1100–1700 A)," *J. Chem. Phys.*, vol. 62, pp. 4274–4277, 1975.

[3] G. Black, R. L. Sharpless, and T. G. Slanger, "Quantum yields for the production of Se(^{1}S) from OCSe (1100–2000A)," *J. Chem. Phys.*, vol. 64, pp. 3985–3992, 1976.

[4] H. T. Powell and J. J. Ewing, "Forbidden transition selenium atom photodissociation lasers," *Appl. Phys. Lett.*, vol. 33, pp. 165–167, 1978.

[5] H. T. Powell, D. Prosnitz, and B. R. Schleicher, "Sulfur $^1S_0$-$^1D_2$ laser by OCS photodissociation," *Appl. Phys. Lett.*, vol. 34, pp. 571–573, 1979.

[6] G. Black, R. L. Sharpless, and T. G. Slanger "Quenching of electronically excited selenium atoms, Se($^1S_0$)," *J. Chem. Phys.*, vol. 64, pp. 3993–3997, 1976.

[7] J. K. Rice and J. R. Woodworth, "Kinetic processes in photolytically produced group VI ^{1}S atoms," *Laser Dev. Laser Fusion Appl., Res. Prog. Rep.*, Sandia Labs, Dec. 1978, pp. 34–44.

[8] W. Duncan, "The electronic spectra of simple main group inorganic and organometallic systems," Ph.D. dissertation, Univ. Edinburgh, 1976.

[9] C. B. Edwards, M. H. R. Hutchinson, D. J. Bradley, and M. D. Hutchinson, "Repetitive vacuum ultraviolet xenon excimer laser," *Rev. Sci. Instrum.*, vol. 50, pp. 1201–1207, 1979.

[10] T. G. Pearson and P. L. Robinson, "Carbonyl selenide, Part I. Preparation and physical properties," *J. Chem. Soc.*, pp. 652–660, 1932.

[11] M. J. Shaw, private communication.

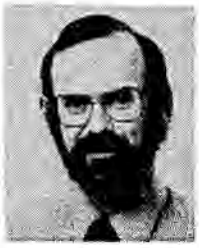
[12] E. J. McGuire, "Photoionization of the group VI $(ns)^2$ $(np)^4$ $^1S_0$ term via excitation of autoionizing levels," *Laser Dev. Laser Fusion Appl., Res. Prog. Rep.*, Sandia Labs, Dec. 1978, pp. 44–58.

[13] E. J. Finn and G. W. King, "The absorption spectrum of carbonyl selenide-Rydberg transitions" *J. Molec. Spectrosc.*, vol. 56, pp. 52–63, 1975.



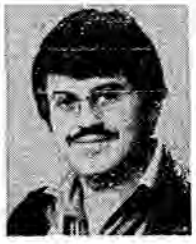
Kenneth T. V. Grattan was born on December 9, 1953 in County Armagh, Northern Ireland. He received the B.Sc. degree in physics and the Ph.D. degree from the Queen's University of Belfast, Northern Ireland, in 1974 and 1978 respectively. His doctoral research involved the development of ultraviolet gas discharge lasers and their applications to the study of the photophysics of vapor phase organic scintillators.

Since 1978, he has been a Research Assistant at the Blackett Laboratory, Imperial College, London, England, where he is working on UV and VUV excimer lasers and their applications to Group VI high energy storage lasers.



Henry R. Hutchinson was born in County Londonderry, Northern Ireland, on December 2, 1945. He received the B.Sc. and Ph.D. degrees from the Queen's University of Belfast, Northern Ireland, in 1968 and 1971, respectively. His dissertation research was on the nonlinear interaction of intense laser pulses with dyes.

From 1971 to 1973 he worked on electron-beam pumped lasers. Since 1973 he has been a Lecturer in Physics at the Blackett Laboratory, Imperial College, University of London, London, England, where he is engaged in research on the development and application of UV and VUV excimer lasers and the generation of short-wavelength radiation by nonlinear frequency mixing.



Evangelos S. Theocharous was born in Famagusta, Cyprus, on August 11, 1954. He received the B.Sc. and A.R.C.S. degrees in physics in 1976 from the Imperial College, University of London, London, England, where he is currently working towards the Ph.D. degree.

He is a Research Assistant at the Imperial College where his research is in the field of vacuum ultraviolet laser development and applications to molecular photodissociation.